D'Hondt, S.L., Jørgensen, B.B., Miller, D.J., et al., 2003
Proceedings of the Ocean Drilling Program, Initial Reports Volume 201

11. SITE 1230[1]

Shipboard Scientific Party[2]

BACKGROUND AND OBJECTIVES

Site 1230 was the single hydrate-bearing site selected for drilling during Leg 201. The principal objectives at this site were

1. To determine if and how hydrate-bearing sequences differ in microbial activities, microbial communities, and the nature of microbe-environment interactions from nearby methane-rich sequences that lack hydrates (Sites 1227 and 1229) and nearby sulfate-rich sequences with low methane concentration (Site 1228) and
2. To provide a Peru margin microbial and biogeochemical counterpoint to hydrate-rich sites in other regions of the world ocean (such as Leg 164's northwest Atlantic Blake Ridge and Leg 204's northeast Pacific Hydrate Ridge).

Site 1230 is located on the lower slope of the Peru Trench in 5086 m water depth. Sediments of this area are part of the accretionary wedge just landward of the Peru Trench (Suess, von Huene, et al., 1988). The lithologies, sediment age, and many geochemical and geophysical characteristics of the target site were well characterized by Leg 112 studies of nearby Site 685 (Shipboard Scientific Party, 1988). The upper 200 m of Pleistocene to Holocene sediment is a clay-rich diatomaceous mud, partly accreted by downslope transport from the shelf. At ~200 meters below seafloor (mbsf), a stratigraphic hiatus of ~4.5 m.y. separates the slope deposit from upper Miocene diatom ooze (Shipboard Scientific Party, 1988). Authigenic carbonates and phosphates are sparse, whereas pyrite framboids are abundant throughout the section (Shipboard Scientific Party, 1988). Calculated sedimentation rates are high; they average 250 m/m.y. for the Miocene sequence and 100 m/m.y. for the Pleis-

[1]Examples of how to reference the whole or part of this volume.
[2]Shipboard Scientific Party addresses.

Ms 201IR-111

tocene section (Shipboard Scientific Party, 1988). These high rates are consistent with sedimentation in a lower-slope basin or trench axis.

The surface waters over Site 1230 are part of the Peru upwelling system and are biologically highly productive. The organic carbon content of the sediment is high at Site 685 (Shipboard Science Party, 1988). Methane concentrations were observed to rise above 1 bar by 11.6 mbsf and remain in the range of 10^4–10^5 µL/L throughout the cored sediment column down to 432 mbsf (Kvenvolden et al., 1990). Concentrations of ethane and butane generally increase downhole from 1 to 100 µL/L, and the methane/ethane ratio decreases from 10^5 to 10^3. The Leg 112 Scientific Party found visual evidence of methane hydrate at 99 and 164 mbsf in the form of small pieces of dark gray hydrate (Shipboard Scientific Party, 1988; Kvenvolden and Kastner, 1990). The samples looked like rounded pieces of mudstone but felt cold and showed bubbling foam. Based on this information, Site 1230 provides an excellent opportunity for assessing the nature of microbial communities and their activities in hydrate-bearing sediments rich in organic material and under high hydrostatic pressure.

Concentrations of dissolved sulfate decline to 0 mM between the first and second core analyzed at Site 685 (between 3 and 18.1 mbsf) (Shipboard Scientific Party, 1988). Chloride concentrations range between 525 and 555 mM. The maximum concentration is associated with the most shallow sulfate-free sample (18.1 mbsf) and was suggested by the Leg 112 Shipboard Scientific Party to lie just above hydrate at the top of the hydrate stability field. Salinity, alkalinity, dissolved ammonium, phosphate, and magnesium concentrations rise to maximum values in the interval of 107–134 mbsf, decline sharply between 165 and 235 mbsf, and then decrease gradually to the base of the hole at ~450 mbsf. The maxima in alkalinity (156 mM), ammonium (31,760 µM), and phosphate (826 µM) were the highest then known from deep-ocean drilling (Shipboard Scientific Party, 1988). Downhole variation in chloride and calcium concentrations is generally opposite to the variation in these other chemical species. The pH drops below 7 at 133 mbsf and remains below 7 to the base of the hole (Shipboard Scientific Party, 1988).

These patterns of interstitial water (IW) chemistry are inferred to result from high levels of biological activity throughout the sediment column, coupled with hydrate formation and diffusive exchange with the overlying ocean. The subsurface extent of key electron donors (hydrogen, acetate, and formate) and electron acceptors with standard free-energy yields greater than that of sulfate (oxygen, nitrate, manganese oxide, and iron oxides) was not determined for Site 685.

PRINCIPAL RESULTS

The biogeochemical zonation of Site 1230 is more typical of an upper-slope sediment than a typical deep-sea sediment; its uppermost sediment contains a narrow suboxic zone, and sulfate depletion occurs at <9 mbsf. Oxygen and nitrate are not detectable at the top of the mudline core. Dissolved manganese is present in the uppermost 0.5 m of sediment but is near the detection limit (<1 µM) throughout the remaining sediment column. Dissolved iron is likewise low (mostly 1–3 µM) in the upper 25 m of the sediment. Below the narrow suboxic zone, sulfate reduction is the dominant mineralization process down to the bottom of the sulfate zone at 8–9 mbsf. The sulfate gradient is

nearly linear and indicates that most of the net sulfate reduction takes place at the sulfate/methane interface (Iversen and Jørgensen, 1985; Niewöhner et al., 1998; Borowski et al., 1996, 2000).

Methane builds up steeply beginning at the sulfate boundary, and it reaches >1 bar partial pressure by 11 mbsf. Below that depth, methane concentrations in recovered cores fluctuate around a few millimolar, which is the usual pattern in supersaturated cores with gas escape upon depressurization. At Site 1230, however, nine successful deployments of the pressure coring sampler (PCS) at depths ranging from 22 to 277 mbsf allowed the methane concentration profile from the entire sediment column to be accurately determined. The PCS recovered a full 1-m core in most deployments. Its highest internal pressure was 8086 psi in a core recovered from 254.6 mbsf. At 254.6 mbsf, 8086 psi is equivalent to 105% of hydrostatic pressure. The overpressure is caused by dissolving gas hydrate resulting from warming during the wireline trip (Dickens et al., 2000). The total amount of methane retrieved by the PCS reached 400,000 µM methane at 157 mbsf. This greatly exceeds methane solubility at the ambient temperature and hydrostatic pressure but is consistent with the presence of several percent gas hydrate in the sediment pore space.

The presence of gas hydrate was also monitored by rapid infrared (IR) scanning of the recovered cores. Immediately after retrieval, each core was brought to the catwalk and scanned along the core liner surface with a digital IR camera. Our purpose was to detect the cooling effect caused by rapid gas hydrate dissolution. This approach was successful, as core segments with negative temperature anomalies of about –5°C proved to harbor gas hydrate. Hydrate was recovered from ~82 and ~148 mbsf as small pieces mixed with sediment. The recovered hydrate probably represented only a small fraction of the in situ hydrate because of rapid dissolution and loss in the expanding cores. Samples from four additional horizons (123, 142, 150, and 200 mbsf) probably contained disseminated gas hydrate, based on observed fizzing and scanned temperature anomalies as low as –3.2°C. Downhole sonic and resistivity logs suggest broad intervals of possible hydrate presence. Preliminary comparison of inferred hydrate distributions and PCS methane data suggests that the interstitial concentrations of dissolved methane build up to reach the phase boundary of hydrate formation at ~50 mbsf. The dissolved concentrations may remain at this phase boundary at depth, with intervals of hydrate formation determined by the lithology and physical properties of the sediment.

The depth distribution of chloride in the interstitial water also provided evidence of hydrates, which release freshwater by dissolution during the wireline trip of the sediment core. Chloride shows a distinct gradient with a peak at 18 mbsf. This subsurface peak is presumably a remnant of the last glacial salinity excursion. It is accentuated by a drop in chlorinity below 18 mbsf that is probably due to freshening by hydrate dissolution. Within the methane zone, the drop in chlorinity is 10–27 mM and the concentrations show strong depth fluctuations with minimum values that appear to coincide with depths of hydrate occurrences (e.g., at 82 mbsf).

Ethane and propane are present at 1–2 ppm concentrations throughout the methane-rich zone down to ~140 mbsf. Their concentrations increase three- to fivefold over the next 70 m. Their distribution profiles suggest that ethane and propane are products of organic carbon degradation in the methanogenic zone.

Interstitial water analyses at Site 1230 provide clear evidence of very high microbial activity with extreme accumulations of products from organic degradation processes. Alkalinity and dissolved inorganic carbon (DIC) increase steeply with depth from near seawater values at the sediment/water interface to a broad maxima of 155 mM at 100–150 mbsf, deep in the methanogenic zone. These concentrations are among the highest ever measured in marine sediments. Below this maximum, the concentrations drop again with depth. Ammonium likewise builds up extreme concentrations of 35,000 to 40,000 µM from 100 to 150 mbsf.

Below the interface of counter-diffusing sulfate and methane, there is a second diffusive interface between hydrogen sulfide and iron at 25 mbsf. The hydrogen sulfide produced from sulfate reduction reaches a peak concentration of 9.4 mM at the bottom of the sulfate zone. From there it decreases steeply both upward and downward, reaching zero near the sediment/water interface and at 25 mbsf. Iron is abundant (5–57 µM) in the interstitial water of the methane zone from 200 to 25 mbsf, where it meets the hydrogen sulfide and is inferred to precipitate as ferrous sulfide and pyrite.

A diffusive interface between sulfate and barium is encountered at 8–9 mbsf. Barium concentrations are only a few micromolar in the sulfate zone but increase steeply below that zone to plateau at 400 µM between 50 and 150 mbsf. At 250 mbsf barium concentrations approach 1000 µM, which may be the highest interstitial water concentration of barium ever recorded in deep-sea sediments. The narrow depth interval of coexisting barium and sulfate appears to be a zone of barite precipitation. We infer their concentrations to be determined by the solubility product of barite in that zone. Consequently, the shallow sulfate zone is an effective barrier against upward diffusion of dissolved barium. Barium fronts associated with the sulfate boundary have also been observed in sediments of the Gulf of California and the South Atlantic Ocean (Brumsack, 1986; Kasten et al., 2001). Based on data from Leg 112, von Breymann et al. (1990) concluded that the deepest sites have the highest dissolved and solid-phase barium concentrations because detritus sedimenting through a deepwater column scavenges barium from seawater and enriches the sediment in barium.

Acetate and formate are generated as fermentation products and are used as substrates by sulfate-reducing or methanogenic prokaryotes. These volatile fatty acids (VFAs) are present at much higher concentrations at Site 1230 than at any other site studied during Leg 201. The acetate level is 5–20 µM in the sulfate reduction zone and reaches 230 µM in the methane zone at 145 mbsf. This acetate concentration is fivefold higher than at the most active sites on the Peru shelf and is even 10- to 100-fold higher than at the other deep-sea sites. Formate remains mostly at 5–10 µM throughout the sediment column. Hydrogen concentrations are low, in the 0.1- to 1.5-nM range.

The interstitial water at Site 1230 has a distinct yellow color that is not present at any other Leg 201 site. We presume this color is probably due to dissolved organic matter. The intensity of the color, which was measured spectrophotometrically, increases steeply from zero at the sediment/water interface to a broad maximum between 25 and 150 mbsf. Below that depth, it drops again to reach 15%–20% of the maximum value at 250 mbsf.

Prokaryotic cell concentrations in the organic-rich Pleistocene to Holocene sediments are near the average of previously studied subseafloor sediments in the upper 60 m of the sediment column. They are about

threefold above average in the next 150 m. However, in the older accretionary wedge sediments below 216 mbsf, the cell density abruptly drops fourfold, from 7.9×10^6 to 1.9×10^6 cells/cm^3. This shows that the concentration of subseafloor prokaryotic cells at Site 1230 is closely related to sediment age rather than sediment depth. The factor that ultimately regulates cell concentrations may be the availability of energy substrates for prokaryotic metabolism.

Samples were taken at regular depth intervals through the entire sediment column for deoxyribonucleic acid (DNA) and fluorescent in situ hybridization-secondary ion mass spectrometry (FISH-SIMS) analysis, measurements of sulfate reduction rates, hydrogen turnover, methanogenesis rates, acetate turnover, thymidine incorporation, and prokaryote lipid biomarkers. Samples for cultivations and viable counts (most probable number [MPN]) target specific depths and geochemical zones, including the sulfate/methane interface and the hydrate-rich methane zone. Contamination tests with perfluorocarbon tracer (PFT) and fluorescent beads show that the potential seawater contamination of Site 1230 microbiological samples is low or undetectable. The only case of detectable bead contamination in a slurry used for Site 1230 microbial cultivations is based on two beads counted in 100 microscopic fields of view scanned. By the experience accumulated during this leg, our confidence has strengthened that, with rigorous contamination controls and aseptic sampling techniques, deep subsurface samples can routinely be obtained without the introduction of microorganisms from the surface environment.

Four successful temperature measurements (two Adara tool deployments and two Davis-Villinger Temperature Probe [DVTP] deployments) over a depth interval of 0–255 mbsf defined a geothermal gradient of 34.3°C/km at Site 1230, with a mudline temperature of 1.7°C and an estimated temperature of 11.2°C at 278 mbsf. The estimated local heat flux is 28 mW/m^2. This is similar to the heat flux calculated by Yamano and Uyeda (1990) at Site 685 from wireline logging data over 75–150 mbsf. Based on a downhole measurement of overpressure, upward interstitial water advection of ~1 cm/yr may occur at this site.

OPERATIONS

Transit to Site 1230

The 187-nmi sea voyage between Sites 1229 and 1230 lasted 16.6 hr at a speed of 11.3 kt. We arrived on the Global Positioning System coordinates for Site 685, as recorded in the Leg 112 *Initial Reports* volume (Shipboard Scientific Party, 1988), just after midnight on 11 March. After a positioning beacon was deployed, the pipe trip to bottom in 5097 m water depth required 11 hr. Coring operations are described in Table T1.

T1. Coring summary, Site 1230, p. 86.

Hole 1230A

We began operations in Hole 1230A, offset 50 m north of the Site 685 coordinates, with a water sampling temperature probe (WSTP) deployment to collect a water sample. The Adara temperature shoe was included on the core barrel assembly for Core 1H to measure the temperature at the mudline. The first core at Site 1230 (Core 1H) (0.0–4.8 mbsf; recovery = 100%) arrived on deck at 1645 hr on 11 March. Continuous

advanced hydraulic piston coring (APC) operations through Core 6H returned an average of 103% recovery. Low levels of hydrogen sulfide were measured with handheld detectors on the first three cores, and hydrogen sulfide safety protocols were observed. Hydrogen sulfide was not detected in cores recovered from below 33 mbsf. Cores recovered from below 33 mbsf all showed evidence of gas expansion, which appeared to increase in severity downhole, so precaution against explosive core liner rupture (perforating the core liners with a handheld drill) was continued through the rest of our coring operation.

The PCS was deployed on Core 7P (52.3 mbsf) and returned a full barrel under pressure. Continuous APC coring followed through Core 15H (to 127.3 mbsf). We were able to advance much farther with piston coring than was achieved during Leg 112 because of technological advancements in APC operations. Recovery in this interval was >100%, despite an apparent less than full stroke on the piston coring system (measured by drill-over depth) due to core expansion. Core 16P (PCS) (127.3–129.3 mbsf) also returned a full core barrel under pressure. Cores 17H through 19H (129.3–156.8 mbsf) returned progressively poorer recovery (recovery = 54%–34%) in expanded cores. Core 20P (156.8–158.8 mbsf) recovered 65 cm of poorly consolidated core under pressure.

Cores 21H through 24H (158.8–196.8 mbsf) suffered incomplete stroke and poor recovery (recovery = 7%–44%), but we continued our strategy of drilling through 9.5-m intervals. Another PCS deployment (Core 25P; 196.8–198.8 mbsf) recovered 18 cm of core under pressure. Four more APC cores (Cores 26H through 29H; 198.8–226.3 mbsf) were also interpreted as incomplete deployments, with the APC shoe coming free after only a meter or so of drill over. The Adara temperature shoe was included on the core barrel assembly for Core 29H and was damaged because of the formation density. These cores returned an average of <1.5 m of core. After deployment of Core 28H, we decided to use a center bit while drilling to the full-stroke depth in order to avoid clogging the bottom-hole assembly. The subsequent Core 29H returned only 0.5 m of core, so to supplement recovery for IW analysis we chose to core to the next APC deployment depth with the extended core barrel (XCB). Only 3.3 m of advancement was possible with Core 30X, which returned 1.78 m of core. Another XCB barrel was deployed to determine if the reason for poor penetration was due to clay buildup on the XCB bit or if the main bit was not capable of further penetration. After cutting though a hard layer (part of which was recovered in the top of Core 31X; 229.6–234.1 mbsf), we decided to continue the approach of APC coring and advancing by recovery, followed by XCB coring of the underlying interval. Two short APC strokes returned <1 m each of core, but Core 35X was nearly full (recovery = 99%) of semisoft sediment. The PCS was deployed as Core 36P (254.6–256.6 mbsf), followed by two XCB cores (Cores 37X and 38X; 256.6–276.8 mbsf). Based on the results of the Core 36P (reduced pressure and gas content compared to shallower deployments), we deployed the pressure core barrel as our final coring tool in Hole 1230A (Core 39P; 276.8–278.8 mbsf).

PFT was pumped continuously during all coring operations at Site 1230 as part of our contamination testing, and fluorescent microspheres were deployed on Cores 1H, 2H, 8H, 38X, and possibly 13H. The DVTP was deployed at 33.3, 79.8, 148.3, 177.8, and 256.6 mbsf; however, only the deployments at 33 and 256 mbsf returned data consistent with a reasonable thermal profile. All other deployments either failed to return any data or provided low temperatures indicative of

poor penetration of the probe tip into stiff sediment. The Davis-Villinger Temperature-Pressure Probe (DVTP-P) was deployed at 257.6 mbsf. A wireline logging program consisting of two runs, one with the triple combination (triple combo) tool string and a second with the Formation MicroScanner (FMS)-sonic tool string, completed operations in Hole 1230A. Logging was completed by 2200 hr on 16 March.

Hole 1230B

After an offset of 20 m north, Hole 1230B was initiated at 2300 hr on 16 March. The interval of 3–11 mbsf was of the most intense interest to shipboard scientists, so we wanted this interval recovered in a single core barrel. Core 1H returned 5.4 m. For Core 2H the bit was lowered to 3 mbsf (based on the recovery from Core 1H). For Janus bookkeeping purposes this required adjusting the bottom depth of Core 1H to 3 mbsf, resulting in an artificial value of 100% recovery for Core 1H. The interval between 3.0 and 5.8 mbsf is represented twice in our recovery. High-density sampling for interstitial water, methane, and microbiological DNA assays effectively depleted all but the first and last sections of Core 2H.

Our operations plan for this hole included three deployments of the PCS to complete the shallow portion of the gas profile initiated in Hole 1230A. Coring continued with Core 3H (12.5–22 mbsf; recovery = 105%) and PCS Core 4P (22.0–24.0 mbsf). APC coring to 71.5 mbsf (Cores 5H through 9H) returned 107% recovery. Core 10P (71.5–73.5 mbsf) returned 99 cm of core under pressure. APC coring to 100 mbsf reached our depth objective for this hole, and coring operations ended with a final deployment of the PCS (Core 14P; 103.0–105.0 mbsf). The DVTP was deployed at 73.5 and 100.0 mbsf, and the DVTP-P was deployed at 101.5 mbsf. The APC-methane (APC-M) tool was deployed continuously from Core 201-1230B-3H to 13H.

Holes 1230C, 1230D, 1230E

Three shallow holes (two APC cores each in Holes 1230C and 1230D and four APC cores in Hole 1230E) were cored to provide samples for dense microbiological sampling (Hole 1230C), paleoceanography and paleomagnetics studies (Hole 1230D), and to ensure that material representing the shallow part of the interval cored at Site 1230 was preserved in the Ocean Drilling Program (ODP) archive (Hole 1230E). Fluorescent microspheres were deployed on Cores 201-1230C-1H and 2H. The Adara tool measured a mudline temperature before Core 201-1230E-1H and a temperature at 32.5 mbsf on Core 201-1230E-4H. The DVTP-P was deployed at 32.5 mbsf. A final PCS deployment was completed at the base of Hole 1230E (34.0–36.0 mbsf). Operations at Site 1230 concluded when the bit passed through the rig floor at 0820 hr on 19 March, and we began our transit to our final site for Leg 201.

LITHOSTRATIGRAPHY

At Site 1230 we recovered a 278.3-m-thick sequence of biogenic and siliciclastic Holocene, Pleistocene, and Miocene sediments from the lower slope of the Peru Trench. The proposed lithostratigraphy is mainly based on Hole 1230A, as it was the only hole at Site 1230 that was continuously cored from the sediment surface to a depth of 278.3

mbsf. The lithostratigraphic description of the sedimentary sequence is based on observation of sediment color, sedimentary structures, and structural features (visual core description), smear slide analysis, and color reflectance. X-ray diffraction (XRD) and measurements of magnetic susceptibility, density, and natural gamma radiation (NGR) were also used to detect lithologic and sedimentologic changes (see "Physical Properties," p. 22, and "Downhole Logging," p. 32).

Based on textural descriptions and wireline log data (see "Downhole Logging," p. 32), sediments from Site 1230 were subdivided into two lithostratigraphic units (Fig. F1). As Site 1230 is located in close proximity (within 100 m) of Leg 112 Site 685, the age framework presented in this chapter follows the chronostratigraphic observations of the Leg 112 Shipboard Scientific Party (1988).

F1. Lithostratigraphic summary, p. 43.

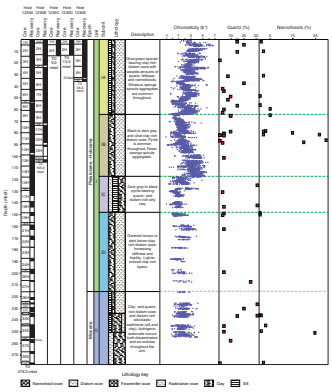

Description of Lithostratigraphic Units

Unit I

Interval: 201-1230A-1H-1 through 27H-CC; 201-1230B-1H-1 through 14P-1; 201-1230C-1H-1 through 2H-CC; 201-1230D-1H-1 through 2H-CC; and 201-1230E-1H-1 through 5P-1
Depth: 0–215.8 mbsf
Age: Holocene–Pleistocene

Unit I consists mostly of biogenic sediments mixed with varying amounts of siliciclastic components. Even though diatom ooze is the dominant component of Unit I, differences in color and in the relative amount of the terrigenous components (mostly quartz) justified further subdivision into four subunits.

Throughout Unit I, several high-angle normal faults with offsets of a few centimeters were observed (Fig. F2A). The first faults are present at shallow depth in Subunit IA (e.g., Section 201-1230B-5H-5) and are common throughout the rest of Unit I. Immediately after splitting, some of the sediments from Subunits IA and IB (e.g., Section 201-1230B-7H-6) were black to dark gray in color. However, these colors changed to lighter olive-green hues in <30 min. The color change is presumably caused by the oxidation of iron monosulfide on the cut surface of the split core. Pyrite was commonly found at lithologic boundaries, in faults (Fig. F2A, F2B), in veins, and in spots and streaks, which often outlined *Chondrites*-type trace fossils.

F2. Site 1230 features, p. 44.

Subunit IA

Interval: 201-1230A-1H-1 through 9H-3; 201-1230B-1H-1 through 8H-CC; 201-1230C-1H-1 through 2H-CC; 201-1230D-1H-1 through 2H-CC; and 201-1230E-1H-1 through 5P-1
Depth: 0–64.1 mbsf

The main lithology of Subunit IA is olive-green spicule- and quartz-bearing clay-rich diatom ooze with variable amounts of quartz, feldspar (both usually <10%), nannofossils (usually <5%), and rare foraminifers. Scattered white sponge spicule aggregates, with diameters ranging from a few millimeters to 1 cm, as well as pyrite specks and streaks (e.g., Cores 201-1230A-2H and 5H), are common features of this subunit. In many parts of Subunit IA, the main lithology alternates with layers of different color and composition. The most common alternations occur with dark olive to brown, several-centimeter-thick layers, which usually are com-

posed of diatom-rich nannofossil ooze. The mineralogic composition of these nannofossil layers includes mostly calcite, with minor amounts of quartz, plagioclase, and pyrite (e.g., XRD Sample 201-1230B-1H-4, 15–16 cm) (see also "Mineralogy," p. 11). These layers are commonly bioturbated, have sharp basal contacts, and are commonly outlined by dark sulfide accumulations (see "Mineralogy," p. 11). A relatively coarse-grained, ~20-cm-thick horizon composed of several yellow layers of foraminifer-bearing clay- and diatom-rich nannofossil ooze was observed in Sections 201-1230B-1H-4 and 201-1230C-1H-3 (Fig. F2C). The layers in this horizon show an increase in foraminifer content toward the base and are associated with dark gray pyrite-rich horizons. The layers have sharp basal contacts and normal grading indicative of redeposition (Fig. F2C). Pale yellow layers composed of quartz-bearing diatom-, foraminifer-, and clay-rich nannofossil ooze are also present in Core 201-1230A-5H. Brown layers composed of diatom-rich clay were observed at several depths in this subunit. These layers are particularly frequent in Core 201-1230A-4H as well as in Section 201-1230A-6H-6. Bioturbation is weak to moderate throughout the subunit and is mostly of *Chondrites* type. High-angle lamination, most likely due to soft sediment deformation, is present in Sections 201-1230A-3H-5 through 3H-7 (Fig. F2E).

After splitting, Section 201-1230D-2H-5, which contains the base of the sulfate reduction zone at 10.6 mbsf (see "Biogeochemistry," p. 12), showed evidence of degassing. Bubbles continued to form on the split surface of the soft sediment several hours after the core had been retrieved. Below this depth, sulfide-rich specks are common in sediments from Site 1230 (e.g., XRD Sample 201-1230B-7H-1, 144 cm).

The lowermost part of Subunit IA (Sections 201-1230A-7P-1 through 9H-3) is characterized by alternations of olive to dark gray nannofossil- and spicule-bearing clay-rich diatom ooze and darker blackish clay-rich diatom ooze. The lower boundary of Subunit IA corresponds to a sharp decrease in chromaticity values (b*) and matches a positive shift in magnetic susceptibility (Fig. F1) (see also "Physical Properties," p. 22).

Subunit IB

Interval: 201-1230A-9H-4 through 14H-CC and 201-1230B-9H-1 through 14P-1
Depth: 64.1–117.8 mbsf

Dark gray to olive, more or less bioturbated clay-rich diatom ooze characterizes the lithology of Subunit IB. Siliciclastic components such as quartz and feldspar generally comprise <10% of the bulk sediment. Diatom content ranges between 50% and 60%. Calcareous nannoplankton is present in trace amounts in the uppermost part of the subunit and disappears below ~79 mbsf (Fig. F1). White spicule aggregates are present but seem to be less frequent compared to Subunit IA. *Chondrites*-type trace fossils are present in moderate density throughout the subunit. Pyrite specks and streaks are common. High-angle normal faults showing offsets of a few centimeters are also common.

In Hole 1230A, the color of sediments from Subunit IB changes gradually from dark gray at the top (Section 201-1230A-9H-4) to dark olive (Core 13H) and brown at the bottom (Core 15H). This change is also recorded by variations in the chromaticity profile (Fig. F1). These gradual color changes coincide with a steady increase in compaction and "stiffness" of the sediment, which also shows pervasive foliation parallel or subparallel to bedding.

Subunit IC

Interval: 201-1230A-15H-1 through 18H-CC
Depth: 117.8–148.3 mbsf

Consolidated, fissile, dark gray to black pyrite-bearing diatom-rich silty clay is the dominant lithology of Subunit IC. A shift toward relatively low values of the chromaticity variable (b*) occurs at the top of this subunit (Fig. F1). The shift is inferred to be due to a relative increase in the siliciclastic fraction, as quartz content is higher than in both the over- and underlying subunits. Although diatom abundance is lower than in Subunit IB, it seems to increase toward the bottom of the subunit (e.g., Section 201-1230A-18H-3, 123 cm). Some portions are characterized by faint banding resulting from decimeter-scale alternation between darker and lighter layers. Bioturbation is moderate to high throughout and is mostly of *Chondrites* type.

Subunit ID

Interval: 201-1230A-19H-1 through 27H-CC
Depth: 148.3–215.8 mbsf

The boundary between Subunits IC and ID is defined by a change in sediment color from dark gray to greenish brown and dark brown. This color change is reflected by a moderate shift of the chromaticity variable b* (Fig. F1). The sediment of this subunit is well consolidated and fissile clay-rich diatom ooze. Fissility is usually pervasive, and in some cases (e.g., Core 201-1230A-19H) is oblique to bedding (Fig. F2F). In the uppermost part of the subunit (Core 201-1230A-19H), dark brown clay-rich intervals alternate with lighter-colored olive diatom ooze. In general, the former appear to be less fractured and more ductile than the latter.

Poor core recovery and strong drilling disturbance characterized a large portion of Hole 1230A, including most of Subunit ID (recovery = 23%) and the underlying Unit II. According to biostratigraphic data presented in the Leg 112 *Initial Reports* volume (Shipboard Scientific Party, 1988), a major hiatus in the biostratigraphic record is present between ~200 and 203 mbsf at Site 685. This hiatus (with a minimum duration of 4.3 m.y.) separates lower Pleistocene slope deposits (Unit I) from accreted upper Miocene sediments (Unit II). Wireline logging data, in particular *P*-wave velocity, resistivity, and bulk density, show a prominent shift between 215 and 216 mbsf for Site 1230 (see "Downhole Logging," p. 32). These data indicate the presence of a fractured zone, which may represent an unconformable tectonized contact between Units I and II. Accordingly, we established the boundary between Units I and II at the core break between Cores 201-1230A-27H and 28H at 215.8 mbsf (Fig. F1) (see also "Unit II," p. 10).

Unit II

Interval: 201-1230A-28H-1 through 39P-1
Depth: 215.8–278.3 mbsf
Age: Miocene

Most of Unit II is characterized by both poor recovery and core disturbance. The few sections recovered from the uppermost three cores of this unit (Sections 201-1230A-28X-1 and 30X-1) are characterized by a pervasive scaly fabric (Fig. F2G), which offers further support to the presence of a tectonic boundary between Units I and II. It is also worth not-

ing that several layers of dolomite breccia are present in both Section 201-1230A-30X-1 and the underlying Section 31X-1 (Fig. F2H) (see also "Mineralogy," p. 11). Sandy fabric is less pervasive between Sections 201-1230A-31X-1 (Fig. F2I) and Section 35X-2, where the sediment includes a few scattered dolostone nodules and is a consolidated and fissile, commonly bioturbated clay- and quartz-rich diatom ooze (XRD Sample 201-1230A-31X-1, 93–94 cm). Scaly fabric, possibly related to tectonic fracturing, was also observed in the upper part of Section 201-1230A-35X-4. Below this fractured layer, several carbonate concretions are present within relatively undisturbed sediment composed of quartz-bearing dolomite-rich clay.

In general, lighter layers with higher nannofossil concentrations and disseminated carbonate rhombohedra are more common below ~235 mbsf (Fig. F1). Usually, diatom- and silt-rich intervals have a dry, semiconsolidated appearance, whereas clay-rich layers are smoother, with a more homogeneous texture.

Mineralogy

A total of 21 XRD analyses were performed on samples collected from both Holes 1230A and 1230B. Overall, quartz was the primary mineral detected; it was detected together with plagioclase in all analyzed samples. The highest concentrations of quartz were recorded in the highly consolidated and fractured dark silt- and clay-rich diatom oozes of Unit II (Samples 201-1230A-31X-1, 93–94 cm; 33X-2, 14 cm; and 33X-CC, 14 cm). Plagioclase seems to be more concentrated in the brown nannofossil ooze layers of Subunit IA (e.g., Sample 201-1230B-1H-4, 15–16 cm). Glauconite, pyrite, and clay are also common minerals at this site; however, they are only present in small or trace amounts. In Subunits IA and IB, dark pyrite concentrations commonly outline boundaries between alternating olive diatom ooze and brown nannofossil ooze layers (Fig. F2C). Pyrite is also a common mineral in the consolidated, fissile, and fractured sediments of Unit II (e.g., Sample 201-1230A-33X-CC, 16 cm). Glauconite is present in most of the analyzed samples, and the highest concentrations of this mineral were detected in the quartz-rich samples of Unit II (e.g., Sample 201-1230A-31X-1, 93–94 cm). The amount of calcite is generally related to the presence of nannofossils in the biogenic assemblage. In Unit I, calcite was detected only in nannofossil-rich layers (e.g., Sample 201-1230B-1H-4, 15–16 cm) (Fig. F2C; interval between 15 and 16 cm). In the nannofossil-rich sediments of Unit II, calcite was found in most of the analyzed samples (e.g., Sample 201-1230A-35X-5, 68–68 cm). A dolomite layer was found in Unit II (Sample 201-1230A-31X-1, 0–18 cm). The latter is probably a cemented breccia, which is present below the tectonized interval that marks the boundary between Units I and II. Even though most of the sediments from Site 1230 are composed of variable amounts of diatom ooze, opal-A could only be detected in the samples from Unit II that had the lowest concentrations of quartz (Samples 201-1230A-30X-1, 93–94 cm; 35X-4, 40 cm; 35X-4, 80 cm; and 35X-5, 68 cm).

The mineralogy of Site 1230 sediments offers some insights on the depositional setting of both Units I and II. The common presence of quartz and plagioclase in most of the analyzed samples indicates that there was a relatively constant input of fine-grained terrigenous components during the deposition of both units. The origin of both calcite and opal-A is clearly biogenic, as the presence of these minerals is

linked to nannofossil- and diatom-rich sediments, respectively. The presence of authigenic dolomite at or near the boundary between the Pleistocene to Holocene sediments of Unit I and the Miocene sediments of the accretionary prism (Unit II) might indicate fluid flow and carbonate precipitation along a tectonic surface.

Summary

Drilling on the lower slope of the Peru Trench produced a 278.3-m-thick sequence of both biogenic and siliciclastic sediments. The majority of the sedimentary section at Site 1230 consists of predominantly biogenic Holocene and Pleistocene sediments with varying amounts of siliciclastic components (Unit I; 0–215.8 mbsf). Unit I overlies Miocene sediments that probably belong to the accretionary prism of the Peru Trench (Shipboard Scientific Party, 1988). Although diatom ooze is the main component in most of the Unit I sediments, differences in color and in the relative amount of the terrigenous component suggested a further lithostratigraphic subdivision into four subunits. Subunit IA is a green spicule- and quartz-bearing clay-rich diatom ooze interbedded with brown bioturbated diatom and nannofossil ooze layers. The mineralogy of the nannofossil ooze layers is characterized by the presence of calcite, with smaller amounts of quartz, plagioclase, and pyrite. Small offsets resulting from high-angle normal faults were observed at the very top of Subunit IA and are commonly present throughout Unit I. Subunit IB is a dark gray to dark olive clay-rich diatom ooze that is characterized by a gradual increase in both consolidation and foliation of the sediment from top to bottom. Subunit IC consists of a mixed siliciclastic and diatomaceous sediment. Generally, its sediment is consolidated, fissile, and dark gray to black. Subunit ID is characterized by greenish brown to dark brown well-consolidated and very fissile clay-rich diatom ooze. Poor core recovery in the lower part of Site 1230 made it difficult to establish the boundary between Units I and II. However, the boundary was placed at 215.8 mbsf because downhole logging data indicate a distinct break in resistivity and bulk density at that depth, and very fractured layers are present just below that depth. This boundary, which probably represents a tectonized unconformable contact between Pleistocene and Miocene sediments, is also characterized by a hard layer of authigenic dolomite that may be the product of fluid flow along the tectonic surface. Sediments of Unit II are very consolidated and fissile. They often show a pervasive slaty fabric, which accounts for tectonic deformation in an accretionary prism. Their main composition is clay- and quartz-rich diatom ooze.

BIOGEOCHEMISTRY

Interstitial Water

The 115 IW samples for Site 1230 (Table T2) were collected (1) to define chemical gradients, especially around the anaerobic oxidation of methane (AOM) zone and gas hydrate intervals, and (2) to augment routinely measured species with nonroutine analyses of biogeochemically important species. A total of 73 IW samples were taken from Hole 1230A at a resolution of three per core in order to delineate key chemical horizons and to collect sufficient water for the numerous shore-based requests. From Hole 1230B, 32 IW samples, including 17 samples

T2. Dissolved species in IW, p. 89.

from Core 201-1230B-2H, were taken. This sampling was primarily aimed at constructing high-resolution chemical profiles across the AOM zone as determined by sulfate measurements in Hole 1230A. Eleven samples were taken from Hole 1230C to provide a chemostratigraphic link across the AOM zone between Holes 1230B and 1230C, the latter sampled mainly for microbiology. A WSTP sample was also collected at 10 m above the seafloor.

The most apparent change in interstitial water composition at Site 1230 is color (Fig. F3A). Interstitial water becomes yellow at many Deep Sea Drilling Project (DSDP) and ODP sites drilled into organic-rich sequences. At Site 808 (Nankai accretionary prism), one of the few locations where this yellowness has been quantified, the color probably correlates to dissolved organic carbon (You et al., 1993). Interstitial water at the top of the Site 1230 sequence is clear but rapidly becomes yellow with depth, reaching a golden color (>0.50 JWBL) by 40 mbsf. Below ~160 mbsf, the water begins to clear. Interstitial water below 220 mbsf is nearly clear (<0.15 JWBL).

Broadly tracking the yellowness of water, the profiles of alkalinity and DIC (Fig. F3B, F3C) covary ($r^2 > 0.98$). Alkalinity increases sharply from 2.7 mM at the seafloor to 100 mM at ~30 mbsf and less rapidly to a broad maximum of 150–157 mM between 100 and 150 mbsf. Alkalinity then decreases to ~40 mM at 250 mbsf. DIC increases rapidly from 2.6 mM at the seafloor to 100 mM at ~30 mbsf and less rapidly to a broad maximum of 155–163 mM between 100 and 150 mbsf. DIC then decreases to between 50 and 80 mM below 250 mbsf. Both alkalinity and DIC concentrations are slightly lower in depth intervals where gas hydrates were present or suspected (Cores 201-1230A-15H, 18H, and 19H). The alkalinity profile is similar to that reported for the upper 250 mbsf at Site 685 (Shipboard Scientific Party, 1988). The large increase in alkalinity and DIC at Site 1230 probably corresponds to an interval of intense methane production.

Dissolved silica concentrations rapidly rise from ~500 µM near the sediment/water interface to ~900 µM at 1.5 mbsf (Fig. F3D). From this depth to ~250 mbsf, silica concentrations show considerable scatter between 750 and 1050 µM. Concentrations appear to rise slightly at the bottom of the hole. Biogenic opal solubility probably controls the overall shape of the silica profile. However, as in gas-charged sediments at the Blake Ridge (Paull et al., 1996, p. 131), the dissolved silica content of individual samples may have decreased during whole-round storage prior to squeezing.

Ammonium increases downhole from 1000 µM within 1 m of the sediment/water interface to a broad subsurface maximum of 35,000–40,000 µM between 100 and 200 mbsf (Fig. F3E). Ammonium concentrations then decrease toward the bottom of the hole. Four main processes probably control the shape of the overall ammonium profile: organic matter degradation, microbial uptake, diffusion, and adsorption onto clays.

As highlighted during ODP Leg 112 (Suess, von Huene, et al., 1988), maximum concentrations of dissolved phosphate are >500 µM at this location. These are among the highest values reported for an ODP/DSDP location. Our phosphate profile (Fig. F3F) generally traces the low-resolution record reported by Leg 112 scientists but contains some unexplained deviations. Phosphate concentrations rise steadily and steeply from near zero at the sediment/water interface to 400 µM by 20 mbsf. Below this depth, unlike at Site 685, dissolved phosphate concentrations show considerable scatter, with values ranging between 0 and

F3. Dissolved species in IW, p. 49.

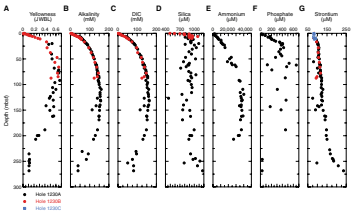

660 µM. As with silica, the interval of scatter broadly coincides with an inferred depth range of extreme degassing during core recovery and processing.

Dissolved strontium concentrations increase rapidly from 82 µM at the sediment/water interface to 105 µM at 20 mbsf (Fig. F3G). Below this depth, strontium slowly increases to 150 µM at ~210 mbsf. However, several excursions to lower values are superimposed on this general concentration gradient. At ~250 mbsf, strontium concentrations again rise quickly, reaching 235 µM at 270 mbsf. The overall shape of the downhole strontium profile mimics the low-resolution profile obtained at Site 685 (Kastner et al., 1990), except that the absolute values often differ by as much as 20%. The mean strontium concentration measured in six samples of International Association for the Physical Sciences of the Ocean (IAPSO) standard seawater was 88 ± 1 µM, which compared well to the certified value of 87 µM. The scattered low values between 50 and 90 and between 125 and 150 mbsf may indicate samples that were affected by carbonate precipitation prior to squeezing. Alternatively, some of the excursions may reflect dilution by dissociated gas hydrate.

Dissolved lithium concentrations remain close to bottom-water concentration (28 µM) until ~25 mbsf (Fig. F3H). With the exception of several deviations to lower concentrations near 80 and 150 mbsf, lithium then steadily rises to 215 µM at ~170 mbsf. Below this depth, lithium rapidly increases to 670 µM at ~270 mbsf. Carbonate recrystallization at shallow depths, a process that incorporates lithium, probably causes the significant curvature in the upper 50 m. Lithium-rich waters at depth also exert a strong control on the overall profile, although the source of these waters is unknown.

The downhole chloride profile at Site 1230 (Fig. F3I) exhibits three features characteristic of chloride profiles in sediment sequences with significant gas hydrate (e.g., Cascadia Margin [Westbrook, Carson, Musgrave, et al., 1994] and Blake Ridge [Paull, Matsumoto, Wallace, et al., 1996]). Chloride concentrations increase from bottom-water concentration (555 mM) to a shallow subsurface maximum of 568 mM at 20 mbsf. Concentrations then decrease rapidly to reach a baseline value, which lies between 550 and 555 mM at Site 1230. Superimposed on this baseline are significant deviations to lower values. For example, Sample 201-1230-19H-1, 135–150 cm, has a chloride concentration of 388 mM. A commonly held explanation for this characteristic chloride profile includes four components (Hesse et al., 1985; Egeberg and Dickens, 1999; Davie and Buffett, 2001): (1) gas hydrate formation at shallow depth excludes chloride (and other dissolved ions), which then advect or diffuse to water of lower concentration, including overlying bottom water; (2) burial of sediment eventually brings the solid gas hydrate to depths where it is no longer stable and dissociates, releasing freshwater and lowering the average chloride concentration of the sediment column; (3) dissociation of gas hydrate in discrete horizons during core recovery leads to anomalous freshening beyond baseline concentration; and (4) finally, the drop in seawater chloride since the last glacial maximum followed by diffusion decreases chloride concentration in the uppermost sediment. Interestingly, the shallow chloride maximum is more pronounced and the baseline concentration is higher at Site 1230 than at sites on the Blake Ridge, one of the few other locations with gas hydrates and high-resolution IW profiles. These characteristics may indicate stronger upward flow and a lower total amount of gas hydrate at Site 1230 than the 0.2 mm/yr and average 5% occupancy of pore space

inferred for the Blake Ridge (Egeberg and Dickens, 1999). Alternatively, the location of the chloride peak may reflect the top of the hydrate zone. It should be noted that the chloride concentrations reported here include bromide and iodide, which together are >3 mM at this location (Martin et al., 1993).

Recent literature has emphasized that sulfate profiles are steep and nearly linear in regions with significant upward transport of methane and gas hydrates (Borowski et al., 1996, 1999; Hoehler et al., 2000). Sulfate concentrations were determined for the WSTP sample and 44 IW samples from shallow depth. In all three holes, sulfate decreases from typical seawater concentrations at the seafloor (28.9 mM in the WSTP sample) to <0.80 mM at shallow depth (Fig. F3J). In Hole 1230B, where high-resolution sampling was conducted, sulfate drops almost linearly with depth ($R^2 > 0.998$) to 0.64 mM at 9.0 mbsf. This steep, nearly linear decrease of 3.2 mM/m strongly suggests that AOM consumes a large fraction of the sulfate over a thin zone (Borowski et al., 1996; Niewöhner et al., 1998; Fossing et al., 2000). This inference is supported by the steep increase in headspace methane concentration beginning at ~7 mbsf (Fig. F3K).

For samples from Holes 1230B and 1230C, the preparation of samples was changed to maximize analytical sensitivity at low sulfate concentrations. Interestingly, these analyses show that the steep sulfate gradient in shallow sediment does not extend to zero sulfate concentration immediately below the sulfate/methane interface, as purported to occur elsewhere. Instead, sulfate decreases gradually below 9.0 mbsf, reaching zero concentration at ~30 mbsf (Table T2). Addition of sulfate during the squeezing process (e.g., oxidation of through sulfides) was excluded as an explanation for these anomalous sulfate values because samples processed similarly but obtained from deeper depths at Site 1230 or from other sites of Leg 201 had zero sulfate. Hence, upon recognizing this phenomenon in Hole 1230B, two hypotheses were forwarded: (1) oxidation of sulfide during storage adds sulfate to the water or (2) a solid sulfate-bearing phase (e.g., barite, below) slowly dissolves upon entering sulfate-depleted water. To address the first hypothesis, IW samples from Hole 1230C were squeezed in opposite order from those in Hole 1230B and analyzed within minutes. Despite this approach, IW samples from similar depths in Holes 1230B and 1230C (after correcting for core offsets, below) contain similar sulfate. Additionally, three samples of squeezed water from Hole 1230A were reanalyzed after 4 days to examine the potential effect of oxidation (Table T3). No significant oxidation was observed over this 4-day period (~0.15 mM compound to <0.2 mM). Minor amounts of sulfate are probably present over an extended depth interval below the main AOM zone, although we cannot rigorously support barite dissolution as an explanation based on available information.

Interstitial water barium (Fig. F3L) spans a wide concentration range at Site 1230, as somewhat expected from limited analyses at Site 685 (von Breymann et al., 1990). Dissolved barium is between 0.4 and 10 µM in the uppermost 7 m, a concentration range that already exceeds that at most ODP sites examined for this element. Beginning at ~7 mbsf, which coincides with the increase in headspace methane (Fig. F3K), barium concentrations rise rapidly to 265 µM at ~20 mbsf. Below this depth, the barium concentrations steadily decrease, resulting in barium concentrations of ~400 µM between 50 and 150 mbsf. From this depth to 270 mbsf, dissolved barium climbs to nearly 1200 µM. To our knowledge, this is the highest concentration ever reported in a deep

T3. Sulfate analyses before and after storage, p. 92.

marine borehole. Superimposed on this overall profile is a series of excursions to lower values. Several processes likely contribute to the complex barium profile at Site 1230. First, the occasional barium data that lie well below the general trend probably reflect dilution by gas hydrate dissociation or, in some cases (e.g., Sample 201-1230A-8H-1, 135–150 cm), contamination by borehole water. Given the low K_{sp} of barite (~10^{-10}) (Monnin, 1999) and the exceptional barium concentrations, even a trace incursion of sulfate will lead to barite precipitation. Second, dissolved barium (and strontium, above) appears to be precipitating into some solid phase between 50 and 150 mbsf. Third, and most importantly, extreme dissolution and precipitation of barite around the sulfate/methane interface (Torres et al., 1996; Dickens, 2001) has led to the incredibly high dissolved barium concentrations at Site 1230. Solid barite, associated with primary productivity in the water column, is deposited on the seafloor and buried over time into the sulfate-depleted zone, where it dissolves. Dissolved barium then advects or diffuses upward to the sulfate-rich zone, where it precipitates. Shallow sediment at Site 685 contains high solid-phase barium concentrations (~1000 ppm) that are likely present as barite (von Breymann et al., 1990). Apparently, at Site 1230, the extreme input of barite over time has led to high interstitial water barium concentrations.

The total dissolved sulfide ($\Sigma H_2S = H_2S + HS^-$) profile at Site 1230 (Fig. **F3M**) can be divided into two distinct zones: a shallow zone between 0 and 25 mbsf, where sulfide is generally high, and a deep zone between 25 and 268 mbsf, where sulfide is low. Sulfide is first detected (0.0054 mM) at a depth of 0.04 mbsf. Below this depth, sulfide increases steeply and linearly with increasing depth, reaching maximum concentrations (to 10.9 mM) over a narrow depth zone from 7 to 9 mbsf. Below this peak, sulfide concentrations decrease to <0.002 mM at 27 mbsf. The sulfide peak is nearly symmetrical in the uppermost 18 m of sediment but shows concave-upward curvature between 17 and 25 mbsf, suggesting uptake of sulfide into the solid phase within this layer. Below 25 mbsf, sulfide concentrations remain low, usually <0.001 mM.

As at the other sites of Leg 201, the dissolved iron profile at Site 1230 (Fig. **F3N**) shows considerable downhole scatter but with an obvious association to sulfide. Except in the top 1.5 m, where they decrease from ~19 to 3 µM, dissolved iron concentrations are low (<5 µM) between the sediment/water interface and 25 mbsf. Beginning at this depth, dissolved iron abruptly increases, ranging between 5 and 60 µM until 200 mbsf. Dissolved iron concentrations are <10 µM below 200 mbsf. The overall dissolved iron profile likely reflects the dissolution and precipitation of solid iron phases. Iron oxides and hydroxides are deposited on the seafloor. Within the upper few centimeters, these phases dissolve, releasing iron, which then precipitates as one or more iron sulfide minerals. In sediment deeper than 25 mbsf, where neither sulfide nor oxygen is present, iron-bearing solids again dissolve, releasing iron to the interstitial water. These solids could be aluminosilicates, oxides that have escaped shallow diagenesis, or sulfides entering sulfide-depleted water.

Although dissolved manganese concentrations are generally low (<8 µM) at Site 1230, the downhole profile (Fig. **F3O**) displays two intriguing features. First, after increasing to a peak of 7.3 µM at 0.65 mbsf, dissolved manganese concentrations sharply decline to below detection limit (0.1 µM) at 5 mbsf. Second, below this depth dissolved manganese concentrations oscillate to form several well-defined peaks and troughs

with amplitudes of ~1.5 µM. Manganese oxides probably dissolve in the uppermost 1 m of sediment, releasing dissolved manganese to the interstitial water, which is subsequently reduced by microorganisms. In the interval of high sulfide between 1 and 25 mbsf, sulfide phases may incorporate manganese. Below 25 mbsf, there is a balance between dissolution of manganese-bearing solids, again either aluminosilicates, oxides, or sulfides and precipitation.

Concentrations of acetate and formate were determined for 68 samples from Holes 1230A and 1230B, including a water sample obtained from sediment containing a high portion of gas hydrate (Table **T2;** Fig. **F3P, F3Q**). Acetate concentrations range from 3.3 to 220 µM and significantly exceed those at previous Leg 201 sites. In general, the acetate profile shows three concentration zones. From the sediment/water interface to ~13 mbsf, concentrations are mostly <20 µM. Between 13 and 133 mbsf, acetate concentrations range from 20 to 60 µM. Acetate concentrations then increase sharply below this depth, dropping below 100 µM in only a few samples. It is noteworthy that the sudden increase in acetate concentrations occurs in an interval with relatively high amounts of methane hydrate (see **"Gas Hydrate,"** p. 35), although a potential link is not obvious. Acetate is depleted in water released from dissociated gas hydrate (see **"Gas Hydrate,"** p. 35). In contrast to the acetate profile, formate concentrations display significantly less variation downhole. Formate concentrations range from 2.9 to 41 µM, with almost all values <10 µM. Formate concentrations display a slight trend to higher values with increasing depth.

Hydrogen incubations were conducted on 18 samples from Hole 1230A and 5 samples from Hole 1230C. All samples were incubated at 4°C, close to the in situ sediment temperature (see Table **T4** for details). Hydrogen concentrations ranged from 0.07 to 1.4 nM and did not display a systemic downhole trend.

T4. Hydrogen concentrations, p. 93.

Headspace methane concentrations, as determined by analyses after 7 days at 22°C, are generally higher than those at previous sites (Table **T5;** Fig. **F3K**). Methane concentrations are <100 µM between the sediment/water interface and ~7 mbsf. Below this depth, where sulfate drops to <0.80 mM, methane concentrations rise sharply, reaching 7000 µM by ~18 mbsf. Of all sites studied during Leg 201, Site 1230 displays the steepest sulfate gradient in shallow sediment. Below 18 mbsf, methane concentrations determined by the headspace technique slowly and erratically decrease downhole. The methane profile between 0 and 18 mbsf may represent in situ methane concentrations. However, as highlighted by methane-rich gas voids in sediment cores (Table **T6;** see **"Lithostratigraphy"** p. 7), the scattered methane profile below 18 mbsf undoubtedly reflects differential gas loss during core recovery, the intensity perhaps linked to lithology. The in situ methane concentrations are probably >300 mM in lower parts of the sediment sequence at Site 1230, as indicated by results from the PCS (see **Dickens et al.,** this volume). As at all sites of Leg 201, methane concentrations derived from the safety methane protocol are generally lower than those obtained from the more time-consuming extraction in NaOH solution (see **"Biogeochemistry,"** p. 9, in the "Explanatory Notes" chapter).

T5. Hydrocarbon gas concentrations, p. 94.

T6. Gas analyses of vacutainer samples, p. 96.

Ethane and propane comprise trace gas components in the majority of headspace samples from Site 1230 (Table **T5;** Fig. **F3S**). Interestingly, there is a clear downhole change in the amount of these gases. Ethane and propane concentrations are <1 µM in the top 200 mbsf, excluding one sample at 26.60 mbsf (Sample 201-1230A-4H-2, 130–135 cm) that yielded unusually high concentrations of both gases during analysis ac-

cording to the safety protocol (171.7 ppm ethane and 287.1 ppm propane; ~35 and 55 µM). Below 220 mbsf, ethane and propane concentrations increase drastically, reaching 12 µM, although their abundances do not correlate in detail. The apparent increase in ethane and propane at depth may indicate an interval of in situ production by microbial activity or upward flow of gas.

High-resolution recovery of the well-characterized AOM zone at Site 1230 represents an important goal of Leg 201. However, studies and sampling of this interval need to account for meter-scale depth offsets between holes that often occur during drilling operations (e.g., Hagelberg et al., 1992). In the absence of obvious physical property changes to correlate, we have aligned Holes 1230A, 1230B, and 1230C using the dissolved sulfate and barium profiles (Fig. F4). This correlation (Fig. F5), based on a continuous Hole1230B, implies a 0.5-m gap between Cores 201-1230A-1H and 2H and missing or compressed mudlines in Holes 1230A and 1230B.

Rock-Eval Pyrolysis

Rock-Eval pyrolysis was determined on selected sediment samples from Site 1230 as well as other Leg 201 sites for comparison. These data from all sites are presented and discussed here for brevity. Sediment samples from Site 1228 are from the IW squeeze cakes; all other samples are from split cores.

The results of Rock-Eval pyrolysis (Table T7; Fig. F6) show that sediments at most Leg 201 sites contain thermally immature organic carbon, with total organic carbon (TOC) concentrations often >1%. TOC concentrations at Site 1230 range from 0.7% to 5.2%, with most values falling between 2% and 4%. Hydrogen index (HI) values at Sites 1227–1229 are generally high and consistent with organic matter being primarily derived from marine algae (Tissot and Welte, 1984). As a group, Site 1228 samples have the highest HI and Site 1230 samples have the lowest HI. All samples but one from Site 1231 have TOC <0.5%.

MICROBIOLOGY

Microbiological sampling at Site 1230 covered the shallow sulfate-reducing zone near the sediment/water interface (0–8 mbsf), the transition between the sulfate-rich surface layers and the sulfate-depleted methanogenic deeper sediment layers (8–12 mbsf), and the deep sediment layers down to 268 mbsf. The upper 20 m of the sediment column was characterized by steep biogeochemical gradients. This interval was sampled in at least two sections per core for DNA and FISH-SIMS analysis, measurements of sulfate reduction rates, hydrogen concentration and turnover, methanogenesis rates, acetate turnover, thymidine incorporation, bacterial lipid biomarkers, adenosine triphosphate, FISH, and iron/manganese/sulfur solid phases (Fig. F7) (Cores 201-1230A-1H through 3H). The deeper sediment layers were sampled on average every 15 m (Cores 201-1230A-4H through 38X).

Sampling in Hole 1230B focused on Core 201-1230B-2H. This core included the interface where the steep, decreasing sulfate gradient leads into a zone where sulfate concentrations remained <1 mM but do not approach zero for at least 2 m (~8–10 mbsf). In order to sample this low-sulfate zone in fine spatial resolution, Sections 201-1230B-2H-2, 2H-3, 2H-4, and 2H-5 were divided into three subsections. Each of these sub-

F4. Barium and sulfate profiles, p. 52.

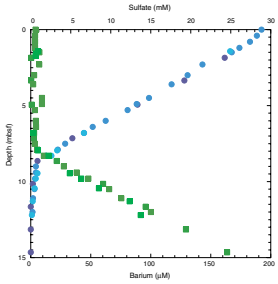

F5. Correlation of the top two cores in each hole, p. 53.

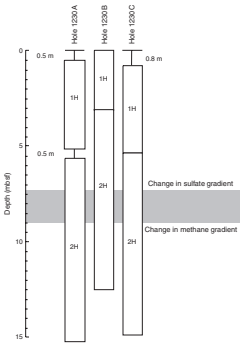

T7. Rock-Eval pyrolysis, p. 97.

F6. Downcore TOC profiles, p. 54.

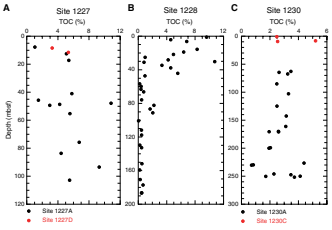

F7. Subsampling for MBIO, Hole 1230A, p. 55.

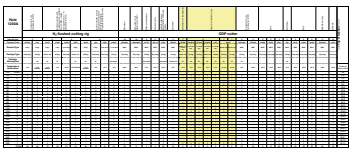

sections was sampled for interstitial water, DNA, and biomarker analyses (Fig. F8). In this way, microbial population gradients obtained from DNA and biomarker analyses can be connected directly to the sulfate profile and other interstitial water data. In addition, the sediment surrounding a gas hydrate nodule in Section 201-1230B-12H-2 was sampled with 5-cm³ syringes (see "Lithostratigraphy," p. 7, and "Biogeochemistry," p. 12).

A similar strategy was followed in Hole 1230C. Here, the sampling scheme for Sections 201-1230C-2H-2, 2H-3, 2H-4, and 2H-5 included activity determinations (sulfate reduction measurements and acetate turnover measurements), cultivations, biomarker and DNA analyses, and an interstitial water sample at the top of each section (Fig. F9). The interstitial water sample was analyzed immediately for sulfate to allow precise correlation of the sampling scheme to the sulfate profile in the low-sulfate zone before the actual microbiology sampling started. In particular, the area of the most detailed sampling was centered on the 7.5- to 9.7-mbsf depth interval, where the steep sulfate gradient of the upper sediment column turned into the low-sulfate zone (8.5- to 9-mbsf interval in Section 201-1230C-2H-3). In order to cluster as many samples as possible around this interface, DNA samples and enrichment samples were taken in 5-cm³ syringes (combined enrichments) (Fig. F9) from a single whole-round core (WRC) section rather than as separate WRC samples (Fig. F9). These integrated sampling strategies are necessary at key biogeochemical horizons, when a resolution of ≤1 m is required.

Samples from the overlying "slop" (liquid mixture of surface sediment and water) were taken from Core 201-1230C-0 for experiments to evaluate the effects of pressure on microbial activity measurements (sulfate reduction, thyridine incorporation, acetate turnover, and bicarbonate reduction) and for total cell counts, FISH, and thermophile enrichments.

Total Bacterial Enumeration

Samples of 1-cm³ plugs for total prokaryotic cell enumeration were taken during core processing in the 10°C refrigerator from Holes 1230A, 1230B, and 1230C. From Hole 1230A, 24 samples were taken between 1.11 and 268.65 mbsf. The majority of these samples were processed immediately. From Hole 1230B, 29 samples were taken between the surface of the sediment column and 81.83 mbsf. These samples were concentrated between Section 201-1230B-2H-2 and 2H-5 and were designed to provide high-intensity sampling through the sulfate–methane transition. Most of these will be processed as part of shore-based activities. Two samples were also taken in Hole 1230C at 7.75 and 8.04 mbsf (Samples 201-1230C-2H-3, 25–30 cm, and 2H-3, 54–55 cm). These last samples were specifically targeted at the sulfate–methane transition and will also be processed on shore. Prokaryotes were present in all samples studied, to the depth of 257.70 mbsf (Fig. F10). The highest number of prokaryotes was found near the surface (Sample 201-1230B-1H-1, 0–1 cm), in a sample that contained 4.21×10^8 cells/cm³. The lowest number was at the base of the hole, with 1.28×10^6 cells/cm³ (Sample 201-1230A-37X-1, 10–14 cm). This is a 330-fold difference between the cell concentration of the sediment/water interface and that of this deepest sample.

The overall depth profile of cell numbers per cubic centimeter follows a trend observed at other ODP sites (Parkes et al., 1994); many of

F8. Subsampling for MBIO, Hole 1230B, p. 56.

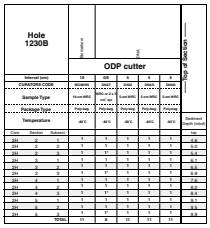

F9. Subsampling for MBIO, Hole 1230C, p. 57.

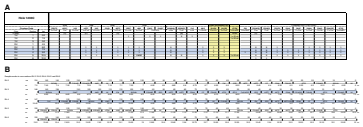

F10. Prokaryotic cells enumerated, p. 58.

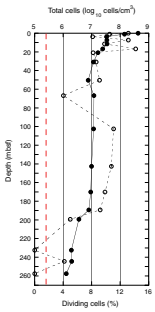

the data points lie very close to or on the mean regression line for all previously enumerated sites (Fig. **F11**). There are two increases of note in the Site 1230 record. First, between ~7 and 21 mbsf (Samples 201-1230A-2H-2, 110–115 cm, and 3H-5, 68–78 cm) there is a small increase coincident with the sulfate–methane transition and the upper part of the methanogenic zone. Second, there are nearly sustained constant cell numbers between ~66 and 190 mbsf (Samples 201-1230A-9H-5, 132–138 cm, and 201-1230A-24H-2, 71–77 cm). The reasons for this plateau in prokaryotic numbers are unclear, although it is coincident with a bulge in many of the interstitial water geochemical profiles (see Fig. **F3**).

Numbers of dividing cells (suggested as an index of growth activity) are typically <10% of the total count. As expected, dividing cells as a percentage of the total count are high near the surface (Fig. **F10**). They then decrease to ~9% between 20 and 50 mbsf. After a single low datum they then increase to 10%–11% over the depth range of the plateau in total cell numbers. This may indicate that between 60 and 190 mbsf continuing growth contributes to this plateau in prokaryotic cell numbers. Below 190 mbsf, total cell numbers decrease to $<1 \times 10^7$ cells/cm^3 and percent dividing cells becomes unreliable. Nevertheless, there appears to be a substantial decrease in percent dividing cells, and on two occasions zero was recorded.

At 216 mbsf, there is a discontinuity in the sediment column where, during accretion, the upper layers of sediment were removed and replaced by younger sediment, leaving a hiatus of ~4 Ma. When this site was previously cored (Shipboard Scientific Party, 1988) at Site 685, the data were not sufficiently constrained to accurately identify this boundary. If there are missing sediment layers, then prokaryotic cell counts in the lower sediments would appear to be smaller than expected for their current depth in the sediment column. Therefore a step-down in numbers would be visible in the total prokaryote profile. Such a step is observed between ~170 and 230 mbsf (Fig. **F12**). Taking the tangents of a smoothed curve over the lower and the upper part of the cell number profile, the intersection of the tangents provides an estimate for the boundary of 214 mbsf.

The nature of the sediments at this site made direct counting more problematic than usual. Where subsamples of 15–40 µL can generally be processed, in this case subsample size was restricted to a maximum of 8–12 µL. Consequently, the detection limit increased to 2.5×10^5 cells/cm^3 and counting sensitivity decreased. The percentage of dividing cells should be viewed with caution where the direct count is $<1 \times 10^7$ cells/cm^3.

F11. Total prokaryote profile, p. 59.

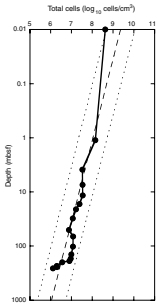

F12. Prokaryotic cell numbers, 65–245 mbsf, p. 60.

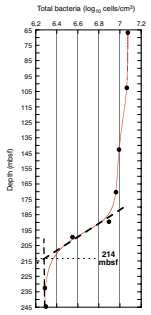

Contamination Tests

While drilling cores for microbiology, the potential for contamination with bacteria from the surface is highly critical. Contamination tests were continuously conducted using solutes (PFT) or bacterial-sized particles (fluorescent microspheres) to check for the potential intrusion of drill water from the periphery toward the center of cores and thus to confirm the suitability of the core material for microbiological research. We used the chemical and particle tracer techniques described in ODP *Technical Note* 28 (Smith et al., 2000). Furthermore, the freshly collected cores were visually examined for possible cracks and other signs of disturbance by observation through the transparent core liner. Core sections observed to be disturbed before or after subsampling were not an-

alyzed further. Such disturbance phenomena are critical to the integrity of the core material and therefore also to its usefulness for microbiological studies.

Perfluorocarbon Tracer

The PFT was injected continuously into the drilling fluid during drilling of Holes 1230A, 1230B, and 1230C (see "Perfluorocarbon Tracer Contamination Tests," p. 26, in "Microbiological Procedures and Protocols" in "Microbiology" in the "Explanatory Notes" chapter). PFT sampling focused on microbiology cores and especially on sections that were used for slurry preparation and cultivations. Two 5-cm^3 subcore samples were taken at the core center and pooled for PFT measurement. In parallel, a 5-cm^3 subcore sample was taken at the core periphery, adjacent to the core liner, to compare the PFT concentrations in the center of a core to the PFT concentrations at the periphery of the same core, and to assess the difference in contamination potential. Whenever possible, the samples were taken directly on the catwalk and capped away from nearby cores because the PFT content of catwalk air was usually not detectable.

With three exceptions, low levels of potential seawater contamination (<0.05 µL seawater/g sediment) were found for the center portions of all tested APC cores of Holes 1230A, 1230B, and 1230C (average = 0.08 µL seawater/g sediment) (Table T8). The three exceptions, which may have been contaminated, are samples from Cores 201-1230A-13H and 22H and 201-1230C-1H. The outer portions of all tested cores had significantly high levels of PFT tracer and potential seawater contamination (mostly >0.15 µL seawater/g sediment; average = 0.71 µL seawater/g sediment). XCB cores showed higher PFT concentrations than did APC cores (for center portions, average = 0.24 µL seawater/g sediment; for outer portions, average = 2.74 µL seawater/g sediment). Three of the four XCB cores sampled exhibit PFT concentrations in the center that suggest potential prokaryotic cell contamination from seawater drilling fluid (>0.2 µL seawater/g sediment). In almost all cases for both APC and XCB cores, the PFT content and the estimated potential seawater contamination levels were higher in the periphery of the core than in the center.

T8. Seawater contamination based on PFT, p. 99.

Of the 11 slurry samples taken from Site 1230 (Table T9), only the slurries from Cores 201-1230A-1H, 31X, and 38X showed concentrations of PFT that suggest potential microbial contamination from seawater drilling fluid. Assuming 5×10^8 prokaryotic cells/L surface seawater, each 0.1 µL of seawater contamination may represent as many as 50 contaminating cells if the sediment is porous enough to allow cells to travel with the PFT.

T9. Potential contamination of slurries based on PFT, p. 100.

In order to assess the relationship of PFT contamination to particulate contamination (such as microorganisms), nine of the sediment samples for which PFT concentrations had been determined were further analyzed for bead contamination (Table T8). No beads were found in APC samples with low PFT values (corresponding to ≤0.02 µL seawater contamination/g sediment). Six beads were found in 50 fields counted for a sample with as much as 0.22 µL seawater contamination/g sediment. This latter count represents 76 beads/g sediment. Considering the extremely high number of beads deployed (1.7×10^{11} in this case), 76 beads/g sediment most likely represents far fewer actual contaminating microorganisms. The results of these comparisons suggest that samples with PFT contaminations representing less than ~0.02 µL

contaminating seawater/g sediment were not contaminated with microorganisms during the drilling and sample processing.

Particulate Tracer

Fluorescent microspheres (beads) were deployed on all seven cores from which slurries were intended to be made at this site (Table T10). However, because of variable sediment quality, on two occasions slurries were made from adjacent cores in which beads had not been deployed. Thus, only five slurries could be examined for bead contamination (Table T10). For each slurry two subsamples were processed: (1) a sample of the slurry to check contamination and (2) a scraping from the outer surface of the core to confirm deployment of beads.

Bead deployment was confirmed from the outer core scrapings in five of six cores that were sampled for slurry preparation (Table T10). Beads were detected in one slurry sample (Sample 201-1230A 38X-1, 65–71 cm) at low levels, but nevertheless at levels that suggested potential contamination. This was the only XCB core used for slurry preparation, and XCB cores, because of the way they are obtained, have a higher potential for contamination compared to APC cores. The slurries made from Sections 201-1230C-2H-2 through 2H-5 were low volume and insufficient for bead analysis. PFT analysis however, suggested that Core 201-1230C-2H was free of contamination.

T10. Potential contamination of slurries based on beads, p. 101.

Cultivations

Depths were selected for cultivation in order to cover the entire drilled sediment column (Hole 1230A) and especially the sulfate–methane transition zone (Hole 1230C). Additionally, samples taken close to hydrate layers were used for enrichments. The media inoculated are selective for fermenters, sulfate reducers, methanogens, and various anaerobic chemolithoautotrophic and heterotrophic prokaryotes that use iron(III) or manganese(IV) as an electron acceptor. Quantitative cultivations (MPN experiments) and enrichment cultures were started at temperatures between 4° and 80°C (Table T11). As it is known that aerobic prokaryotes may also be present in strictly anoxic environments, several MPN experiments for aerobic prokaryotes (media with suffix -ox) were started at this site to compare with the anoxic assays (Table T11).

T11. Media inoculated with material from Site 1230, p. 102.

FISH-SIMS

^{13}C substrate incubations were initiated for postcruise analysis by FISH-SIMS using material from Cores 201-1230A-2H, 9H, 15H, and 38X. In these cases, 10 mL of the master slurry was injected into each bottle. The ^{13}C substrates used were methane, acetate, and glucose. Glucose was used in Cores 201-1230A-9H, 13H, 15H, and 38X. Acetate was used at all depths except Core 201-1230A-38X, with multiple bottles at each depth. Methane was used at all depths, with multiple bottles used for samples from Cores 201-1230A-2H and 38X.

PHYSICAL PROPERTIES

At Site 1230, one deep hole (Hole 1230A; 278.3 mbsf penetration), one intermediate-depth hole (Hole 1230B; 105.0 mbsf penetration) and

three shallow holes (Holes 1230C, 1230D, and 1230E; <15.0 mbsf penetration) were cored. Physical property measurements conducted on cores from all holes ranged from standard-resolution multisensor track (MST), IR camera imaging, and discrete sample property measurements on Hole 1230A cores, to IR camera and MST runs on Hole 1230B cores, to only MST runs on cores from the subsequent holes (Holes 1230C–1230E), with high-resolution acquisition on Hole 1230D. Continuous IR imaging was conducted on the catwalk prior to microbiological or interstitial water whole-round core sampling. MST data were obtained from all intact whole-round cores that were not used for microbiological and geochemical sampling. These MST data provide a good near-continuous record of physical property variation from the seafloor to 135 mbsf. For sediments recovered from below 135 mbsf, APC injection disturbance, degassing, and depressurization expansion artifacts almost completely destroyed the in situ sediment fabric. As a result, accurate electrical resistivity (formation factor) measurements were not possible and *P*-wave velocities were only obtained for discrete samples from the upper ~155 mbsf and from 230 to 245 mbsf. The *P*-wave logger (PWL) on the MST track was turned off after running the first core (~10 m) in Hole 1230A because the data were inconsistent for the reasons mentioned above.

Each section of whole-round core analyzed for physical properties was degassed on the catwalk (up to 2 hr, if necessary for safety, due to high hydrogen sulfide levels), equilibrated to laboratory temperature (2–4 hr), and then run on the MST. The standard-resolution measurements were magnetic susceptibility (spacing = 5 cm, data acquisition scheme [DAQ] = 2 × 1 s), gamma ray attenuation (GRA) density (spacing = 10 cm, count time = 5 s), and NGR (spacing = 30 cm, count time = 15 s). Thermal conductivity measurements were made on the third section of each whole-round core in Hole 1230A, where possible.

Moisture and density (MAD) properties and *P*-wave velocity from the digital velocimeter (PWS3) were collected at a frequency of one per section, where possible, and at higher resolution in sections with many voids or lithologic transitions. MAD samples were co-located with the methane headspace extractions, where possible, to facilitate the volumetric analysis of methane concentrations.

Instrumentation, measurement principles, and data transformations are further discussed in **"Physical Properties,"** p. 41, in the "Explanatory Notes" chapter.

Overview

Physical property data at Site 1230 can conveniently be described in terms of the lithostratigraphic subdivisions. We are able to describe the interval of low core recovery (135–225 mbsf) because of continuous triple combo and FMS-sonic tool wireline logs across this zone. All physical property data suggest a sharp boundary at 216 mbsf, the depth assigned to the Unit I/II contact (see **"Description of Lithostratigraphic Units,"** p. 8, in "Lithostratigraphy"). Above this level, variations in physical property data are small and can be interpreted in terms of sediment compositional variation, burial and compaction, and the presence of gas hydrates between 80 and 160 mbsf. GRA-based bulk density measurements are extremely noisy, reflecting depressurization and gas expansion. This process also results in artificially low density for the sediments, which masks the expected compaction signature throughout Unit I. MAD bulk density data are much less noisy, show the ex-

pected downhole compaction profile, and match the wireline density measurements except for a slight low bias of 0.06 g/cm³ in the lower half of Unit I. Whole-core magnetic susceptibility and NGR emission measurements are lower than in situ values because of volumetric expansion during recovery. However, both data sets retain sufficient downhole variability to discriminate subunits based on these properties. We note that over the common intervals the wireline logs track the complementary physical property data extremely well, with the exception of the neutron porosity tool, which has a 12%–15% high bias relative to the corresponding MAD-derived porosity.

The trend of the bulk resistivity data best defines the Unit I/II boundary with stationary trends above and below a 1.6-Ωm increase at 216 mbsf. Below 216 mbsf (Unit II), MAD density is higher than that in Unit I but the GRA density data are inconsistent because of degassing effects. On average, grain density, magnetic susceptibility, and *P*-wave velocity are all slightly higher in Unit II than in Unit I. The downhole records of each physical property are described and interpreted in detail below. The correlation between gas hydrates and physical properties is discussed in "Gas Hydrate," p. 35.

Infrared Scanner

Each core from Holes 1230A and 1230B was scanned with an IR camera immediately upon its arrival on the catwalk (see "Infrared Thermal Imaging," p. 42, in "Physical Properties" in the "Explanatory Notes" chapter), except when the cores were very short or when hydrogen sulfide was a safety hazard. A key improvement at Site 1230 was the use of the external liquid crystal display screen, which provided a live view of the core scan, allowing immediate identification of voids and cold spots. Cold spots were of particular interest at Site 1230, as they were likely indicators of the presence of hydrates. Partial automation of image analysis allowed depth-matched downhole plots to be generated within a day. Three method development goals were therefore achieved at this site: (1) development of procedures and criteria for identification of hydrates using the IR camera, (2) correlation of camera temperatures with other physical property measurements, and (3) comparison of temperature distributions between holes (1230A and 1230B).

Hydrates were visually identified in Cores 201-1230A-18H and 19H. At this time, we discovered that the core liner temperatures at hydrate locations could be as high as ~16°C rather than the 0°–10°C previously assumed. Subsequently, using the 16°C criterion, the camera identified a cold area of interest in Core 201-1230A-26H. This area was sectioned and immediately split, revealing very cold, bubbling sediment, which was interpreted as containing disseminated hydrate. A composite image of this core is illustrated in Figure **F13.** The catwalk scan minimum temperature of the intact cores was 15.7°C (Fig. **F13A**), whereas the split core minimum temperature was –1.7°C (Fig. **F13B**). Temperatures as low as –3.2°C were imaged when the core was disrupted during sampling (Fig. **F13C**).

Downhole profiles were compiled using the method described in "Infrared Thermal Imaging," p. 42, in "Physical Properties" in the "Explanatory Notes" chapter. The downhole plot of temperature recorded by the IR camera for Hole 1230A has a distinctive feature at ~70 mbsf (Fig. **F14**). At that depth, variability of core-scan temperatures increased, indicating increasingly common voids and cold spots.

F13. IR scan of Core 201-1230A-26H, p. 61.

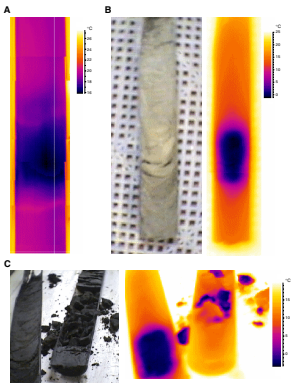

F14. Core liner temperature profile, Hole 1230A, p. 62.

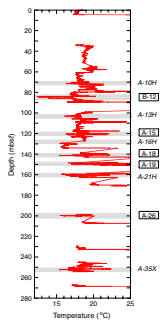

Downhole plots of core liner temperature for Holes 1230A and 1230B are compared in Figure F15. The profiles of average scan temperature correlate well above 70 mbsf, in the hydrate-free sediment. In the sediment below 70 mbsf, the complex temperature structure was not reproducible between holes.

F15. Core liner temperature profile, Holes 1230A and 1230B, p. 63.

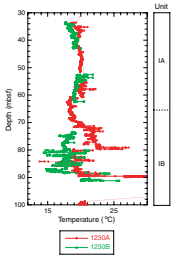

Magnetic Susceptibility

Low-field volume magnetic susceptibility was measured on the MST using the Bartington loop sensor as described in "Magnetic Susceptibility," p. 44, in "MST Measurements" in "Physical Properties" in the "Explanatory Notes" chapter. Data were collected on whole-round core sections from Holes 1230A, 1230B, 1230C, and 1229E at standard resolution (spacing = 5 cm, DAQ = 2 × 1.0 s). Hole 1230D was run at high resolution (spacing = 1 cm, count time = 10 s). Positive magnetic susceptibility is present in all cores (Fig. F16). A duplicate continuous record from Holes 1230A and 1230B is present from 0 to 90 mbsf. Below this level, the record is mostly continuous in Hole 1230A to a depth of 135 mbsf. Magnetic susceptibility was not recorded at Site 685.

F16. MST volume magnetic susceptibility, p. 64.

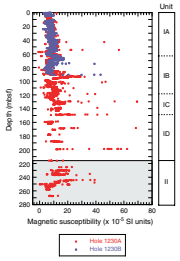

Subunit IA (0–64 mbsf), a diatomaceous and nannofossil ooze, is characterized by increasing magnetic susceptibility from ~6 × 10^{-5} SI units at the seafloor to ~13 × 10^{-5} SI units at 64 mbsf. Regular oscillations of ~8 × 10^{-5} SI units over a 2- to 3-m scale are present. The susceptibility low of 5 × 10^{-5} SI units at 58 mbsf breaks the general downhole increase in this subunit.

In Subunit IB (a clay-rich diatomaceous ooze), susceptibility declines to ~6 × 10^{-5} SI units to 82 mbsf. Between 82 and 118 mbsf, the magnetic susceptibility data fluctuate between 5 × 10^{-5} and 18 × 10^{-5} SI units, with a peak of 28 × 10^{-5} SI units at 93 mbsf. There is no apparent lithologic explanation for the oscillations over this interval, although we note gas hydrates were visually observed in the stratigraphic section at ~82 mbsf. Whether this correlation is an artifact of degassing or has some significance linked to hydrate formation remains to be investigated. At the base of Subunit IB (118 mbsf), the susceptibility is ~15 × 10^{-5} SI units.

Across Subunit IC (118–148 mbsf), magnetic susceptibility falls to ~8 × 10^{-5} SI units at 121 mbsf. It subsequently peaks at ~16 × 10^{-5} SI units at 130 mbsf. Below this level the record is incomplete, but susceptibility appears to remain at 14 × 10^{-5} to 16 × 10^{-5} SI units to the top of Subunit ID.

Subunit ID (148–218 mbsf) had poor core recovery, so its magnetic susceptibility trends are unclear. Magnetic susceptibility on recovered segments ranges from ~5 × 10^{-5} to 25 × 10^{-5} SI units.

The magnetic susceptibility record of Unit II (216–277 mbsf) is similarly incomplete. From the few intact sections available, magnetic susceptibility ranged from 5 × 10^{-5} to 25 × 10^{-5} SI units, similar to sediments in Unit I.

Paleomagnetism

At Site 1230 we collected 25 discrete samples for paleomagnetic measurements. The sampling frequency was one sample from each core from Hole 1230A (Cores 201-1230A-1H through 35X; 0–254.5 mbsf). Alternating-field (AF) demagnetization of the natural remanent magnetization (NRM) was conducted up to 40 mT in 10- or 5-mT steps. Anhys-

teretic remanent magnetization (ARM) was measured to 40 mT in 10-mT steps with a 29-µT direct current–biasing field. AF demagnetization of the ARM was conducted to 40 mT in 10-mT steps.

Lithostratigraphic Subunits IC through ID (see **"Description of Lithostratigraphic Units,"** p. 8, in "Lithostratigraphy") exhibit higher magnetic intensity of NRM after 20-mT AF demagnetization (Fig. **F17**). Demagnetization of the dark brown pyrite-bearing diatom-rich silty clay in lithostratigraphic Subunit IC reveals magnetic directions that are unstable (Fig. **F18**). In lithostratigraphic Subunit ID, magnetic intensity correlated with magnetic susceptibility despite poor core recovery (Fig. **F17**). Lithostratigraphic Subunit ID, which consists of dark brown clay-rich diatom ooze alternating with lighter olive diatom ooze, shows stable magnetization. In general, the former appears to be less fractured and brittle than the latter. The less brittle clay-rich, well-consolidated layer (Sample 201-1230A-19H-2, 10–12 cm) has a stable direction (Fig. **F19**). The fractured diatom-rich fissile layer (Sample 201-1230A-22H-1, 60–62 cm) shows a downward drilling-induced overprint (Fig. **F20**). Further demagnetization is needed to determine original directions.

Density and Porosity

Bulk density data were measured on the MST by the GRA densitometer (spacing = 10 cm, count time = 5 s, for Holes 1230A and 1230B) and were calculated from mass/volume measurements of discrete samples from Hole 1230A. Additional MAD data, including porosity and grain density, were also calculated from these mass/volume measurements. Wireline bulk density data are available for the interval from 80 to 270 mbsf. The wireline log measurements are generally 0.02–0.08 g/cm³ higher than the discrete sample results across the entire common interval for Hole 1230A (Fig. **F21**). A similar suite of density data are available for Site 685 (Shipboard Scientific Party, 1988).

MST bulk density data for both Holes 1230A and 1230B are noisy over the interval of high core recovery (0–135 mbsf). These data range from 0 g/cm³ (presumably gas voids) to 1.55 g/cm³ with the majority between 1.3 and 1.5 g/cm³ (Fig. **F21A**). The poor quality of the GRA measurements is evident from values <1.2 g/cm³, extreme variability over <1 m, and the –0.15-g/cm³ bias relative to MAD values. We attribute these problems to the effects of depressured core gas expansion, although care was taken to not collect MST data over voids visible through the core liners. A 5-m moving average of the data from Hole 1230A shows variation over the range 1.3–1.45 g/cm³ on a scale of 10 to 15 m (with the average varying little across Subunits IA, IB, IC, and most of ID) (Fig. **F21B**). GRA density data from Site 685 (not shown) reflect the consequences of recording at a 6-mm spacing without regard to the location of voids. They are extremely noisy, variable, and 15%–30% lower than comparable Hole 1230A measurements.

MAD data define downhole trends more clearly than the MST records and are consistent with wireline log results (Fig. **F21B**). Discrete sample bulk density increases slightly with depth from a near-seafloor value of ~1.35 g/cm³ to ~1.55 g/cm³ at the base of Unit I (Fig. **F22A**). An initial steep increase in bulk density (from 1.35 to 1.45 g/cm³) corresponds to a rapid decrease in porosity (from 78% to 70%) across the first 20 mbsf (Fig. **F22C**). From 20 mbsf to the base of Subunit IA (64 mbsf), bulk density remains relatively constant at ~1.45 g/cm³, whereas

F17. Magnetic intensity and susceptibility, p. 65.

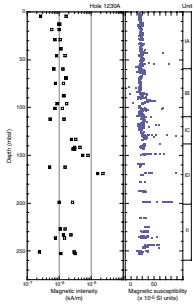

F18. Principal component analysis, 201-1230A-17H-3, 89–91 cm, p. 66.

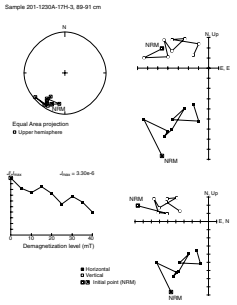

F19. Principal component analysis, 201-1230A-19H-2, 10–12 cm, p. 67.

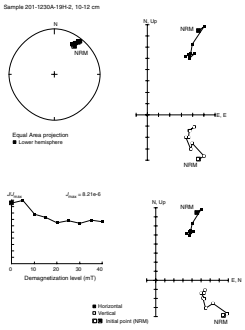

F20. Principal component analysis, 201-1230A-22H-1, 60–62 cm, p. 68.

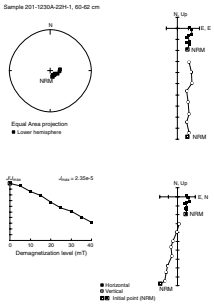

porosity continues to decline slightly to 68%. Grain density is widely variable across the upper 20 m of Hole 1230A and then remains at ~2.44 g/cm³ to the base of Subunit IA (Fig. F22B).

In Subunit IB, MAD-derived bulk density displays three 10-m cycles. Each of these cycles is characterized by a gradual upward decrease from ~1.5 to 1.4 g/cm³ followed by a sharp return to ~1.5 g/cm³ at the top of the cycle. Both the grain density and porosity plots show the same pattern, indicating that the bulk response is dominantly a function of sediment particle type. The wireline bulk density log (Fig. F21B) records the lower two of these cycles and suggests that each cycle consists of thinly interstratified low- and high-porosity bands.

Subunit IC is characterized by a slight downhole decline in bulk density (from ~1.59 to 1.55 g/cm³ in the wireline record) (Fig. F21B). Grain density and porosity data suggest this interval is dissected by a depositional discontinuity at 128 mbsf. The resolution of the density data is not sufficient to allow us to unequivocally interpret this feature. Resistivity data (Fig. F37) suggest that the discontinuity may be linked to a hydrate-bearing zone between 126 and 130 mbsf.

Subunit ID is marked by low core recovery. The MAD-derived bulk density profile follows a smoothed trend of the wireline bulk density log (Fig. F21B). Average bulk density is relatively constant at ~1.46 g/cm³ from 148 to 180 mbsf, increases to 1.61 g/cm³ at 199 mbsf, and then drops to 1.46 g/cm³ at the base of Unit I.

In Unit II, density and porosity measures are widely variable. Average porosity is ~55% and ranges between 40% and 65%. Bulk density ranges between 1.45 and 2.0 g/cm³. Grain density exhibits similar variation between 2.2 and 2.7 g/cm³. Given the close match between the MAD and wireline records where there is sufficient recovery, the data in Unit II indicate interbedded or alternating lithologies with variable physical properties. This is consistent with the lithologic descriptions of ooze with varying clay content, tectonic fabric development, and intermittent carbonate cementation zones (see "Description of Lithostratigraphic Units," p. 8, in "Lithostratigraphy").

The neutron porosity wireline data depict a profile that mimics the MAD-derived porosity measurements, although the wireline data are extremely variable (±15%) and ~15% higher than the MAD-based values (Fig. F26). The cause of this discrepancy is enigmatic. Despite the discrepancy, the wireline data do show, consistent with the MAD measurements, a slightly higher porosity over Subunit ID than would be otherwise expected by simple burial and compaction of a relatively homogeneous sedimentary section.

Compressional Wave Velocity

P-wave data from the MST PWL were recorded at a 10-cm spacing for the first core from Hole 1230A and at 2-cm spacing for Holes 1230D and 1230E. Discrete samples were removed from split cores at a rate of about two per core, depending on lithologic variation and core condition, cut into 1.8- to 3.0-cm³ cubes, and resaturated with seawater for up to 2 days to overcome the loss of interstitial water arising from degassing of the cores. The cubes were oriented so that *P*-wave velocity could be measured using the PWS3 velocimeter in the x-, y-, and z-directions (two horizontal and one vertical plane, respectively, defined with the vertical direction along core axis).

F21. Density measurements, p. 69.

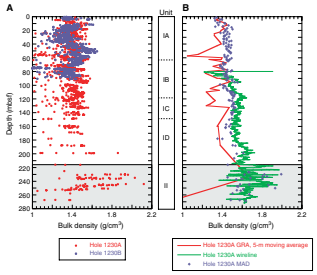

F22. MAD measurements, p. 70.

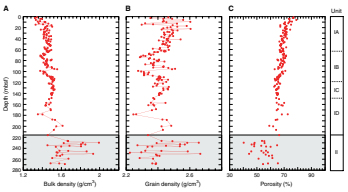

The PWS3 velocimeter data (Fig. F23) show a trend in Unit I consistent with downhole burial compaction observed in the bulk density profile. *P*-wave velocities range from 1500 m/s at the seafloor to ~1600 m/s at the deepest reliable measurement at 170 mbsf. PWL and PWS3 measurements both record the same rapid compaction across the uppermost 10–20 mbsf, as observed in the density data. The PWS3 data yield average velocities ~80–110 m/s slower than those recorded by the sonic wireline log over the common intervals. We attribute this difference to the disruption of sediment fabric caused by gas expansion and the effective pressure difference between in situ and shipboard states. Despite this disruption, the PWS3 data still clearly retain a relict compaction signature.

At the Unit I/II boundary, wireline *P*-wave velocity increases from ~1700 to 1820 m/s over an interval of ~2 m, followed by a sharp peak at 222 mbsf of ~2440 m/s. A carbonate-cemented breccia was recovered from within this 222- to 225-mbsf interval. Below 222 mbsf, the *P*-wave velocity wireline log and the sparse discrete PWS3 data vary over a range of 1560–2150 m/s across the 30-m interval of Unit II. We attribute this variation, similar to that seen in other physical properties, to a heterogeneous distribution of tectonic fabric and degree of cementation.

F23. *P*-wave velocity profiles, p. 71.

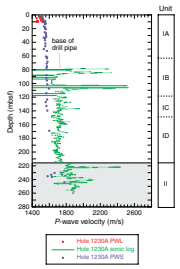

Natural Gamma Ray Emission

NGR was measured on the MST for all Site 1230 holes (spacing = 30 cm, count time = 15 s), except for Hole 1230D, which was run at a higher spatial resolution (spacing = 15 cm, count time = 30 s). In addition, natural gamma radiation was recorded with the NGR sonde on the triple combo tool string during the wireline logging run. MST data sets for Holes 1230A and 1230B are shown with the wireline results in Figure F24. The wireline response is suppressed above ~80 mbsf because of attenuation by the drill pipe.

F24. Natural gamma radiation, p. 72.

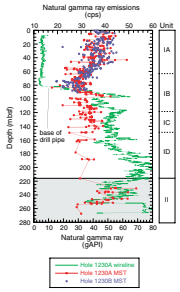

Natural gamma radiation decreases slightly across the upper part of Subunit IA from ~40 counts per second (cps) at the seafloor to ~35 cps at 50 mbsf. Just below 50 mbsf, radiation emissions fall to ~25 cps. This discontinuity does not correlate with features in any other physical property record. A slight offset in NGR at 64 mbsf corresponds to the Subunit IA/IB boundary. The MST NGR record remains relatively constant at ~30 cps until a depth of 82 mbsf, coincident with the depth at which the unattenuated wireline record starts.

Both the MST NGR and the wireline NGR log record low values (<20 cps and ~20 American Petroleum Institute NGR units [gAPI], respectively) at 82 mbsf and then rapidly increasing values to a depth of 96 mbsf. This NGR cycle correlates with a similar rapid downward increase in wireline bulk density (Fig. F21B). The shape of the high-resolution NGR wireline log, in particular, indicates this to be a trend of the type normally associated with upward-coarsening grain size or decreasing clay content. The same trend is recorded by the MST NGR data. From 96 to 118 mbsf, two cycles with similarly upward-decreasing NGR signatures are present. Their responses are not as apparent as in the uppermost cycle, with the lowest values at ~ 40 gAPI units and the high at ~50 gAPI units. Each of these lower two cycles is ~10 m thick and corresponds to similar patterns in the bulk density and resistivity logs. The base of Subunit IB is located at a gamma ray emission peak of 65 gAPI units. A match between the MST and the higher-resolution wireline logs is not clear over this interval.

Across Subunit IC, both the gamma ray wireline log and the MST NGR data are reasonably constant. Values range between 60 and 50 gAPI units, with a slight decline from the top to the base. The noisy but uniform pattern suggests either a thinly bedded or bioturbated, interstratified clay and ooze sequence.

Across the low-recovery interval (Subunit ID), MST NGR data are too sparse to be useful. The wireline log indicates a trend similar to that in Subunit IC for the upper 5 m of Subunit ID. Between 155 and 160 mbsf, emission rates of ~70 gAPI units cap a thick upward-decreasing NGR cycle that extends from 160 to ~202 mbsf. Over this interval, the record increases from 40 to 93 gAPI units. From the base of this cycle to the Unit I/II boundary at 218 mbsf, average NGR declines only slightly from ~78 to 68 gAPI units, with high variability. The actual Unit I/II break in the NGR record is located at 220 mbsf, 2 m below the main break in all other physical property records.

The record from Unit II is characterized by two cycles of upwardly increasing gamma radioactivity. The partial MST NGR record over this interval confirms this pattern. The boundary between the two cycles is at 230 mbsf. The NGR data are not as noisy as the other physical properties over Unit II, and the change at 230 mbsf in the NGR data is not clear in any other property. These cycles probably represent zones of lithologically homogeneous sediment separated by tectonically altered, variably cemented intervals (Shipboard Scientific Party, 1988) (see **"Lithostratigraphy,"** p. 7).

Thermal Conductivity

Thermal conductivity measurements were made on Hole 1230A sediments at a rate of one per core (usually the third section, at 75 cm, if this was available). Values range between 0.68 and 1.07 W/(m·K) (average = 0.83 W/[m·K]) (Fig. **F25A**). Average normalized thermal conductivity and bulk density profiles are correlated (Fig. **F25B**), indicating that the thermal conductivity is generally controlled by water content of the sediments. The consistency and correlation with water content of these measurements is distinctly different from the results reported for Site 685 (Shipboard Scientific Party, 1988; their figure 69). The Site 685 needle probe measurements range over 0.74–0.98 W/(m·K) from 0 to 180 mbsf. At any particular depth, the variation within a 3-m interval is of this same order (0.20 W/[m·K]), clearly indicating ubiquitous measurement error given the homogeneity of sediment type and low porosity variations over the same interval (within 2%). The empirical estimate of thermal conductivity from wireline logs for Site 685 is also suspect, as the method predicts decreasing values across the interface at 216 mbsf between the slope apron and the accretionary wedge.

F25. Thermal conductivity measurements, p. 73.

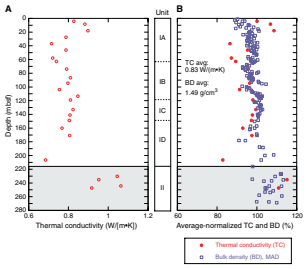

Electrical Properties

We attempted to collect electrical resistance data for calculation of formation factor on cores from Hole 1230A, but degassing of the cores on the catwalk resulted in loss of interstitial water and severe disruption of sediment fabric. Resaturation of cores using surface seawater proved unsuccessful, with measurements of formation factors >3 and some readings up to 8. For comparison, equivalent depth measurements made on diatomaceous ooze at Sites 1227, 1228, and 1229 ranged from 1.7–2.3. Periodic attempts, especially in sediments that appeared con-

solidated, met with similar results. No formation factor results are reported for Site 1230.

The shallow resistivity log was used as a proxy for comparison (Fig. F29D). These data cover the interval from 81 to 275 mbsf (lower 38 m of Subunit IB, Subunits IC and ID, and Unit II) and provide a detailed electrical resistivity record over the gas hydrate zone. As is standard, these logs have not been temperature corrected, but the thermal effect for the 5°C range over the logged interval is calculated at ~0.2 Ωm.

Resistivity increases suddenly at the Unit I/II boundary as a result of the abrupt porosity decrease (65%–44%). A sequence of sharp resistivity modulations is present in Unit II (at 222–225, 231–234, 240–246, and 246–248 mbsf, respectively), with values ranging from 1.0 to 3.5 Ωm. These intervals correlate with positive abrupt bulk density (Fig. F21B) and sonic *P*-wave velocity (Fig. F23) anomalies that, combined with lithostratigraphic indicators, suggest zones of intense cementation and/or tectonic fabric.

Summary and Discussion

Physical property data were derived from MST and discrete sample measurements and two wireline tool (triple combination and FMS-sonic) logging runs. Cores recovered above ~160 mbsf were characterized by high in situ gas content. Rapid depressurization on the catwalk caused considerable disturbance to sediment fabric. This disturbance inhibited *P*-wave velocity measurements, eliminated formation factor determination, and biased MAD-based bulk density by –0.02 to –0.08 g/cm^3 relative to in situ wireline estimates. Wireline- and laboratory-based physical property profiles, with the exception of the porosity data, are nonetheless in agreement where core recovery allowed for continuous shipboard measurements. The porosity discrepancy between the discrete property and logging data (~15%) has not been satisfactorily resolved, but several possible explanations exist. For instance, incomplete drying of closed diatom frustules could result in a low discrete porosity estimate relative to the wireline log. Equally, degassing of sediments could widen the gap between porosity measurements made in the laboratory and those made in the borehole because of the different properties used by each to calculate porosity. In overpressured sediments exposed in the borehole, free gas escapes from the formation to be substituted by water, whereas in the extracted sediments the same process in air results in dewatering of the sediments. Wireline porosity values >100%, however, suggest a systematic bias in the neutron sonde processing.

The stratigraphic section is composed of two units divided by a sharp physical property boundary at 216 mbsf. The principal consolidation process in Unit I is consistent with burial compaction as shown by the bulk density/porosity and *P*-wave velocity profiles. Wireline resistivity and *P*-wave velocity anomalies, coupled with catwalk IR thermal imaging analysis and direct observations, support prediction of several in situ gas hydrate zones in Subunits IB and IC (see "Gas Hydrate," p. 35). Unit II physical properties reflect distinct consolidation-related modifications, most clearly shown as carbonate cementation and strain fabric development. Such lithologic modification is characteristic of convergent margin wedge sediments.

DOWNHOLE TOOLS

At Site 1230, the downhole tools employed were the Adara temperature shoe, DVTP, DVTP-P, WSTP, and PCS. The results of the temperature and pressure measurements at Site 1230 are described in the two sections below. A sample of bottom water was successfully collected with the WSTP from 10 to 20 m above the seafloor at the site of Hole 1230A. Chlorinity data showed that this sample deviated <7% from IAPSO standard seawater (see **"Interstitial Water,"** p. 12, in "Biogeochemistry").

Abundant gas voids in sediment indicated that significant loss of methane occurred during core recovery at Site 685 (Shipboard Scientific Party, 1988). Because methane comprises an important product and reactant in biogeochemical reactions, the PCS was deployed 10 times at Site 1230 to retain methane otherwise expected to vent during the wireline trip. The ultimate scientific objective of this exercise is the post-cruise construction of an in situ methane concentration profile (see, e.g., Dickens et al., 1997). Initial results of PCS deployments at Site 1230 are presented in **Dickens et al.** (this volume).

In Situ Temperature Measurements

Three downhole temperature determinations were made at Site 1230 using two DVTP deployments in Hole 1230A and one in Hole 1230B. Two Adara temperature shoe deployments at the seafloor yielded values for the bottom-water temperature of 1.74°–1.75°C. The WSTP deployment successfully recorded a value of 1.9°C for water temperature 10–20 m above the seafloor. Figure **F26** shows the data from the successful DVTP deployments at 33.3, 100, and 254.6 mbsf. Three other deployments at 73.5, 79.9, and 148.3 mbsf resulted in records that could not be used. Table **T12** summarizes all of the Site 1230 temperature measurements.

The results of the DVTP and Adara temperature measurements are displayed in Figure **F27.** The combined downhole temperatures yield a linear gradient of 0.0343°C/m in the upper 255 m of the sediment column (Fig. **F27**). The extrapolated temperature at the bottom of Hole 1230A, at 277.3 mbsf, is 11.2°C. Multiplying the gradient by an average thermal conductivity of 0.83 W/(m·K) (Fig. **F25**) gives a conductive heat flow estimate of 28 mW/m² at Site 1230. This heat flow estimate is identical to the value estimated for Site 685 by the Leg 112 Shipboard Scientific Party (1988). Figure **F27B** shows the temperature data with a theoretical steady-state conductive temperature profile calculated using a constant heat flow of 28 mW/m², a seafloor temperature of 1.74°C, and the measured thermal conductivities from the Hole 1230A cores. To illustrate that the steady-state conductive profile cannot match the curvature of the temperature data, a best-fit parabola is also shown. Preliminary calculations indicate that the curvature in the downhole temperature profile can be explained by upward fluid flow of 1–10 mm/yr (Fig. **F27C**). This rate is comparable to model estimates for flow rates in the Peru accretionary prism (Kukowski and Pecher, 1999). On the basis of the DIC profile, an upper bound on the flow rate is ~1 mm/yr (see **"Biogeochemistry,"** p. 12).

The failure rate for DVTP measurements attributed to formation conditions at Site 1230 was 50%, compared to 80% at Site 1229, 50% at Sites 1227 and 1228, and 0% at Sites 1225 and 1226. To understand the

F26. DVTP temperature records, p. 74.

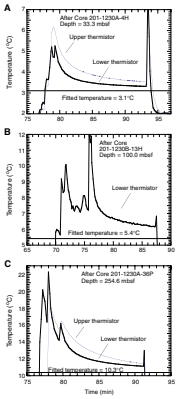

T12. Downhole temperatures, p. 104.

F27. Temperatures vs. depth, p. 75.

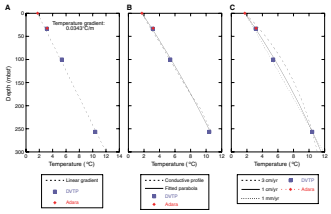

causes of the failures, the conditions of the formation at each location were evaluated by noting the recovery, lithology, and disturbance of the subsequent core (Table T12). The differences in outcome do not appear to be related to either lithology or core recovery. Instead, the degree of disturbance in the subsequent core may be significant. Although the cause of core disturbance on recovery is not known, areas of multiple fractures, voids, and crumbly fabric were common in the intervals with high methane concentrations and gas hydrates (see Fig. F34, and "Gas Hydrate," p. 35). Moreover, the three failed deployments were located at 70–80 and 148–150 mbsf, where the interstitial water lithium concentrations indicate the highest hydrate concentrations (see "Interstitial Water," p. 12, in "Biogeochemistry"). On the basis of these observations, the best strategy for obtaining high-quality temperature data in hydrate-bearing formations may be to identify depths of highest hydrate concentrations in the first hole and avoid these depths by deploying the tool in subsequent holes.

Davis-Villinger Temperature-Pressure Probe

The DVTP-P was deployed twice at Site 1230 with one successful run at a depth of 102.5 mbsf (after Core 201-1230A-14H) (Fig. F28). The results of this deployment indicate overpressure in the formation relative to the base of the hole. This deployment did not detect a pressure spike at the start because the tool was pushed in extremely slowly over several minutes. The slow deployment strategy was used to increase the penetration depth of the tool without exceeding acceptable pressure on bit in the relatively stiff formation. The success of this strategy is evident from the 0.14-MPa difference between formation pressure and the hydrostatic pressure measured in the base of the hole for 5 min at the end of the deployment. For a reasonable formation permeability of ~10^{-16} m^2, the measured overpressure is adequate to produce flow at a rate of ~5 mm/yr.

F28. DVTP-P pressure, p. 76.

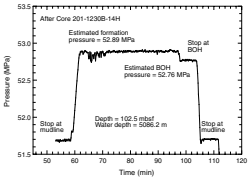

APC-Methane Tool

The APC-M tool was deployed in Hole 1230B continuously from Cores 201-1230B-3H through 13H. The recovered data from this run showed that the tool and data logger initially functioned correctly. Data from the APC-M tool will be analyzed postcruise.

DOWNHOLE LOGGING

Operations

Two logging runs were made in Hole 1230A with the triple combo and the FMS-sonic tool strings (see "Downhole Logging," p. 53, in the "Explanatory Notes" chapter). The FMS-sonic run was added to the program at this site in order to better characterize the gas hydrate deposit that had been detected at Site 685 during Leg 112 (Shipboard Scientific Party, 1988) (see "Gas Hydrate," p. 35). After recovery of Core 201-1230A-39P at 2300 hr on 15 March, the hole was conditioned for logging. The wiper trip indicated that there was no fill at the bottom of the hole. The hole was then displaced with 150 bbl of sepiolite, and the bottom of the drill string was positioned at 80 mbsf. Logging rig-up started at 0300 hr on 16 March. The 35-m-long triple combo tool string

started downhole at 0530 hr, and two passes were made without difficulty. Both passes reached the bottom of the hole at the wireline depth of 282 mbsf, and the triple combo run was completed at 1400 hr. The 33-m-long FMS-sonic tool string started downhole at 1515 hr, and two passes were made without problem over the entire open hole. Because of some concern over a tight spot felt at every exit of the bit, the drill string was raised by 10 m only during the last pass, allowing data recording in the open hole to 70 mbsf. Logging operations and rig-down were completed by 2200 hr on March 16 (see Table T13 for a detailed summary of the operations).

T13. Detail of logging operations, Hole 1230A, p. 105.

Data Quality

The caliper log measured by the two arms of the FMS (Fig. F29A) shows that the borehole wall was irregular but generally smooth and that the caliper arms maintained a good contact with the formation over most of the interval logged. This suggests that the data should be of excellent quality. There is a good correlation between the density log and the density measurements made on core samples (Fig. F29F). However, the good borehole conditions make it difficult to explain the discrepancy between the porosity log and the core measurements in Figure F29G. The logging values are consistently ~20% higher than the core measurements. The presence of bound water with clays generally increases the porosity measured with the Accelerator Porosity Sonde (see "Downhole Logging," p. 53, in the "Explanatory Notes" chapter), but there was no similar discrepancy in the previous Peru margin sites (Sites 1228 and 1229), where the clay content was generally higher than at this site. Because the dominant component of these sediments is diatom ooze (see "Lithostratigraphy," p. 7), the core measurements might be underestimating the voids in the diatom skeletons, which are sensed by the porosity log. However, this should not account for the extent of the difference between the core and log measurements. We used the grain density measured on core samples (see "Density and Porosity," p. 26, in "Physical Properties") to derive a porosity curve from the density log, by interpolating the grain density measurements at the logging sampling interval (0.1524 m) and assuming a uniform water density of 1.05 g/cm³. The resulting profile (red line in Fig. F29G) is in much better agreement with core measurements. This agreement is a direct consequence of the good match between the log and core density data because the same grain density is used to derive the core sample porosity from the core density measurements.

The sonic compressional and shear velocities in Figure F29E were calculated during the acquisition by an automatic slowness-time coherence algorithm applied to the monopole and dipole waveforms (see "Downhole Logging," p. 53, in the "Explanatory Notes" chapter). The gaps and some dubious spikes in this figure show that the waveforms will need to be reprocessed, particularly in the upper part of the hole, in order to determine more reliable values.

F29. Main logs recorded, Hole 1230A, p. 77.

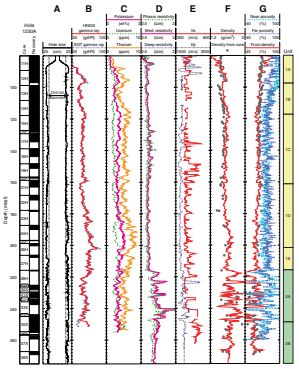

Logging Stratigraphy

The general trend of the logs is controlled by the nature of the sediments and influenced by the location of the site on the lower slope of the Peru Trench, at the transition between the continental crust and the accretionary complex. The sediment composition, as shown by the average gamma radiation values, is intermediate between the equatorial

Pacific sites (Sites 1225 and 1226), which were dominated by biogenic sediments with extremely low gamma radiation counts, and the shallow margin sites (Sites 1228 and 1229), which contained mostly terrigenous sediments. Thorium concentrations consistently higher than uranium suggest that the clastic sediments are of continental origin (Rider, 1996). However, the low variability in most logs is similar to the data recorded in the open-ocean sites. Because of this low variability in the logs, we distinguish only two logging units, which correspond to the two lithostratigraphic units identified from the cores (see **"Description of Lithostratigraphic Units,"** p. 8, in "Lithostratigraphy").

Logging Unit 1 (80–216 mbsf) is characterized by a general downhole increase in natural gamma radiation, thorium, resistivity, and density. This general trend corresponds to sediment compaction. This logging unit can be divided into five subunits with slightly different characteristics.

Logging Subunit 1A (80–97 mbsf) is characterized by very high porosity and a strong downhole increase in gamma radiation and density. Spikes in the resistivity log and, less reliably, in the velocity log could indicate the presence of gas hydrate that was recovered in this unit (Core 201-1230B-12H) (see **"Lithostratigraphy,"** p. 7). A highly resistive feature that steeply dips to the north in the FMS images at 85 mbsf (Fig. **F30A**) could represent a hydrate-rich layer.

The top of logging Subunit 1B (97–118 mbsf) is marked by a sharp drop in density, resistivity, gamma radiation, and thorium followed by a steady downhole increase in these same measurements. The overall lower thorium content of this unit indicates a more marine origin of the sediments.

Logging Subunit 1C (118–160 mbsf) shows almost uniform values in gamma radiation, radioactive element concentration, and density, as well as some variability in resistivity that could be attributed to the presence of gas hydrate. Gas hydrate was identified in three cores from this subunit during Leg 201 (Cores 201-1230A-15H, 18H, and 19H) (see **"Lithostratigraphy,"** p. 7) and during Leg 112 (Shipboard Scientific Party, 1988). The FMS images in this subunit (Fig. **F30B, F30C**) show a series of resistive features that generally dip to the north, northeast, or to the southwest. These features indicate tilted layers, faulting, and conjugate planes, particularly between 135 and 140 mbsf and between 145 and 155 mbsf. Gas hydrate might be filling some of these fault joints.

Logging Subunit 1D (160–201 mbsf) is characterized by a steady increase in density and gamma radiation, mostly due to an increase in thorium. The top of logging Subunit 1E (201–216 mbsf) is marked by a sharp drop in gamma radiation, and this subunit is characterized by a decrease in gamma radiation and density, opposite to the compacting trend of the overlying subunits.

Logging Unit 2 (216–280 mbsf) corresponds to lithostratigraphic Unit II (see **"Description of Lithostratigraphic Units,"** p. 8, in "Lithostratigraphy") and is composed of sediments under intense deformation belonging to the accreted complex. The top of this unit is marked by a sharp increase in resistivity and density. It is also clearly defined in the FMS images (Fig. **F30D**) by a bright massive feature that dips ~69° to the northeast at 216 mbsf. All static images from below this depth (Fig. **F30D, F30E**) are much brighter than those from above this boundary. This relative brightness indicates the higher resistivity of the accreted sediments. Some of the most striking features in the images (at 223, 225, and 241 mbsf) are steeply dipping to the northeast (by 55°–70°). This inclination indicates the general deformation of the accreted sedi-

F30. FMS images, p. 78.

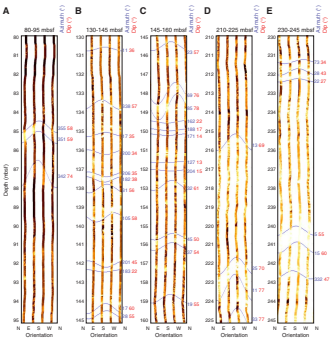

ments. Whereas logging Subunit 2A (216–246 mbsf) shows a very high variability in resistivity and density, the underlying logging Subunit 2B (246–280 mbsf) is characterized by almost uniform, slightly lower, resistivity and density.

Temperature Log

Temperatures were recorded with the Lamont-Doherty Earth Observatory Temperature/Acceleration/Pressure (TAP) memory tool attached at the bottom of the triple combo tool string. Because only a few hours had passed since the end of drilling operations and hole conditioning, the borehole temperature is not representative of the actual equilibrium temperature distribution of the formation. In the case of Hole 1230A, the surface seawater cooled though the 5-km water column generated borehole fluid temperatures lower than the equilibrium formation temperatures. Discrete measurements made with the DVTP indicate a maximum measured temperature of 10.34°C at 256.6 mbsf (see **"In Situ Temperature Measurements,"** p. 31, in "Downhole Tools"), whereas the maximum temperature recorded by the TAP tool at 284 mbsf is 8.9°C (see Fig. **F31**). The generally higher temperatures during the second pass indicate a progressive return to equilibrium. The variations measured at 80 mbsf while logging downhole correspond to the tool exiting the drill string. The temperature fluctuations within the pipe recorded during the two passes logging downhole are difficult to explain. Overall, this profile suggests that besides mechanical drilling disturbances, the operations in Hole 1230A did not raise temperatures and cause decomposition of gas hydrate, which remains stable to temperatures of up to 30°C at this depth (Kvenvolden and McMenamin, 1980). Therefore, the present data should allow an accurate estimation of the hydrate content of these sediments.

F31. Hole 1230A temperature log, p. 79.

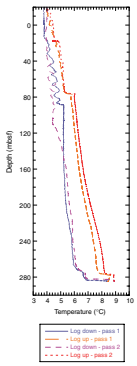

GAS HYDRATE

Solid pieces of gas hydrate were recovered from ~82 and ~148 mbsf at Site 1230. Indirect evidence for gas hydrate also exists in several cores below 70 mbsf. Collectively, physical and chemical data suggest that small quantities of gas hydrate are present, at least intermittently, from ~70 mbsf to the base of the recovered interval at 278.3 mbsf.

Initial Core Inspection and Hydrate Sampling

The dissociation of gas hydrate is an endothermic reaction that produces gas and decreases the temperature of surrounding sediment (Sloan, 1990). All cores from Site 1230 were inspected immediately after retrieval for indications of gas hydrate, including white nodules, fizzing, or unusually cold spots. As soon as the core liner had been placed on the catwalk, the IR camera was run along the core to identify unusually cold core liner temperatures. Intervals that potentially contained gas hydrate were immediately cut out of the core and split. The split core surfaces were then inspected for hydrate or fizzing.

Small pieces of dirty white gas hydrate were recovered from sediments of lithostratigraphic Subunit IB at ~82 mbsf in Core 201-1230B-12H and the top of Subunit ID at ~148 mbsf in Core 201-1230A-19H. A 5-cm^3 piece of hydrate from Core 201-1230B-12H was scraped with a spatula to remove surrounding sediment and placed into a syringe to

collect gas and water for geochemical analyses. The remaining scraped sediment was then collected for microbiological analyses. One fizzing and anomalously cold 15-cm whole-round section (Sample 201-1230A-19H-1, 135–150 cm) was squeezed for interstitial water. At least three other sections contained disseminated gas hydrate based on observed fizzing and low temperatures (see Table T14), although discrete hydrate pieces were not recovered. Table T14 summarizes the six sections with cold spots and observed hydrate or fizzing sediment.

T14. Observations and evidence of gas hydrate, p. 106.

Infrared Camera

IR thermal imaging was useful for identifying zones of potential gas hydrate in sediment cores immediately after retrieval at Site 1230 (Fig. F32). For example, temperature varied <1°C down Core 201-1230A-6H. This core displayed no IR evidence for hydrate. In contrast, temperature changes by nearly 8°C down Core 201-1230A-19H. These intervals are anomalously cold compared with surrounding sediment and voids, the latter being anomalously warm (Fig. F30B). This core contained definite gas hydrate at 148.3 mbsf and likely at ~149.7 mbsf (Table T14). Several other cores exhibited temperature excursions of about –5°C, indicating that they may have contained hydrate. The shallowest of these significant temperature anomalies was present at ~71 mbsf in Core 201-1230A-10H (Fig. F14).

F32. IR temperature comparisons, p. 80.

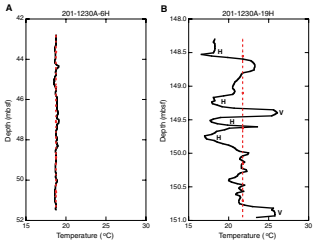

Lithology and Gas Hydrate Occurrence

Cores 201-1230B-11H and 12H (73.5–90.5 mbsf) that surround and contain the upper interval with hydrate samples, consist of dark gray to olive clay-bearing diatom silt and diatom-rich nannofossil silt. High-angle normal faults with offsets of several centimeters are present in Sections 201-1230B-11H-4, 11H-5, and 12H-6. The sediments are characterized by pervasive cleavage with both low-angle and horizontal attitude. The recovered hydrate sample from Core 201-1230B-12H consisted of several vertical to subvertical wavy veins of white gas hydrate, up to 3 mm thick, separated by dark gray sediment (Fig. F33). Cores 201-1230A-18H and 19H (138.8–156.8 mbsf) that surround and contain the lower interval of hydrates consist of dark gray to black quartz-bearing clay-rich diatom ooze. The sediments have a stiff and highly fractured appearance, and recovery was generally low throughout the subunit, possibly due to a combination of fracturing and high gas concentrations (see "Biogeochemistry," p. 12). Horizontal to low-angle foliation is common in most cores of Subunit ID. In addition, Section 201-1230A-19H-2 was characterized by a ~30° cleavage direction. The co-occurrence of steeply dipping gas hydrate veins, pervasive cleavage, and high-angle normal faults, at least in the upper part of the hydrate-bearing interval, suggests structural control on gas hydrate precipitation at Site 1230. Gas hydrate distribution at other locations appears to be structurally controlled because faults and fractures can provide conduits for transporting methane (e.g., Ginsburg and Solovieu, 1977; Wood and Ruppel, 2000).

F33. Gas hydrate filling fractures, p. 81.

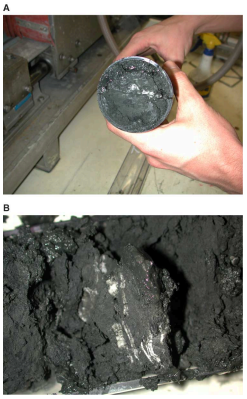

Core Disturbance

Sediment cores recovered from sequences containing gas hydrate are typically disturbed (Paul, Matsumoto, and Wallace, et al., 1996; Westbrook et al., 1994). Extensive core disturbance was noted in most of the

cores below Core 201-1230A-3H. The following types of disturbance, ranging from a few centimeters to tens of centimeters in vertical extent, were observed:

1. Voids marked by clear separation of sediment and bounded on either side by disturbances of either type 2 or 3 below (Fig. F34A, F34B). In this category we specifically did not consider voids where the separation was bounded by planar surfaces without other disturbance because these can (and were observed to) form on the catwalk when the core liners were drilled to relieve pressure for safety reasons.
2. Crumbling of the sediment: zones where the sediments are wholly or partially disaggregated adjacent to undisturbed sediment. For this category, we did not consider any core disturbance that was located at the top of a core (Fig. F34C).
3. Zones of splitting perpendicular to the core axis (i.e., parallel to bedding) where cracks are commonly more closely spaced than elsewhere in the core (Fig. F34D). In many cases there is a gradation from very closely spaced cracks near the center of the zone to more widely spaced cracks.

The depth interval and types of sediment disturbance are similar to those found during Leg 112 at Site 685 (Suess, von Huene, et al., 1988). This disturbance alone does not indicate the presence of hydrate. However, it does suggest depth intervals where methane concentrations are sufficiently high that gas rapidly escapes from sediment during core recovery. Such concentrations are necessary to form gas hydrate.

F34. Methane expansion and gas hydrates, p. 82.

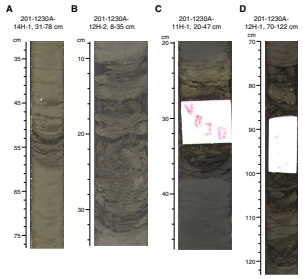

Interstitial Water Chemistry

High-resolution profiles of interstitial water chemistry, particularly of conservative solutes such as chloride, can be used to quantify the amount and distribution of gas hydrate in drill holes (e.g., Hesse et al., 1985; Egeberg and Dickens, 1999). Gas hydrate formation excludes dissolved ions, which, over time, advect or diffuse away from zones of gas hydrate. During core recovery and processing, gas hydrates can rapidly dissociate, releasing their freshwater into the pore space. Consequently, deviations in interstitial water composition toward freshwater can signify dilution by dissociated gas hydrate.

Freshening occurs throughout the cored sediment column below ~20 mbsf at Site 1230 (Fig. F35). As observed in the high-resolution dissolved lithium profile (Fig. F3), it is most extreme in two zones centered at ~80 and ~150 mbsf. The hydrate sample from Core 201-1230B-12H (~80 mbsf) was analyzed for dissolved barium, chloride, iron, lithium, manganese, strontium, acetate, and formate. Although the sample has measurable quantities of all these species (Table T15), the water is much fresher than surrounding interstitial water. It is also fresher than most previous water samples collected from dissociated gas hydrate specimens in deep boreholes (e.g., Kvenvolden and McDonald, 1985; Paull, Matsumoto, Wallace, et al., 1996). The sample is probably contaminated by ~3% interstitial water, based on its ionic content, although the lattice water may contain trace amounts of dissolved species.

An interval fizzing on the catwalk and suspected of containing gas hydrate (Sample 201-1230A-19H-1, 135–150 cm; 149.65 mbsf) was collected and processed as an IW sample. This sample had concentrations of dissolved species significantly below those found in IW samples with

F35. IW chloride concentrations, p. 83.

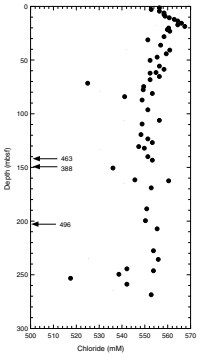

T15. Chemical species in gas hydrate, p. 107.

minimal or no evidence for hydrate (Table T15). In order to account for the low chloride and lithium concentrations of this sample relative to the general interstitial water profiles of these elements (Fig. F3) (see "Interstitial Water," p. 12, in "Biogeochemistry"), the pore space must have contained ~20% hydrate.

The abundance of gas hydrate in sediment can be determined from the in situ gas concentrations (i.e. the concentrations before degassing during conventional core recovery [Dickens et al., 1997]). The PCS was deployed 10 times at Site 1230 between 22 and 277 mbsf in order to construct an in situ gas concentration profile (see Dickens et al., this volume). Preliminary estimates suggest that in situ methane concentration at Site 1230 range from 13 mM (Core 201-1230B-4P) to 400 mM (Core 201-1230A-20P). The latter value greatly exceeds methane solubility with respect to the dissolved methane-methane-hydrate partial saturation curve (Handa, 1990). It is consistent with the presence of several percent gas hydrate in pore space of sediment at ~150 mbsf.

Physical Properties and Wireline Logging

Site 1230 provided an opportunity to examine the links between hydrate presence and physical properties in downhole logs. Wireline logging measurements most sensitive to hydrate presence are resistivity and sonic velocity. Resistivity increases because of the insulating properties of ice and because of the drilling-induced freshening of interstitial water. Sonic velocity increases because of the solidifying effect of solid ice in the pore space (Collett, 1998). The presence of hydrate has been shown to increase sonic attenuation and decrease the amplitude of sonic logging waveforms (Guerin et al., 1999). These features are visible in the logging data from Site 1230, and there are four broad intervals where logging data may indicate the presence of gas hydrate in Hole 1230A (Fig. F36). The extent of these intervals is mostly defined by areas where dipole waveforms, and to a lesser extent monopole waveforms, have lower amplitudes. Guerin et al. (1999) observed that at low hydrate concentration, dipole waveforms are more sensitive to the presence of hydrate, which could explain the stronger amplitude contrasts in the dipole waveforms in Hole 1230A. The FMS images indicate fine features, such as those shown in Figure F30B and F30C. This suggests that any hydrate in these intervals is likely disseminated rather than in massive accumulations. The density log helps distinguish intervals where increased resistivity cannot be attributed to hydrate because hydrate has a slightly lower density than water. Resistivity highs between 216 and 220 and between 224 and 232 mbsf are probably not caused by hydrate but rather by cemented layers because they are associated with increases in density. In comparison, resistivity highs at 128, 140, and 241 mbsf could indicate gas hydrate (Fig. F36). Because of limitations imposed by the resolution of the wireline logs (see "Downhole Logging," p. 53, in the "Explanatory Notes" chapter) and depth matching between separate log runs, reprocessing of sonic data will be required to confidently correlate individual peaks in resistivity and sonic velocity.

F36. Logging data evidence of gas hydrates, p. 84.

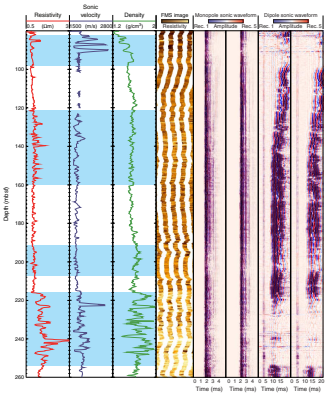

Summary

Previous work at Site 685 suggested that gas hydrates were present below 40 mbsf but were concentrated in two intervals at ~107 and ~165 mbsf (Suess, von Huene, et al., 1988). Information collected at Site 1230 supplements these findings. Two intervals of concentrated gas hydrate

were found at Site 1230, but they are offset from those of Site 685 by ~20 m. One of the gas hydrate pieces recovered at Site 1230 was composed of several-millimeter-thick layers oriented at a high angle to bedding surfaces. We suspect that this gas hydrate was associated with a fault plane because small high-angle faults were common at Site 1230 and because previous work on hydrates in other regions has shown a link between faults and gas hydrate presence (Ginsburg and Solovieu, 1997; Wood and Ruppel, 2000). The depth offset between zones of concentrated hydrate may reflect preferential emplacement of hydrate along high-angle faults.

At other ODP sites where gas hydrate is present, much of the hydrate is inferred to be disseminated in pore space and most does not survive the wireline trip (e.g., the Blake Ridge, Paull, Matsumoto, Wallace, et al., 1996). This may also be the case at Site 1230. In addition to the zones of concentrated hydrate, temperature observations, core disturbance, interstitial water chloride concentrations, and velocity and electrical resistivity log data suggest that small amounts of disseminated gas hydrate may be present throughout the recovered sedimentary section at Site 1230, starting below ~70 mbsf or even shallower (Fig. **F37**).

F37. Comparison of depths with gas hydrates, p. 85.

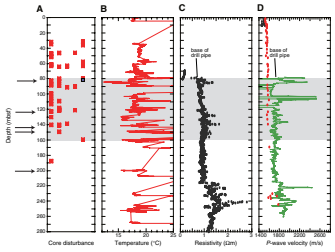

REFERENCES

Borowski, W.S., Hoehler, T.M., Alperin, M.J., Rodriguez, N.M., and Paull, C.K., 2000. Significance of anaerobic methane oxidation in methane-rich sediments overlying the Blake Ridge gas hydrates. *In* Paull, C.K., Matsumoto, R., Wallace, P.J., and Dillon, W.P. (Eds.), *Proc. ODP, Sci. Results,* 164: College Station, TX (Ocean Drilling Program), 87–99.

Borowski, W.S., Paull, C.K., and Ussler, W., III, 1996. Marine pore-water sulfate profiles indicate in situ methane flux from underlying gas hydrate. *Geology,* 24:655–658.

————, 1999. Global and local variations of interstitial sulfate gradients in deep-water, continental margin sediments: sensitivity to underlying methane and gas hydrates. *Mar. Geol.,* 159:131–154.

Brumsack, H.-J., 1986. The inorganic geochemistry of Cretaceous black shales (DSDP Leg 41) in comparison to modern upwelling sediments from the Gulf of California. *In* Summerhayes, C.P., and Shackleton, N.J. (Eds.), *North Atlantic Palaeoceanography.* Spec. Publ.—Geol. Soc. London, 21:447–462.

Collett, T.S., 1998. Well log evaluation of gas hydrate saturations. *Trans. Soc. Prof. Well Log Analysts, Thirty-Ninth Ann. Logging Symp.,* Keystone, Colorado, Pap. MM.

Davie, M.K., and Buffett, B.A., 2001. A numerical model for the formation of gas hydrate below the seafloor. *J. Geophysical Res.,* 106:497–514.

Dickens, G.R., 2001. Sulfate profiles and barium fronts in sediment on the Blake Ridge: present and past methane fluxes through a large gas hydrate reservoir: *Geochim. Cosmochim. Acta,* 65:529–543.

Dickens, G.R., Paull, C.K., Wallace, P., and the ODP Leg 164 Scientific Party, 1997. Direct measurement of in situ methane quantities in a large gas-hydrate reservoir. *Nature,* 385:427–428.

Dickens, G.R., Wallace, P.J., Paull, C.K., and Borowski, W.S., 2000. Detection of methane gas hydrate in the pressure core sampler (PCS): volume-pressure-time relations during controlled degassing experiments. *In* Paull, C.K., Matsumoto, R., Wallace, P.J., and Dillon, W.P. (Eds.), *Proc. ODP, Sci. Results,* 164: College Station, TX (Ocean Drilling Program), 113–126.

Egeberg, P.K., and Dickens, G.R., 1999. Thermodynamic and pore water halogen constraints on gas hydrate distribution at ODP Site 997 (Blake Ridge). *Chem. Geol.,* 153:53–79.

Fossing, H., Ferdelman, T.G., and Berg, P., 2000. Sulfate reduction and methane oxidation in continental margin sediments influenced by irrigation (South-East Atlantic off Namibia). *Geochim. Cosmochim. Acta,* 64:897–910.

Ginsburg, G.D., Solovieu, V.A., 1997. Methane migration within the submarine gas-hydrate stability zone under deep water conditions. *Mar. Geol.,* 137:49–57.

Guerin, G., Goldberg, D., and Meltser, A., 1999. Characterization of in situ elastic properties of gas-hydrate bearing sediments on the Blake Ridge. *J. Geophys. Res.,* 104:17781–17795.

Hagelberg, T.K., Shackleton, N., Pisias, N., and Shipboard Scientific Party, 1992. Development of composite depth sections for Sites 844 through 854. *In* Mayer L., Pisias, N., Janecek, T., et al., *Proc. ODP, Init. Repts.,* 138 (Pt. 1): College Station, TX (Ocean Drilling Program), 79–85.

Handa, Y.P., 1990. Effect of hydrostatic pressure and salinity on the stability of gas hydrates. *J. Phys. Chem.,* 94:2652–2657.

Hesse, R., Lebel, J., and Gieskes, J.M., 1985. Interstitial water chemistry of gas-hydrate-bearing sections on the Middle America Trench slope, Deep-Sea Drilling Project Leg 84. *In* von Huene, R., Aubouin, J., et al., *Init. Repts. DSDP,* 84: Washington (U.S. Govt. Printing Office), 727–737.

Hoehler, T.M., Borowski, W.S., Alperin, M.J., Rodriguez, N.M., and Paull, C.K., 2000. Model, stable isotope, and radiotracer characterization of anaerobic methane oxi-

dation in gas hydrate–bearing sediments of the Blake Ridge. *In* Paull, C.K., Matsumoto, R., Wallace, P.J., and Dillon, W.P. (Eds.), *Proc. ODP, Sci. Results,* 164: College Station, TX (Ocean Drilling Program), 79–85.

Iversen, N., and Jørgensen, B.B., 1985. Anaerobic methane oxidation rates at the sulfate–methane transition in marine sediments from Kattegat and Skagerrak (Denmark). *Limnol. Oceanogr.,* 30:944–955.

Kasten, S., Haese, R.R., Zabel, M., Ruhlemann, C., and Schulz, H.D., 2001. Barium peaks at glacial terminations in sediments of the equatorial Atlantic Ocean—relicts of deglacial productivity pulses? *Chem. Geol.,* 175:635–651.

Kastner, M., Elderfield, H., Martin, J.B., Suess, E., Kvenvolden, K.A., and Garrison, R.E., 1990. Diagenesis and interstitial-water chemistry at the Peruvian continental margin—major constituents and strontium isotopes. *In* Suess, E., von Huene, R., et al., *Proc. ODP, Sci. Results,* 112: College Station, TX (Ocean Drilling Program), 413–440.

Kukowski, N., and Pecher, I., 1999. Thermo-hydraulics of the Peruvian accretionary complex at 12°S. *Geodynamics,* 27:373–402.

Kvenvolden, K.A., Frank, T.J., and Golan-Bac, M., 1990. Hydrocarbon gases in Tertiary and Quaternary sediments offshore Peru—results and comparisons. *In* Suess, E., von Huene, R., et al., *Proc. ODP, Sci. Results,* 112: College Station, TX (Ocean Drilling Program), 505–515.

Kvenvolden, K.A., and Kastner, M., 1990. Gas hydrates of the Peruvian outer continental margin. *In* Suess, E., von Huene, R., et al., *Proc. ODP, Sci. Results,* 112: College Station, TX (Ocean Drilling Program), 517–526.

Kvenvolden, K.A., and McDonald, T.J., 1985. Gas hydrates of the Middle America Trench—Deep Sea Drilling Project Leg 184. *Init. Repts. DSDP,* 184: Washington (U.S. Govt. Printing Office), 677–682.

Kvenvolden, K.A., and McMenamin, M.A., 1980. Hydrates of natural gas: a review of their geologic occurrence. *Geol. Surv. Circ. (U.S.),* 825.

Martin, J.B., Gieskes, J.M., Torres, M., and Kastner, M., 1993. Bromide and iodine in Peru margin sediments and pore fluids: implication for fluid origins. *Geochim. Cosmochim. Acta,* 57:4377–4389.

Monnin, C., 1999. A thermodynamic model for the solubility of barite and celestite in electrolyte solutions and seawater to 200°C and to 1 kbar. *Chem. Geol.,* 153:187–209.

Niewöhner, C., Hensen, C., Kasten, S., Zabel, M., and Schultz, H.D., 1998. Deep sulfate reduction completely mediated by anaerobic methane oxidation in sediments of the upwelling area off Namibia. *Geochim. Cosmochim. Acta,* 62:455–464.

Parkes, R.J., Cragg, B.A., Bale, S.J., Getliff, J.M., Goodman, K., Rochelle, P.A., Fry, J.C., Weightman, A.J., and Harvey, S.M., 1994. A deep bacterial biosphere in Pacific Ocean sediments. *Nature,* 371:410–413.

Paull, C.K., Matsumoto, R., Wallace, P.J., et al., 1996. *Proc. ODP, Init. Repts.,* 164: College Station, TX (Ocean Drilling Program).

Rider, M., 1996. *The Geological Interpretation of Well Logs* (2nd ed.): Houston (Gulf Publishing Co.).

Shipboard Scientific Party, 1988. Site 685. *In* Suess, E., von Huene, R., et al., *Proc. ODP, Init. Repts.,* 112: College Station, TX (Ocean Drilling Program), 597–704.

Sloan, E.D., 1990. *Clathrate Hydrates of Natural Gases:* New York (Marcel Dekker).

Smith, D.C., Spivack, A.J., Fisk, M.R., Haveman, S.A., Staudigel, H., and ODP Leg 185 Shipboard Scientific Party, 2000. Methods for quantifying potential microbial contamination during deep ocean coring. *ODP Tech. Note,* 28 [Online]. Available from the World Wide Web: <http://www-odp.tamu.edu/publications/tnotes/tn28/INDEX.HTM>. [2002-03-30]

Suess, E., von Huene, R., et al., 1988. *Proc. ODP, Init. Repts.,* 112: College Station, TX (Ocean Drilling Program).

Tissot, B.P., and Welte, D.H., 1984. *Petroleum Formation and Occurrence:* Berlin (Springer-Verlag).

Torres, M.E., Brumsack, H.-J., Bohrmann, G., and Emeis, K.C., 1996. Barite fronts in continental margin sediments: a new look at barium remobilization in the zone of sulfate reduction and formation of heavy barites in diagenetic fronts. *Chem. Geol.,* 127:125–139.

von Breymann, M.T., Emeis, K.-C., and Camerlenghi, A., 1990. Geochemistry of sediments from the Peru upwelling area: results from Sites 680, 682, 685, and 688. *In* Suess, E., von Huene, R., et al., *Proc. ODP, Sci. Results,* 112: College Station, TX (Ocean Drilling Program), 491–503.

Westbrook, G.K., Carson, B., Musgrave, R.J., et al., 1994. *Proc. ODP, Init. Repts.,* 146 (Pt. 1): College Station, TX (Ocean Drilling Program).

Wood, W.T., and Ruppel, C.D., 2000. Seismic and thermal investigations of the Blake Ridge gas hydrate area; a synthesis. *In* Paull, C.K., Matsumoto, R., Wallace, P.J., and Dillon, W.P. (Eds.), *Proc. ODP, Sci. Results,* 164: College Station, TX (Ocean Drilling Program), 253–264.

Yamano, M., and Uyeda, S., 1990. Heat-flow studies in the Peru Trench subduction zone. *In* Suess, E., von Huene, R., et al., *Proc. ODP, Sci. Results,* 112: College Station, TX (Ocean Drilling Program), 653–661.

You, C.-F, Gieskes, J.M., Chen, R.F., Spivack, A., and Gamo, T., 1993. Iodide, bromide, manganese, boron, and dissolved organic carbon in interstitial waters of the organic carbon-rich marine sediments: observations in the Nankai accretionary prism. *In* Hill, I.A., Taira, A., Firth, J.V., et al., *Proc. ODP, Sci. Results,* 131: College Station, TX (Ocean Drilling Program), 165–174.

Figure F1. Lithostratigraphic summary for Site 1230. TD = total depth.

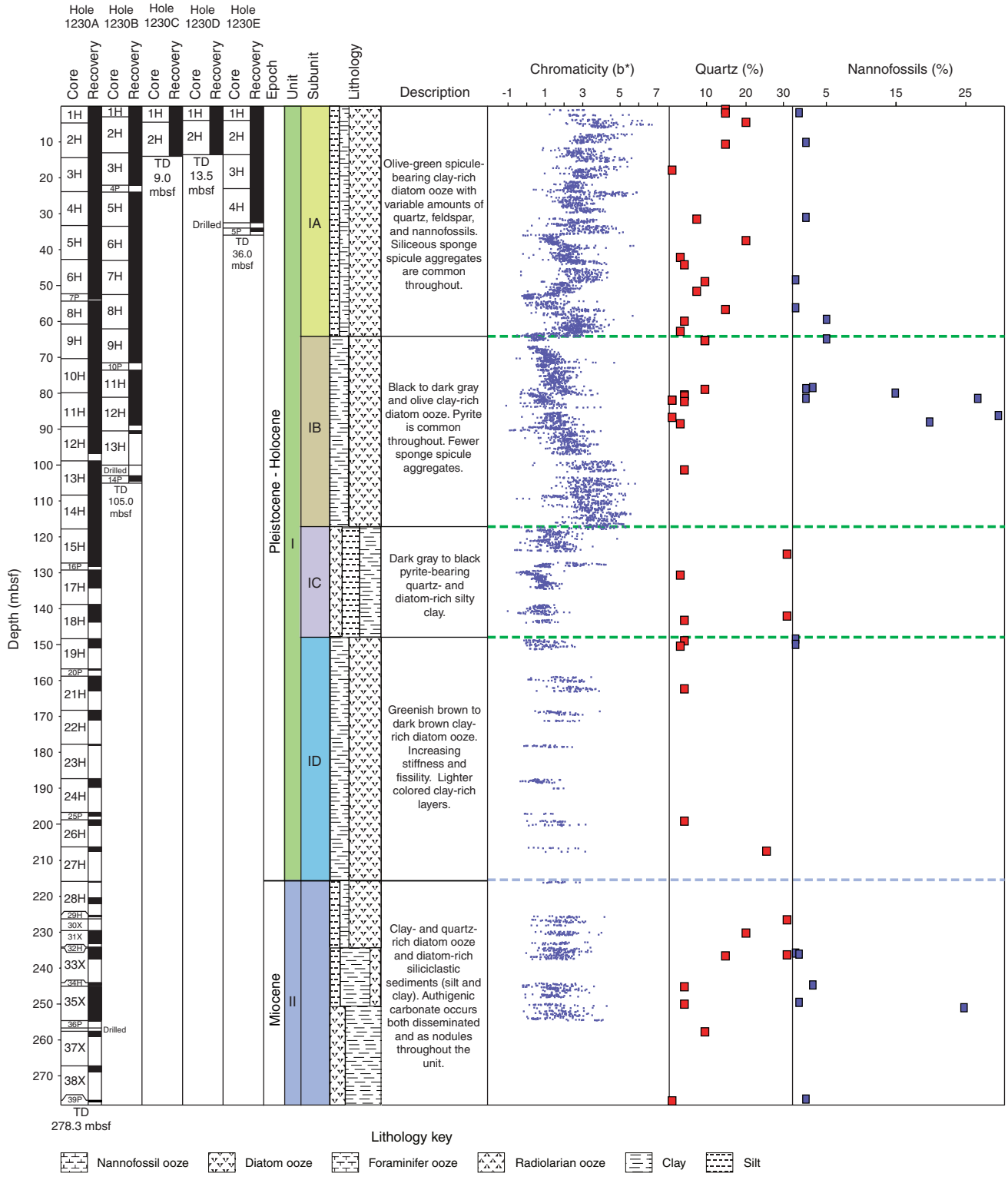

Figure F2. Close-up photographs. **A, B.** High-angle normal faults in Unit I. In both examples, the fault (the surface of which is outlined by concentration of black pyrite) offsets lighter nannofossil layers. (Continued on next four pages.)

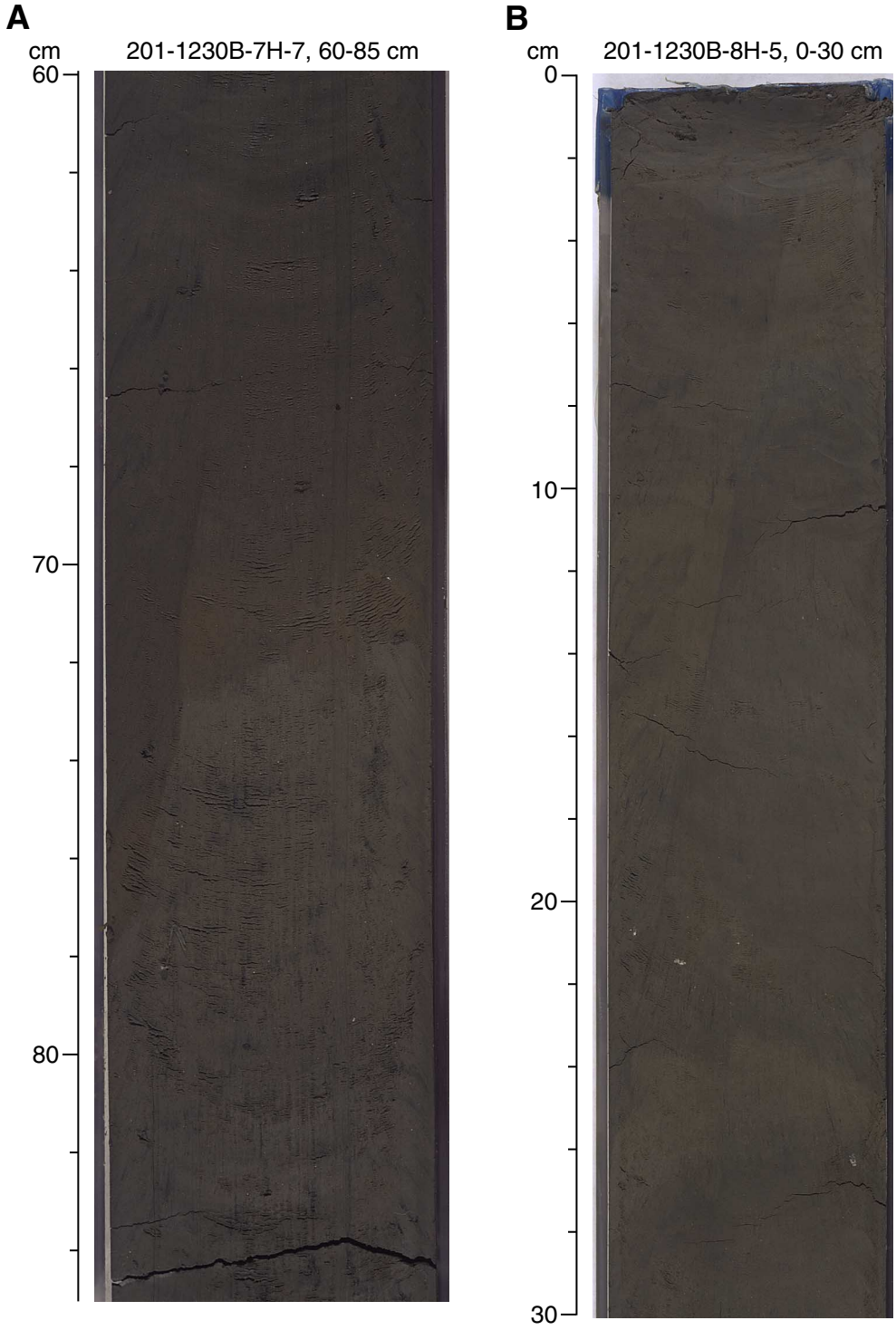

Figure F2 (continued). **C.** Yellow coarse-grained foraminifer-bearing intervals associated with pyrite-rich layers in Subunit IA. **D.** Brown bioturbated nannofossil ooze layer interbedded with a green diatom ooze. (Continued on next page.)

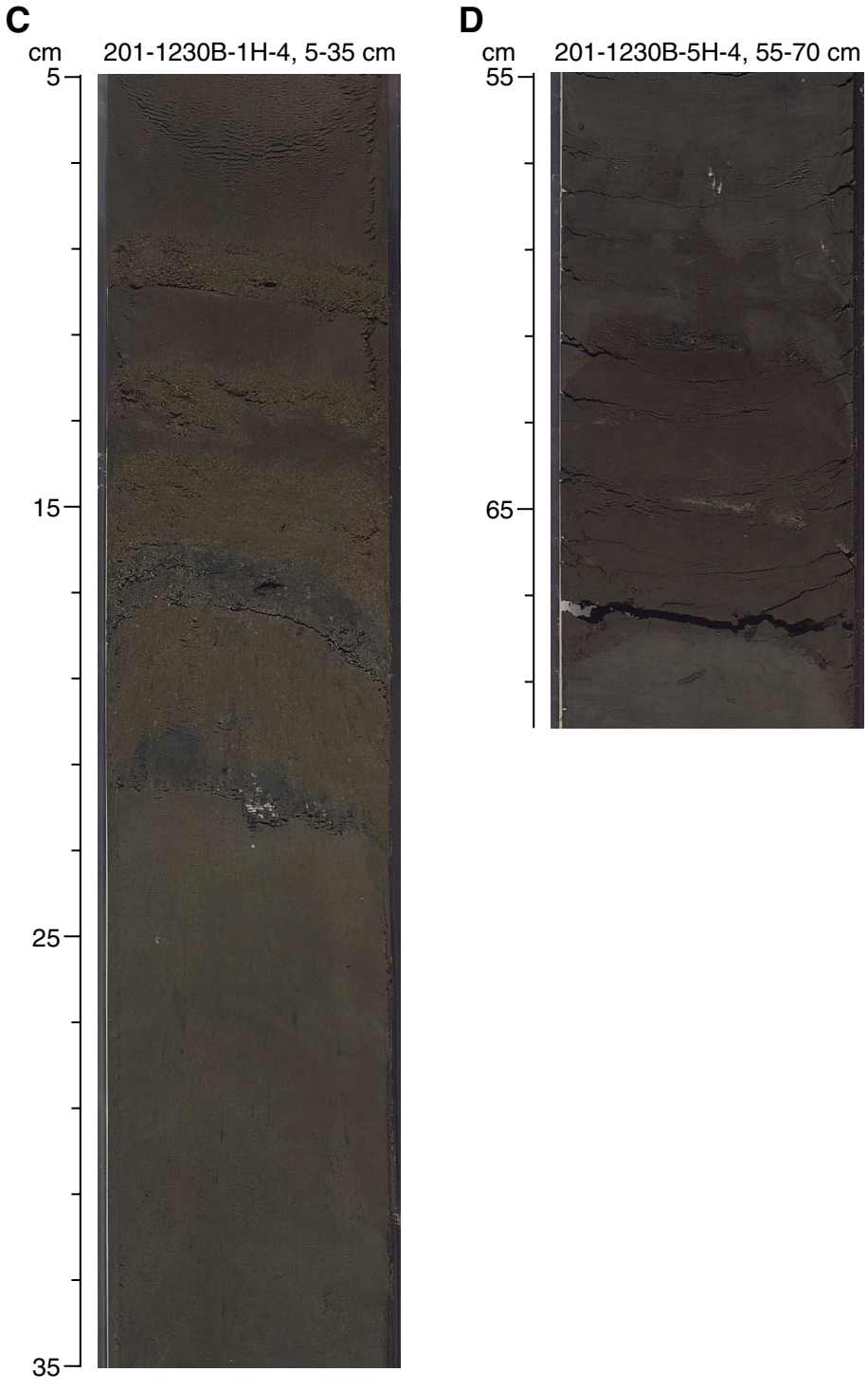

Figure F2 (continued). E. High-angle lamination, most likely a result of soft-sediment deformation in Subunit IA. **F.** Oblique fissility in Subunit ID. (Continued on next page.)

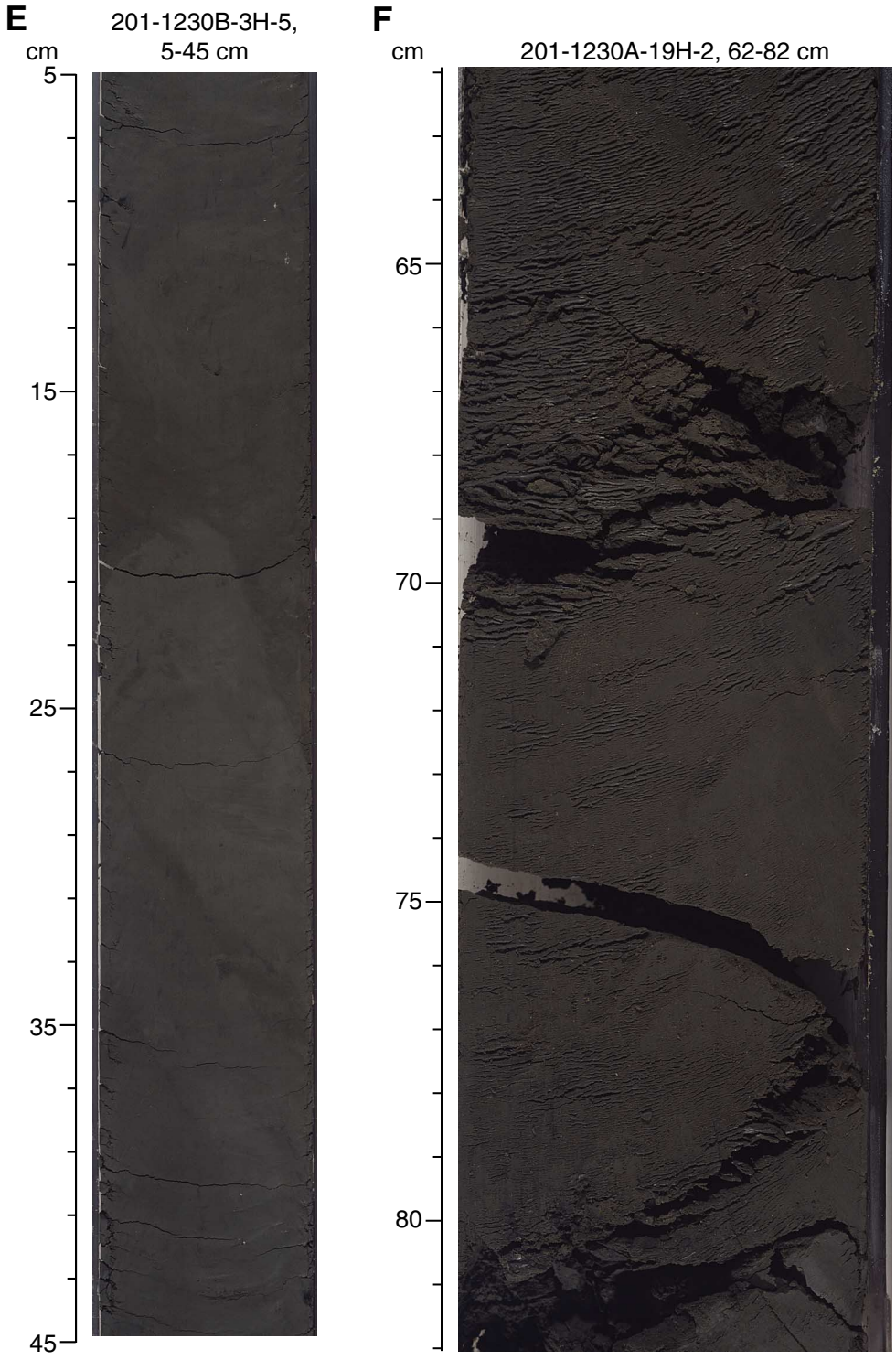

Figure F2 (continued). G. Pervasive scaly fabric in Unit II. **H.** Brecciated dolomite layer in Unit II. (Continued on next page.)

Figure F2 (continued). I. Carbonate nodules from Subunit II.

I

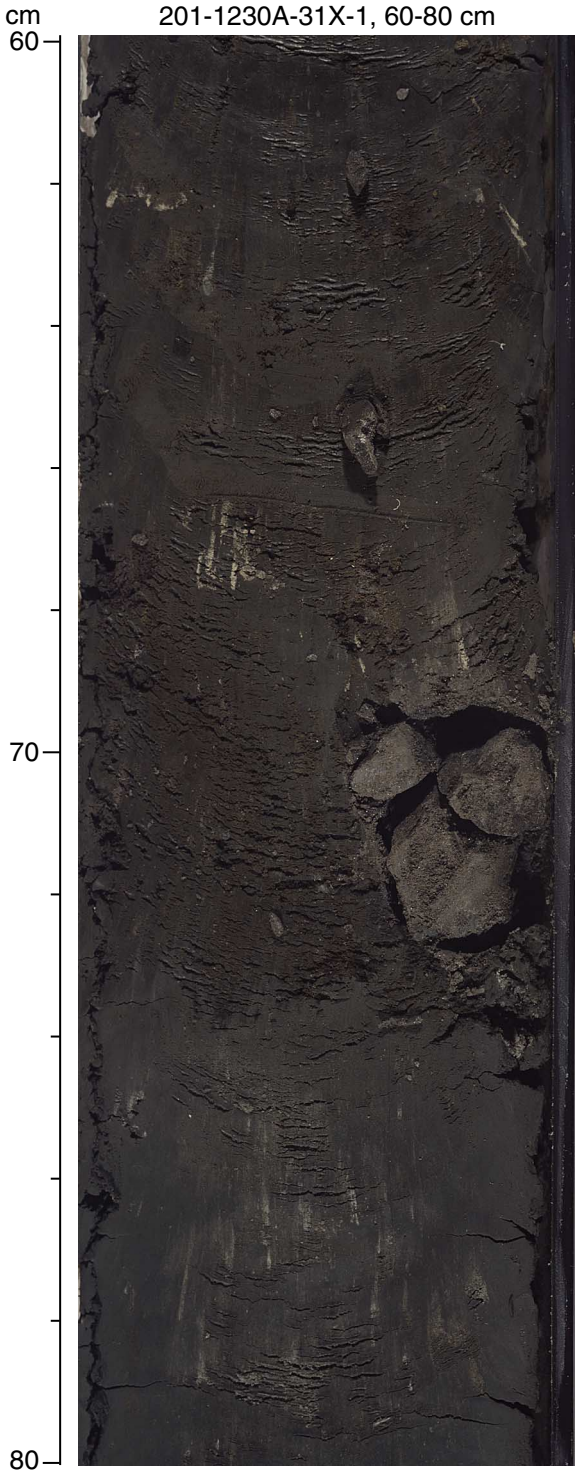

Figure F3. Concentrations of various dissolved species and other characteristics of interstitial water from Site 1230. (**A**) Yellowness, (**B**) alkalinity, (**C**) dissolved inorganic carbon (DIC), (**D**) silica, (**E**) ammonium, (**F**) phosphate, and (**G**) strontium. (Continued on next two pages.)

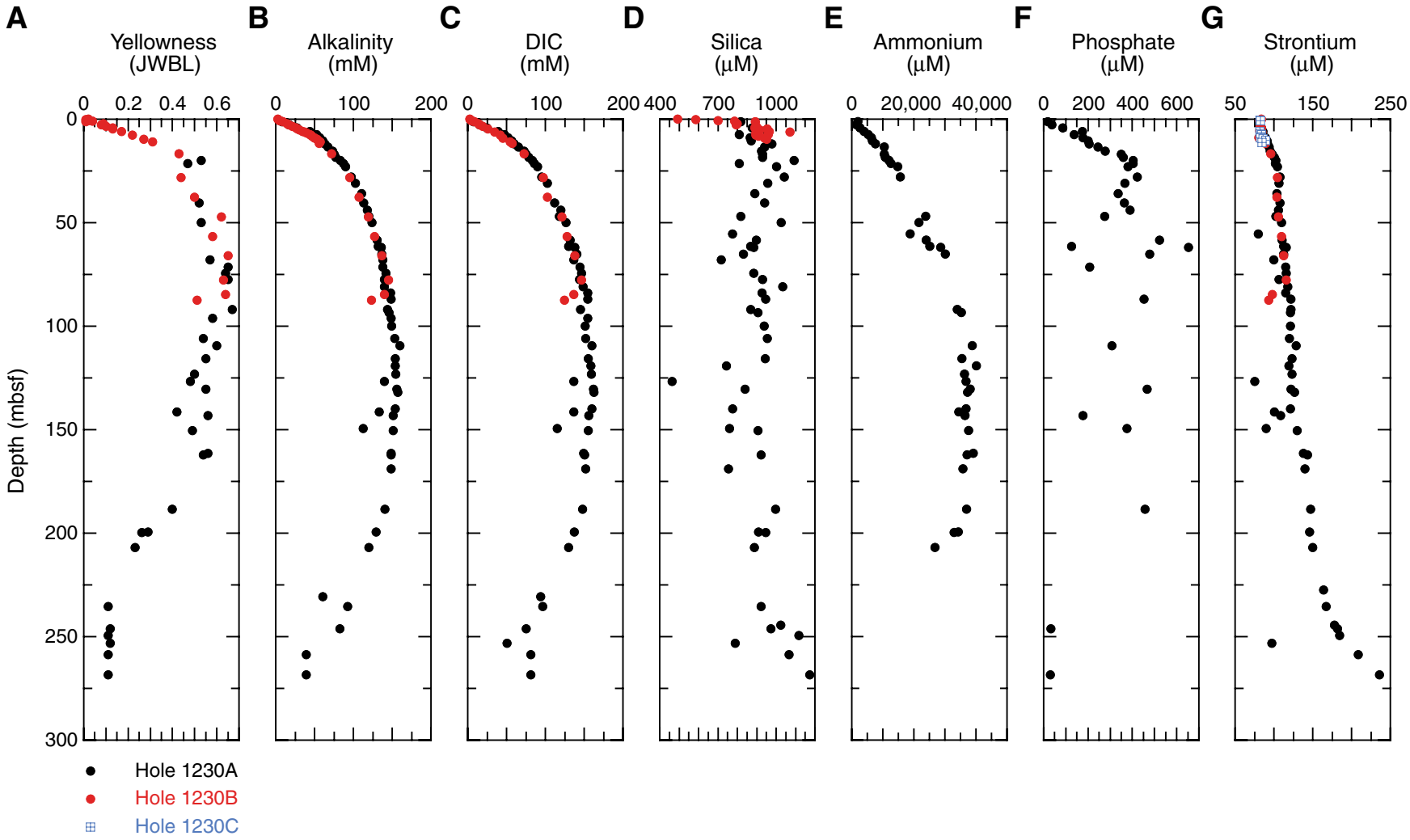

Figure F3 (continued). (**H**) Lithium, (**I**) chloride, (**J**) sulfate (note change in depth scale), (**K**) methane (concentration determined after 7 days at 22°C), (**L**) barium, (**M**) sulfide, and (**N**) iron. (Continued on next page.)

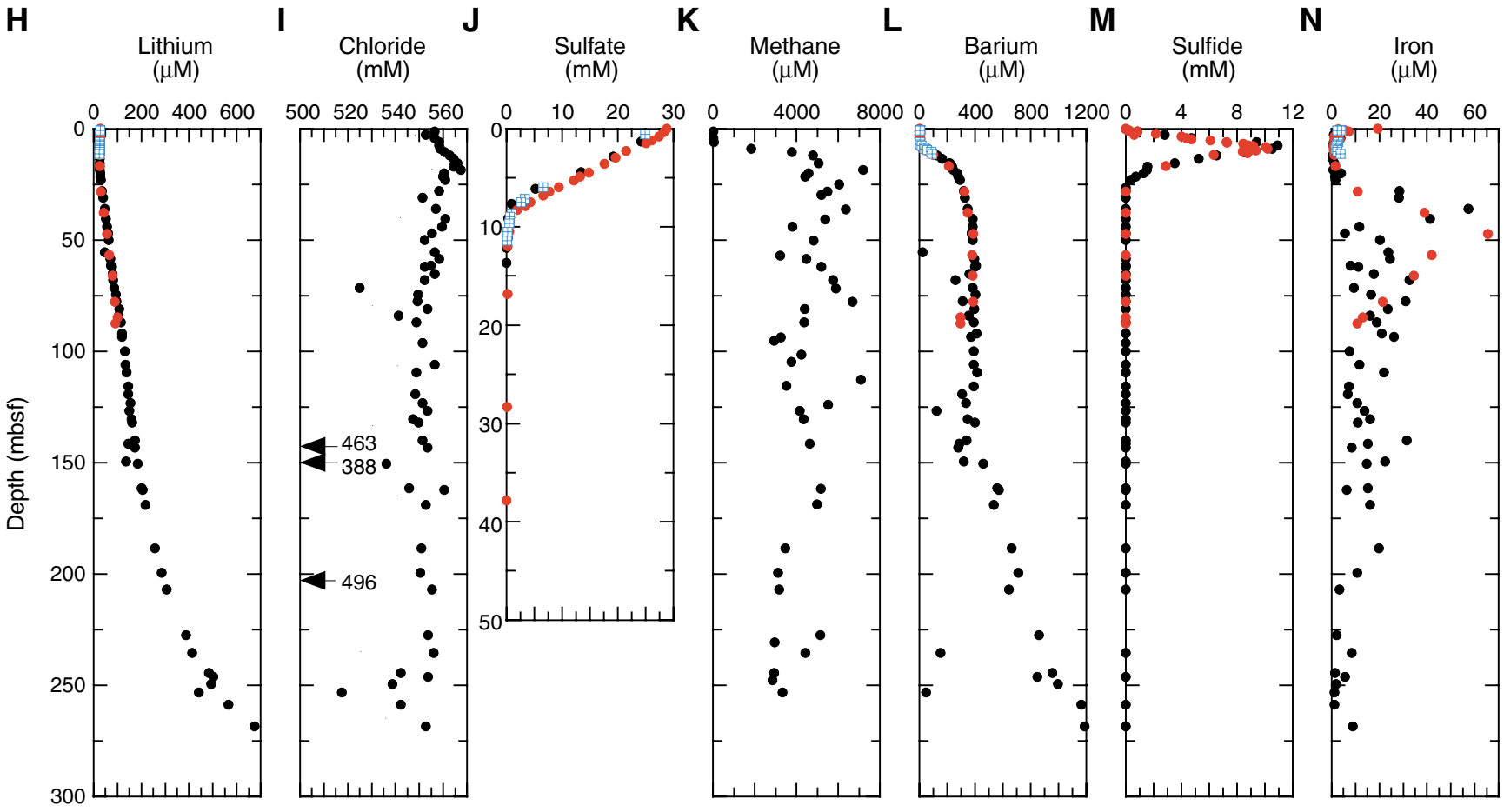

Figure F3 (continued). (**O**) manganese, (**P**) acetate, (**Q**) formate, (**R**) hydrogen, and (**S**) ethane and propane (concentration determined after 7 days at 22°C).

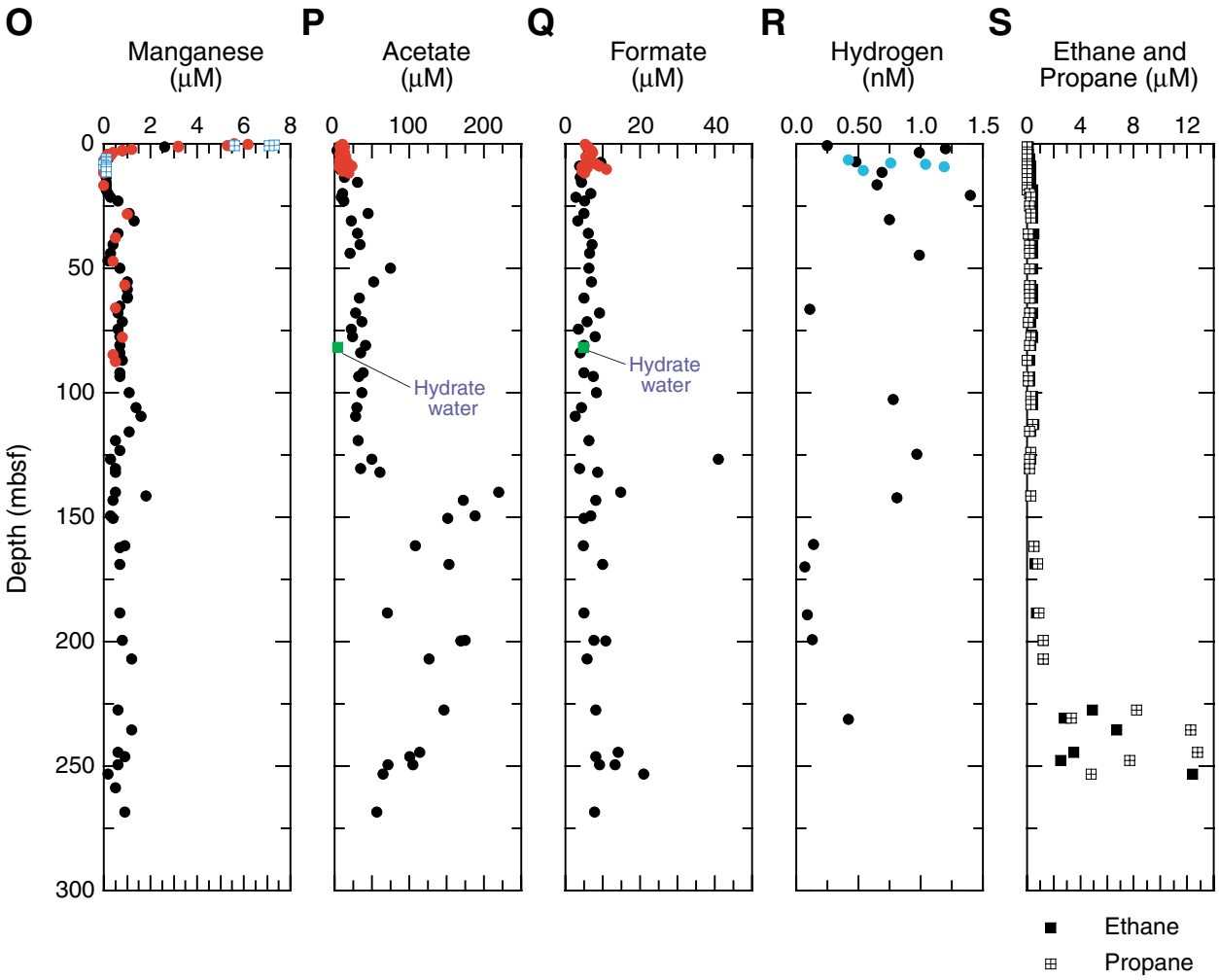

Figure F4. Downhole profiles of dissolved barium and sulfate at Site 1230 after correcting for depth offsets between holes. Circles = sulfate; squares = barium.

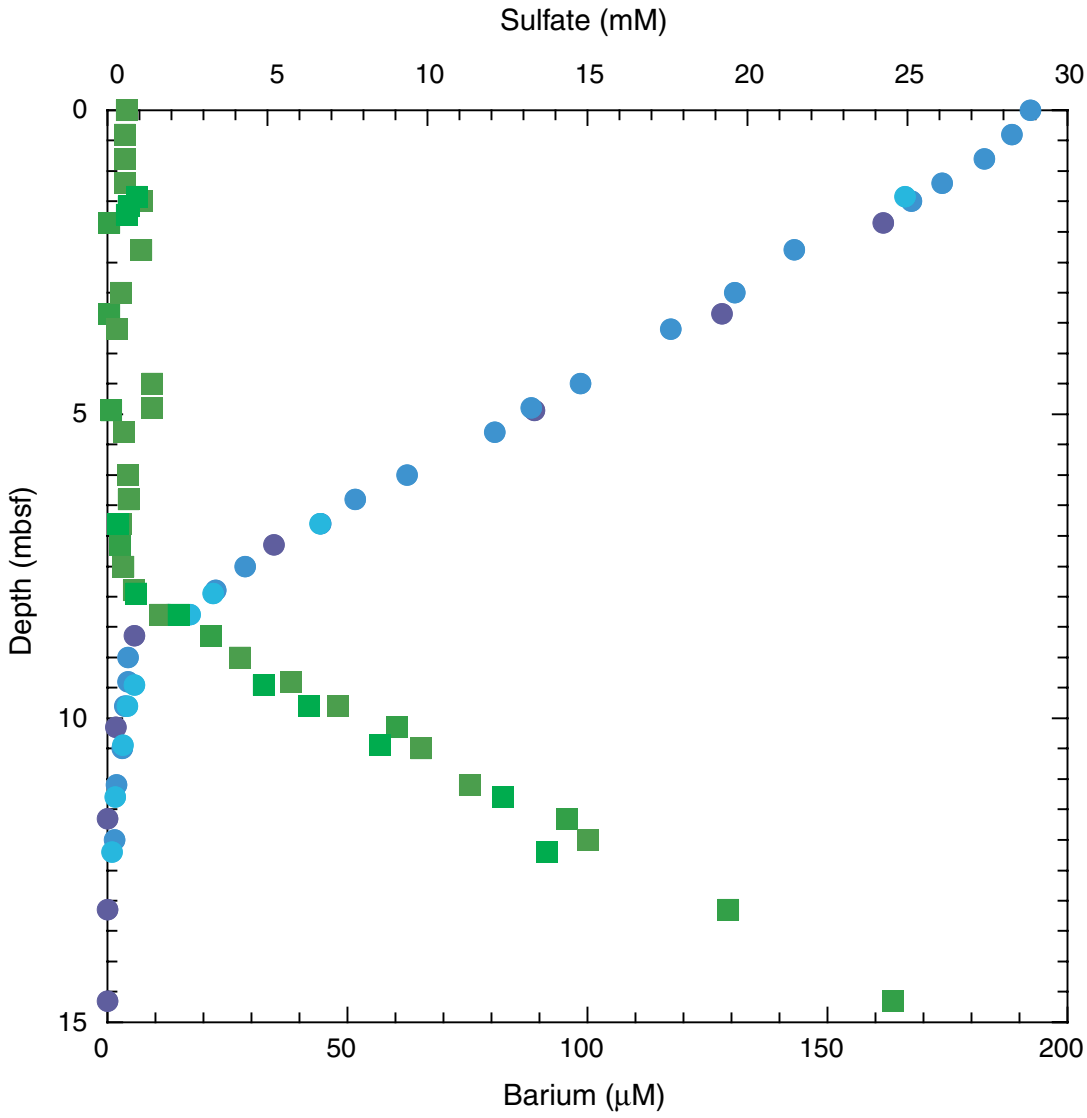

Figure F5. Depth-correlation of the top two cores of Holes 1230A, 1203B, and 1230C.

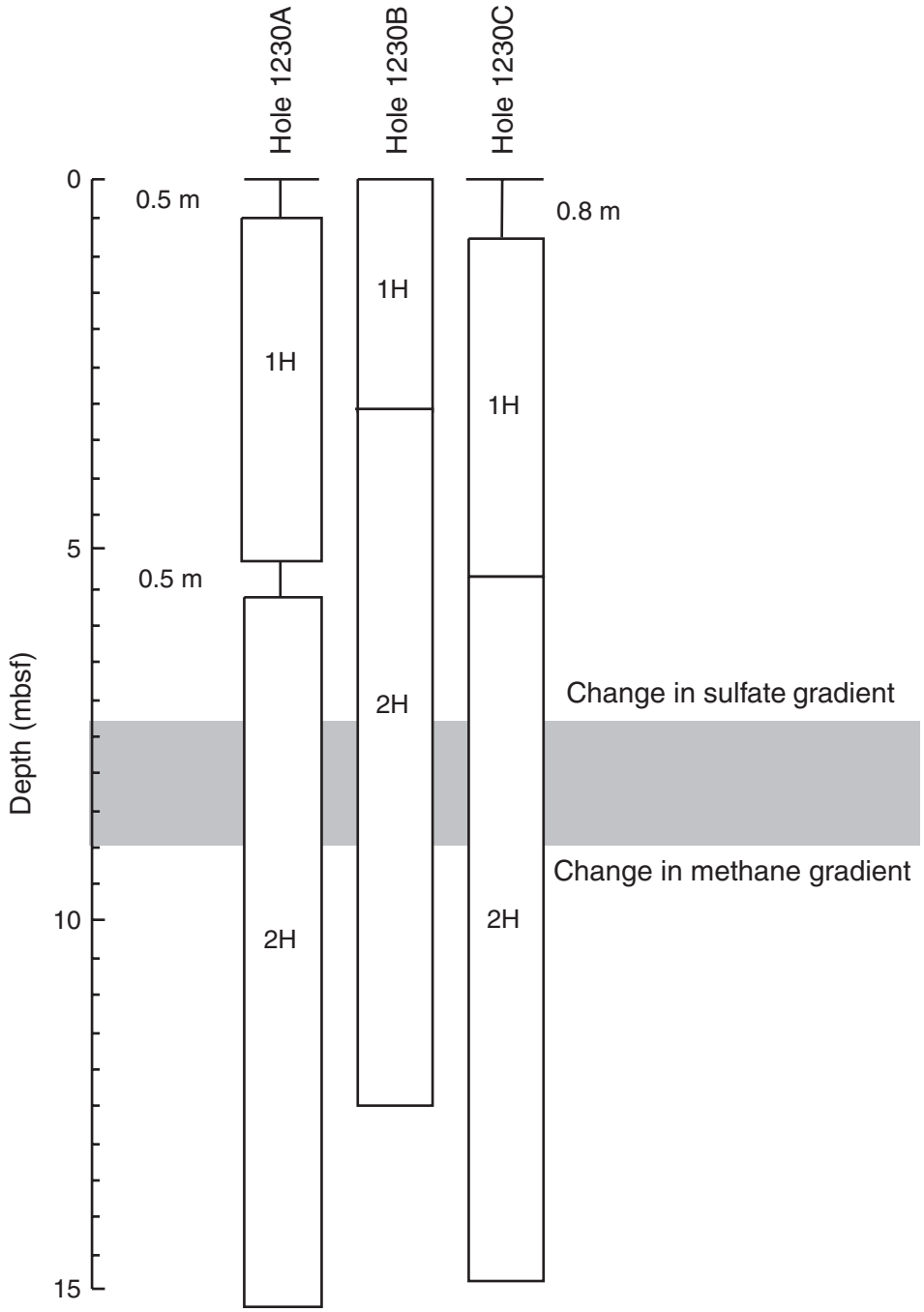

Figure F6. Downcore profiles of total organic carbon (TOC) concentrations derived from Rock-Eval pyrolysis from Sites (**A**) 1227, (**B**) 1228, and (**C**) 1230. Data are presented in Table T7, p. 97.

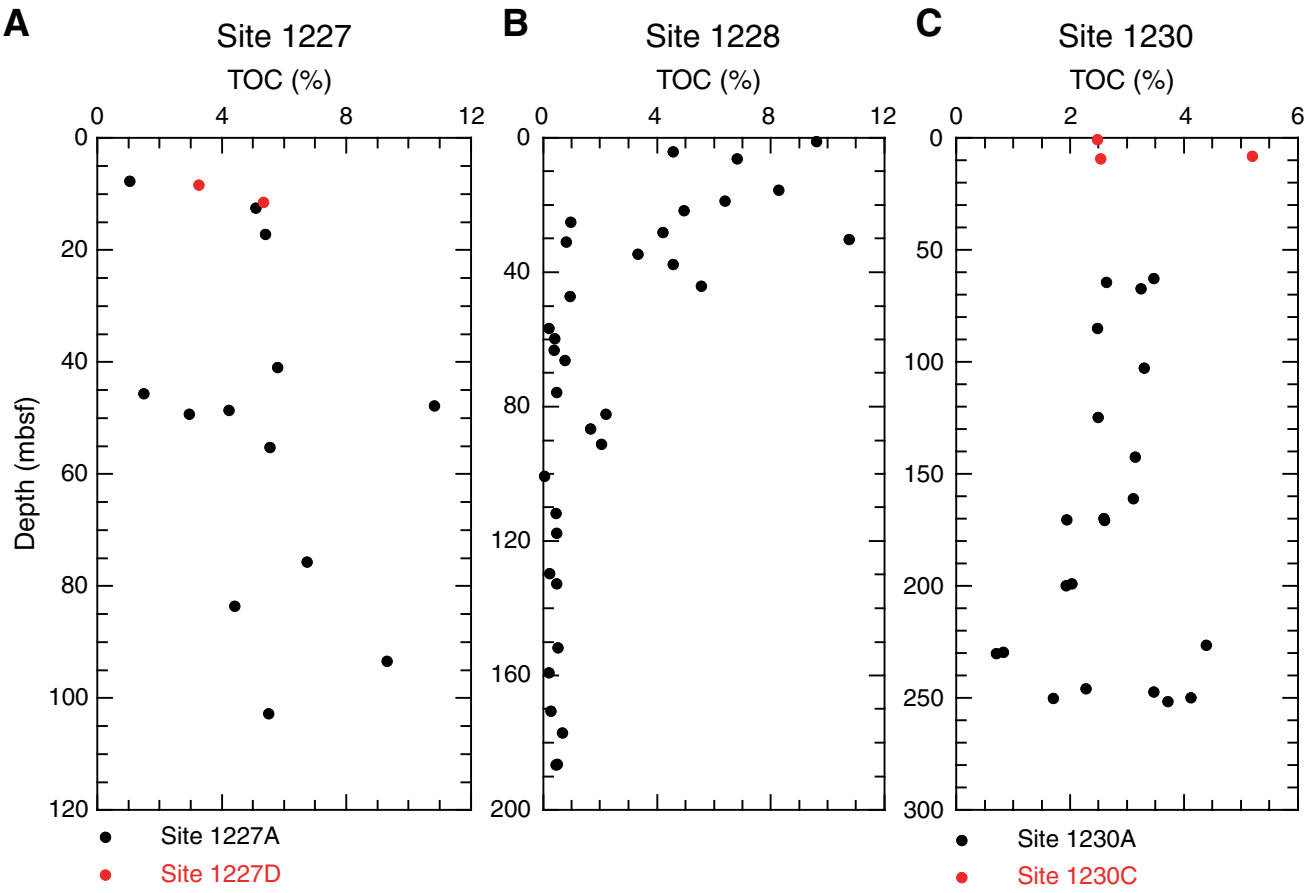

Figure F7. Graphical representation of subsampling and analysis program for the MBIO core sections from Hole 1230A. The sequence of subsections runs from the top of the core (right) toward the bottom (left). DNA = deoxyribonucleic acid, ATP = adenosine triphosphate, WRC = whole-round core. See Table T2, p. 82, in the "Explanatory Notes" chapter for explanation of sampling codes.

Hole 1230A		Fluorescent in situ hybridization (FISH)		Activity measurements: methanogenesis, thymidine incorporation, rates of hydrogen turnover, ^{35}O phosphate turnover				Sulfate reduction activity; hydrogen concentration; CH4S geochemistry; magnetic bacterial particles				Biomarkers	Fluorescent in situ hybridization (FISH)	Diffusion experiments	Cell separations	Fe/Mn/S solid-phase concentrations and stable isotopes	Enrichment	Enrichments for thermophiles	General enrichment slurry					Fluorescent in situ hybridization (FISH)		DNA		Enrichment	DNA			DNA-ODP archive	ATP-DNA	-----Top of Section-----
		N_2-flushed cutting rig										ODP cutter																							
Interval (cm)		6		6		6		6				10	10	5	5	5	5	7	6				7	7	5	5	5	5	5	5	5	5	5	5	10	
Curators Code		FISHTS	H3S	ABTP	O18B	PO4B	ABTP	SRRF	H2S	CNSS	CHNSF	BIOMHIN	BIOMHOR	DIFFF	CELLS	FESF	PRIEUR	HTEW	SLURH	SLURJ	SLURB	LDC	SLUR		FISHWR2	FISHWR	DNAM	DNAF	DNAI	ENI	DNAT	DNAN	DNAS	DNAODP	ATPS	
Sample Type		2 Syr	2 Syr	4 Syr	1 Syr	1-cm slice	8 Syr	4 Syr	4 Syr	1-cm slice	1-cm slice	WRC	WRC	WRC	WRC	WRC	WRC	60-mL + 2 x 5-mL syr	2 x 5-mL syr	1 x 5-mL syr	2 x 5-mL syr	1 x 5-mL syr	60-mL syr	60-mL syr	WRC	WRC	WRC	WRC	WRC	WRC	WRC	WRC	WRC	WRC	WRC	
Package Type		Poly-bag	Al-bag	Anaer. Jar	Al-bag	Poly-bag	Anaer. Jar	Al-Bag	Poly-bag	Poly-bag	Al-bag	Poly-bag	Poly-bag	Al-bag	Poly-bag	Al-bag	Al-bag	Anaer. Jar	Al-bag	Al-bag	Anaer. Jar	Al-bag	Al-bag	Al-bag	Al-bag	Poly-bag	Poly-bag	Poly-bag	Poly-bag	Al-bag	Poly-bag	Poly-bag	Poly-bag	Poly-bag	Poly-bag	
Package Atmosphere			N_2	N_2	N_2		N_2	N_2	N_2		Vac pack			Vac pack		Vac pack	N_2/An-cult	N_2	N_2	N_2	N_2	N_2	N_2	N_2	N_2					N_2						
Temperature Destination		+4˚C	+4˚C Radvan	+4˚C Radvan	+4˚C	-20˚C	+4˚C Radvan	+4˚C Radvan	+4˚C	+4˚C	+4˚C	-80˚C	-80˚C	+4˚C	-80˚C	-20˚C	+4˚C	+4˚C	+4˚C	+4˚C	+4˚C	+4˚C	on ice	on ice	+4˚C	-80˚C	-80˚C	-80˚C	-80˚C	+4˚C	-80˚C	-80˚C	-80˚C	-80˚C	-80˚C	Sediment Depth (mbsf)
Core	Section																																			top
1H	1	1	1	1	1	1	1	1	1	1	1	1	-	-	-	1	-	1	1	1	1	1	1	1	1	1	-	-	1	-	1	1	1	1	1	0.0
1H	2	1	1	1	1	1	1	1	1	1	1	1	-	1	1	1	-	-	-	-	-	-	-	-	-	-	-	-	1	1	1	1	1	1	1	1.5
1H	3	1	1	1	1	1	1	1	1	1	1	1	-	-	-	1	-	-	-	-	-	-	-	-	1	1	-	-	1	-	1	1	1	1	1	3.0
2H	2	1	1	1	1	1	1	1	1	1	1	1	1	-	-	1	1	1	1	1	1	1	1	1	1	1	-	-	1	-	1	1	1	1	1	6.3
2H	5	1	1	1	1	1	1	1	1	1	1	1	-	1	1	1	-	-	-	-	-	-	-	-	1	1	-	-	1	-	1	1	1	1	1	10.8
3H	2	1	1	1	1	1	1	1	1	1	1	1	1	-	-	1	1	-	-	-	-	-	-	-	1	1	-	1	1	-	1	1	1	1	1	15.8
3H	5	1	1	1	1	1	1	1	1	1	1	1	-	-	-	1	-	-	-	-	-	-	-	-	-	-	-	-	1	-	1	1	1	1	1	20.3
4H	5	1	1	1	1	1	1	1	1	1	1	1	1	-	-	1	1	-	-	-	-	-	-	-	1	1	-	1	1	-	1	1	1	1	1	29.8
6H	2	1	1	1	1	1	1	1	1	1	1	1	-	-	-	1	-	-	-	-	-	-	-	-	-	-	1	-	1	-	1	1	1	1	1	44.3
9H	5	1	1	1	1	1	1	1	1	1	1	1	1	1	1	1	1	1	1	1	1	1	1	1	1	1	-	1	1	-	1	1	1	1	1	65.5
11H	4	1	1	1	1	1	1	1	1	1	1	1	1	-	-	1	1	-	-	-	-	-	-	-	-	-	-	1	1	-	1	1	1	1	1	84.3
13H	3	1	1	1	1	1	1	1	1	1	1	1	1	-	-	1	1	1	1	1	1	1	1	1	1	1	1	1	1	-	1	1	1	1	1	101.8
15H	6	1	1	1	1	1	1	1	1	1	1	1	1	-	-	1	1	-	1	1	1	1	1	1	-	-	-	1	1	-	1	1	1	1	1	124.0
18H	3	1	1	1	1	1	1	1	1	1	1	1	-	-	-	1	-	-	-	-	-	-	-	-	-	-	1	-	1	-	1	1	1	1	1	141.8
21H	3	1	1	1	1	1	1	1	1	1	1	1	1	-	-	1	1	-	-	-	-	-	-	-	-	-	-	1	1	1	1	1	1	1	1	160.3
22H	2	1	1	1	1	1	1	1	1	1	1	1	1	-	1	1	1	-	-	-	-	-	-	-	1	1	-	1	1	-	1	1	1	-	1	169.2
24H	2	1	1	1	-	1	1	1	1	1	1	1	-	-	-	1	-	-	-	-	-	-	-	-	-	-	1	-	1	-	1	1	1	1	1	188.8
26H	1	1	1	1	-	1	1	1	1	1	1	-	-	-	-	-	-	-	-	-	-	-	-	-	-	-	-	-	-	-	-	-	-	-	-	198.8
27H	1	-	-	-	-	-	-	-	-	-	-	1	-	-	-	1	1	-	-	-	-	-	-	-	-	-	-	1	1	-	1	1	1	1	1	206.3
30X	1	-	-	-	-	-	-	-	-	-	-	-	-	-	-	-	-	-	-	-	-	-	-	-	-	-	-	-	-	-	1	-	-	1	-	226.3
31X	2	1	1	1	1	1	1	1	1	1	1	1	1	-	-	1	1	-	-	-	-	-	-	-	1	1	1	1	1	-	1	1	1	1	1	231.1
35X	3	1	1	1	1	1	1	1	-	-	-	1	-	-	-	1	-	-	-	-	-	-	-	-	-	-	-	-	1	-	1	1	1	1	1	248.1
37X	1	-	-	-	-	-	-	-	-	-	-	1	1	-	-	1	-	-	-	-	-	-	-	-	1	1	-	-	1	-	1	1	1	-	1	257.6
38X	1	-	-	1	-	1	1	-	-	-	-	1	-	-	-	1	1	1	1	1	1	1	1	1	1	1	-	-	1	-	1	1	1	-	1	267.2
	TOTAL	20	20	21	18	21	21	20	19	19	19	22	11	3	4	22	12	5	6	6	6	6	6	6	12	12	6	11	22	2	23	22	22	20	22	

Figure F8. Graphical representation of subsampling and analysis program for the MBIO core sections from Hole 1230B. The sequence of subsectioning runs from the top of the core (right) toward the bottom (left). * = 5-cm³ WRC samples were taken from the bottom of the subsection; otherwise, 2 × 5-cm³ syringes were taken from the BIOMHIN sample. DNA = deoxyribonucleic acid, WRC = whole-round core. See Table T2, p. 82, in the "Explanatory Notes" chapter for explanation of sampling codes.

Hole 1230B			Biomarkers	DNA				------ Top of Section ------
			ODP cutter					
Interval (cm)			10	0/5	5	5	5	
CURATORS CODE			BIOMHIN	DNAT	DNAI	DNAS	DNAN	
Sample Type			10-cm WRC	WRC or 2 x 5 cm³ syr	5-cm WRC	5-cm WRC	5-cm WRC	
Package Type			Poly-bag	Poly-bag	Poly-bag	Poly-bag	Poly-bag	
Temperature			-80˚C	-80˚C	-80˚C	-80˚C	-80˚C	Sediment Depth (mbsf)
Core	Section	Subsect.						top
2H	2	1	1	1	1	1	1	4.6
2H	2	2	1	1	1	1	1	5.0
2H	2	3	1	1*	1	1	1	5.4
2H	3	1	1	1	1	1	1	6.1
2H	3	2	1	1	1	1	1	6.5
2H	3	3	1	1*	1	1	1	6.9
2H	4	1	1	1	1	1	1	7.6
2H	4	2	1	1	1	1	1	8.0
2H	4	3	1	1*	1	1	1	8.4
2H	5	1	1	1	1	1	1	9.1
2H	5	2	1	1	1	1	1	9.5
2H	5	3	1	1*	1	1	1	9.9
		TOTAL	11	8	11	11	11	

Figure F9. A. Graphical representation of subsampling and analysis program for the MBIO core sections from Hole 1230C. The sequence of subsectioning runs from the top of the core (right) toward the bottom (left). ATP = adenosine triphosphate, DNA = deoxyribonucleic acid, cDNA = combined DNA sampling with 5-cm³ syringes, CE = combined enrichment sampling, EWI = enrichment for thermophiles (see Table T11, p. 102), WRC = whole-round core. **B.** An expanded view of the cutting sequence of Sections 201-1230C-2H-2 through 2H-6. [1] = special handling slop: cut and cap and stand upright in the refer. See Table T2, p. 82, in the "Explanatory Notes" chapter for explanation of sampling codes.

A

Hole 1230C

Curators Code			6 cm			6 cm		6 cm	6 cm										Comb. Enrichments (CE)								COMBINED DNA + FISH (CDNA)							
			FISHTS	AODC	H3S	ABTP	H2S	PO4B	ABTP	SRRF	AMO	CNSS	CHNSF	BIOMHIN	SRRWRF	FeS	AMO	SLURH	SLURB	HTEW	ENI	FISHWR2	FISHWR	FISHTS	DNAI	DNAT	DNAN	DNAS	DNAODP	ATPS
Core	Section	top	2 x 5 mL	1 mL	2 x 5 mL	4 x 5 mL	4 x 5 mL		8 x 5 mL	4 x 5 mL	4 x 5 mL	1-cm slice		10 cm	5 cm	5 cm	1 x 60 mL	2 X 5 mL	2 x 5 mL	5-cm WRC	5-cm WRC	5 cm	5 cm	2 x 5 mL	1 x 5 mL	1 x 5 mL	1 x 5 mL	1 x 5 mL	1 x 5 mL	5-cm WRC
0 (slop)				[1]		[1]			[1]						[2]					25 mL		[1]								
1H	1	0.0								1		1	1		2	1				1 x 60 mL										
1H	2	1.5																		1 x 60 mL										
1H	3	3.0																												
2H	1	4.5																												
2H	2	6.0				1	1		1	1	1			2			1	1	1			2	2	1			1	1	1	1
2H	3	7.5				1	1		1	1	1			2			1	1	1			2	2	1	1	1	1	1	1	1
2H	4	9.0				1	1		1	1	1			2			1	1	1		1	2	2	1	1	1	1	1	1	1
2H	5	10.5				1	1		1	1	1 WRC			2	2		1	1	1	1 x 60 mL		2	2	1	1	1	1	1	1	1
2H	6	12.0																				1	1							

B

Sampling order in core sections 2H-2, 2H-3, 2H-4, 2H-5, and 2H-6

2H-2	cr	154	145	140	135	130	125	120	115	110	105	100	95	90	85	80	75	70	65	60	55	50	45	40	35	30	25	20	15	10	5	0							
			BIOHIN		FISHWR	FISHWR2	AMO	IW											FeS	SRR	ABTP	ABTP	CE	CDNA	FISH2B	ATPS		FISHWR	BIOHIN		IW									
	m	7.5	7.45	7.4	7.35	7.3	7.25	7.2	7.15	7.1	7.05	7	6.95	6.9	6.85	6.8	6.75	6.7	6.65	6.6	6.55	6.5	6.45	6.4	6.35	6.3	6.25	6.2	6.15	6.1	6.05	6	m						
2H-3	cr	148	143	138		130	125	120	115	110	105	100	95	90	85	80	75	70	65	60	55	50	45	40	35	30	25	20	15	10	5	0							
			BIOHIN			DNAT		AMO	IW	ENI		BIOHIN		FISHWR	SRR	ABTP	ABTP	CDNA	CE	FISH2B	ATPS	ATPS	FeS/AODC	SRR	ABTP	ABTP	CDNA	CE/AODC	FISH2B	ATPS		FISHWR	IW						
	m	9	8.95	8.9	8.85	8.8	8.75	8.7	8.65	8.6	8.55	8.5	8.45	8.4	8.35	8.3	8.25	8.2	8.15	8.1	8.05	8	7.95	7.9	7.85	7.8	7.75	7.7	7.65	7.6	7.55	7.5	m						
2H-4	cr	147		140	135	130	125	120	115	110	105	100	95	90	85	80	75	70	65	60	55	50	45	40	35	30	25	20	15	10	5	0							
			FeS		FISHWR	FISH2B	BIOHIN		AMO										IW	FISHWR	BIOHIN	ENI	SRR	ABTP	ABTP/H2S	CDNA	CE	ATPS		FISH2B	IW									
	m	10.45		10.4	10.35	10.3	10.25	10.2	10.15	10.1	10.05	10	9.95	9.9	9.85	9.8	9.75	9.7	9.65	9.6	9.55	9.5	9.45	9.4	9.35	9.3	9.25	9.2	9.15	9.1	9.05	9	m						
2H-5	cr	150	145	140	135	130	125	120	115	110	105	100	95	90	85	80	75	70	65	60	55	50	45	40	35	30	25	20	15	10	5	0							
			FISHWR	FISH2B	BIOHIN		SRRWRF	SRRWRF	HTEW	AMO	AMOWR	SRRWRF		IW						BIOHIN	FISHWR	SRR	ABTP	ABTP	CDNA	CE	FISH2B	ATPS		IW									
	m	12	11.95	11.9	11.85	11.8	11.75	11.7	11.65	11.6	11.55	11.5	11.45	11.4	11.35	11.3	11.25	11.2	11.15	11.1	11.05	11	10.95	10.9	10.85	10.8	10.75	10.7	10.65	10.6	10.55	10.5	m						
2H-6	cr	150	145	140	135	130	125	120	115	110	105	100	95	90	85	80	75	70	65	60	55	50	45	40	35	30	25	20	15	10	5	0							
			FISHWR	FISH2B																																			
	m	13.5	13.45	13.4	13.35	13.3	13.25	13.2	13.15	13.1	13.05	13	12.95	12.9	12.85	12.8	12.75	12.7	12.65	12.6	12.55	12.5	12.45	12.4	12.35	12.3	12.25	12.2	12.15	12.1	12.05	12	m						

Figure F10. Total prokaryotic cells (solid circles) and the percentage of those cells involved in cell division (open circles) with depth at Site 1230. Dividing cell percentages become increasingly unreliable as total cell counts decrease below 1×10^7 cells/cm^3 and within-sample variability rises due to the low number of cells counted. Vertical dashed line on the left represents the detection limit at 2.5×10^5 cells/cm^3.

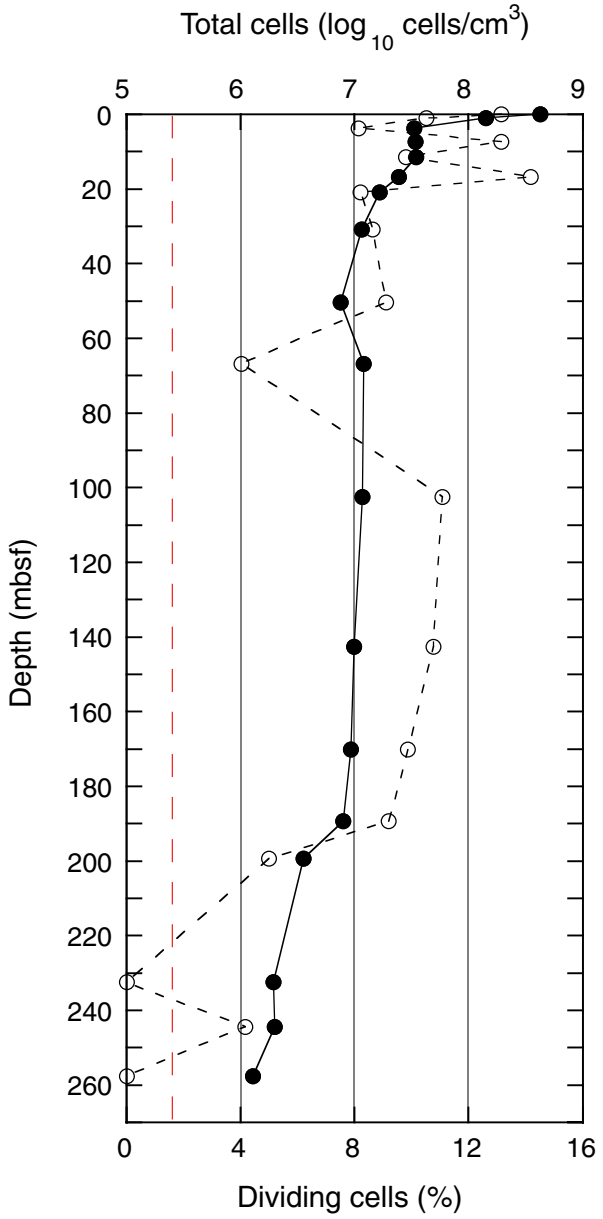

Figure F11. Profile of total prokaryotic cells at Site 1230. Heavy dashed line is a regression line derived from previous ODP legs and updated from Parkes et al. (1994) ($\log_{10}$ cells = 8.03 – 0.66 $\log_{10}$ depth), lighter dashed lines represent the ±2-σ envelopes of data based on censused data from previous ODP legs.

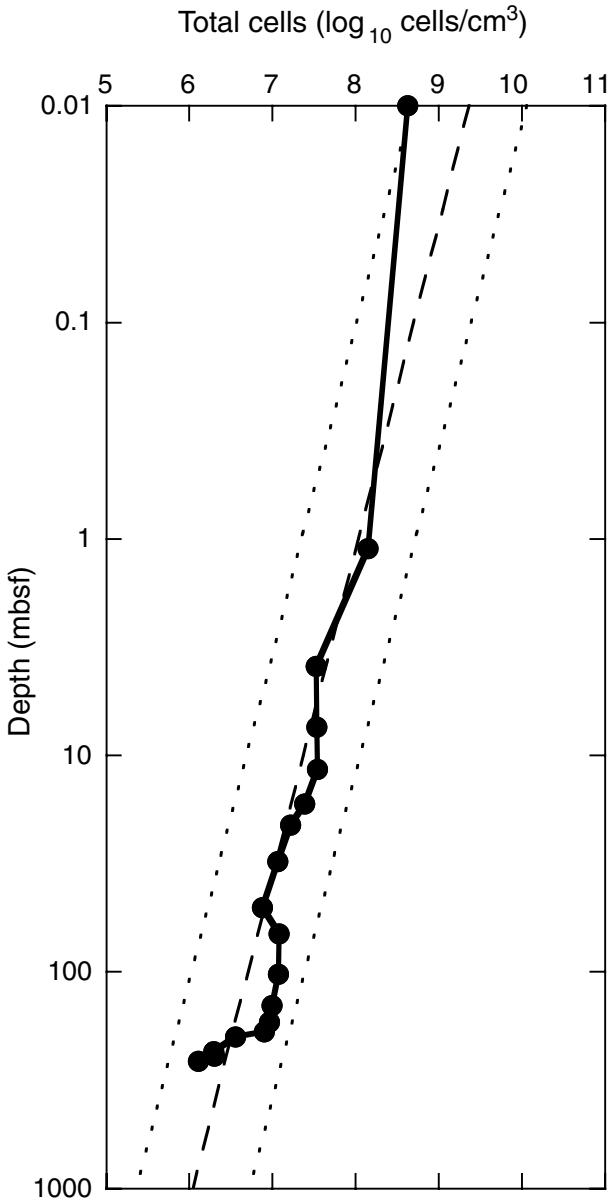

Figure F12. Profile of total prokaryotic cells at Site 1230 between 65 and 245 mbsf and with a smoothed line connecting the data. Heavy dashed lines are extrapolated tangents to the profile line with an intersect at the estimated interface depth between Unit I and Unit II sediments, indicating a sediment hiatus at 214 mbsf.

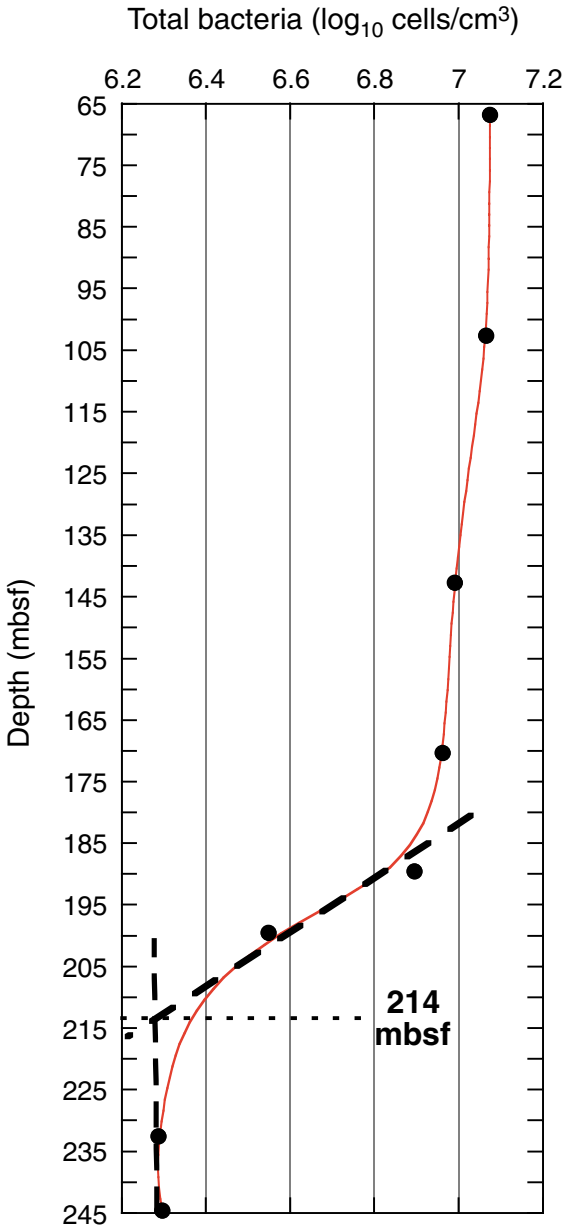

Figure F13. A. Catwalk scan of Core 201-1230A-26H. Average temperature of the core liner is ~20°C. The cold spot is 15.7°C. **B.** Core 201-1230A-26H split at the location of the core liner cold spot. Visual (left) and infrared (right) images were both taken with the IR camera. Average temperature of the core sediment is ~15°C. The cold spot is –1.7°C. **C.** The same section after subsampling for disseminated hydrate. Visual (left) and infrared (right) images were both taken with the IR camera. Average temperature of the core sediment is ~15°C. The minimum temperature recorded after subsampling the cold spot, reaching –3.2°C, was even lower than the split-core image.

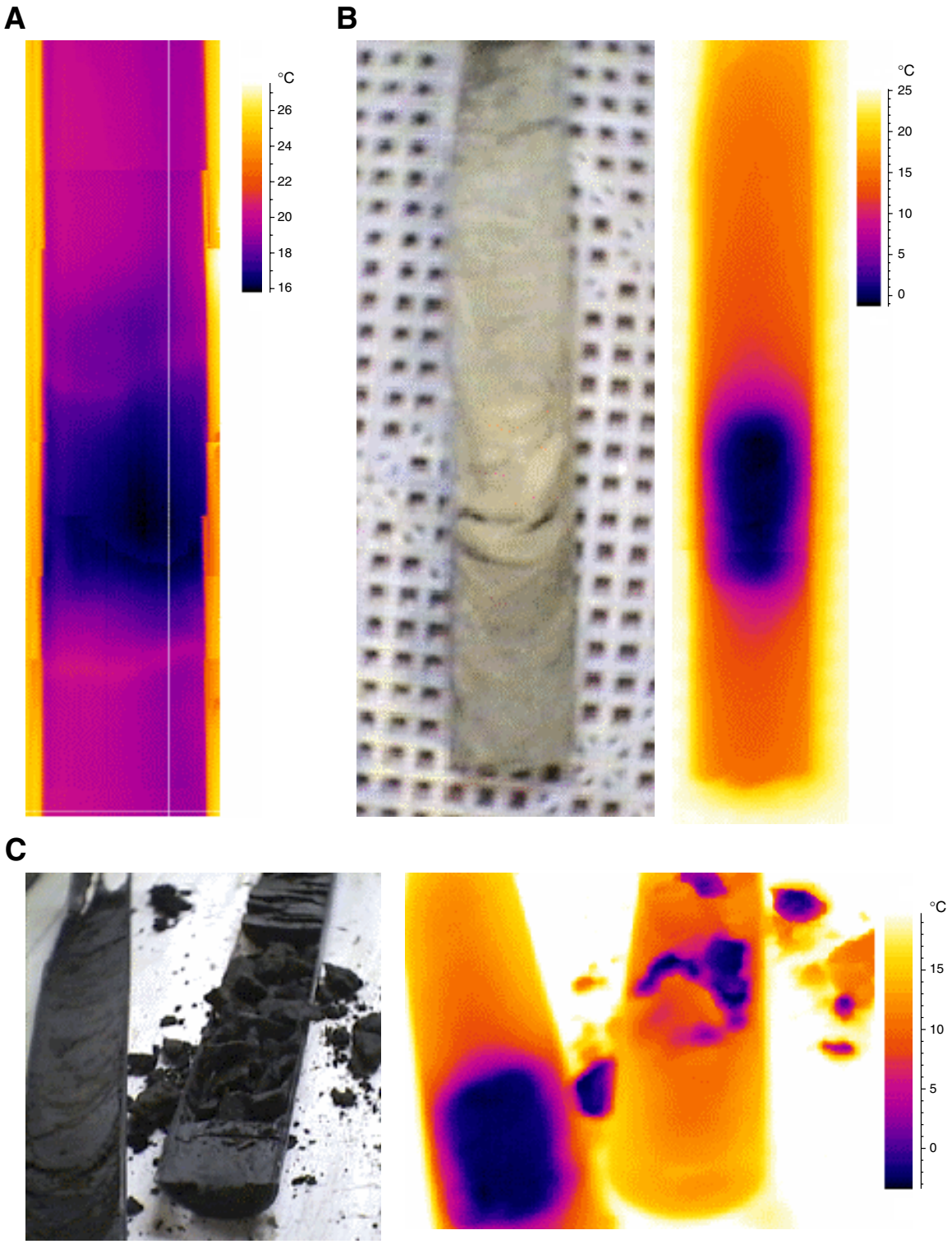

Figure F14. Core liner temperature profile measured on the catwalk using the IR camera for Hole 1230A. Hydrate locations visually confirmed (by presence of white hydrate or inferred from bubbling of the sediment) are noted by a gray band and a box around the hole and core number. Hydrate locations suspected based on core liner temperatures but not confirmed by recovery of visible hydrate or bubbling of sediment are noted by a gray band with the hole and core number in italics.

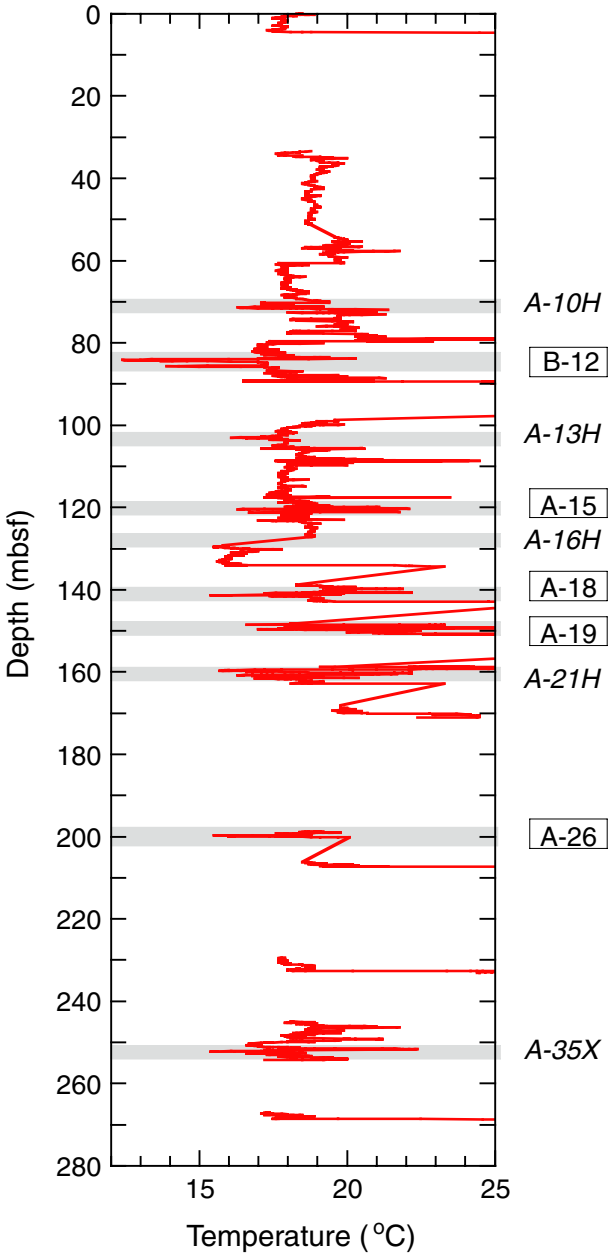

Figure F15. Core liner temperature profiles for Holes 1230A and 1230B generated from data measured on the catwalk using the IR camera.

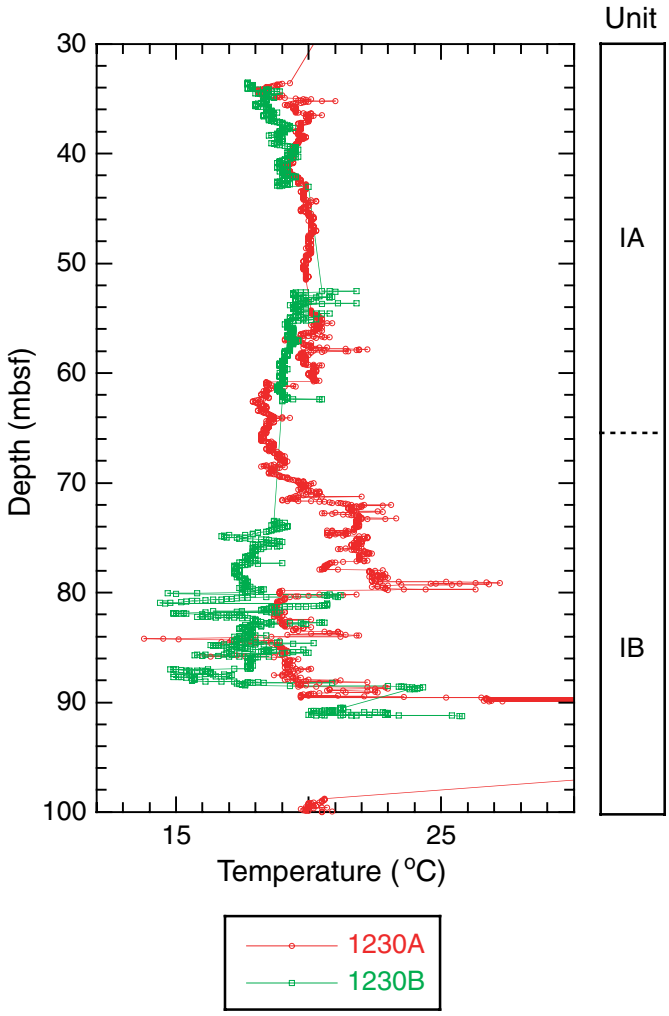

Figure F16. Multisensor track measurements of volume magnetic susceptibility for Holes 1230A and 1230B.

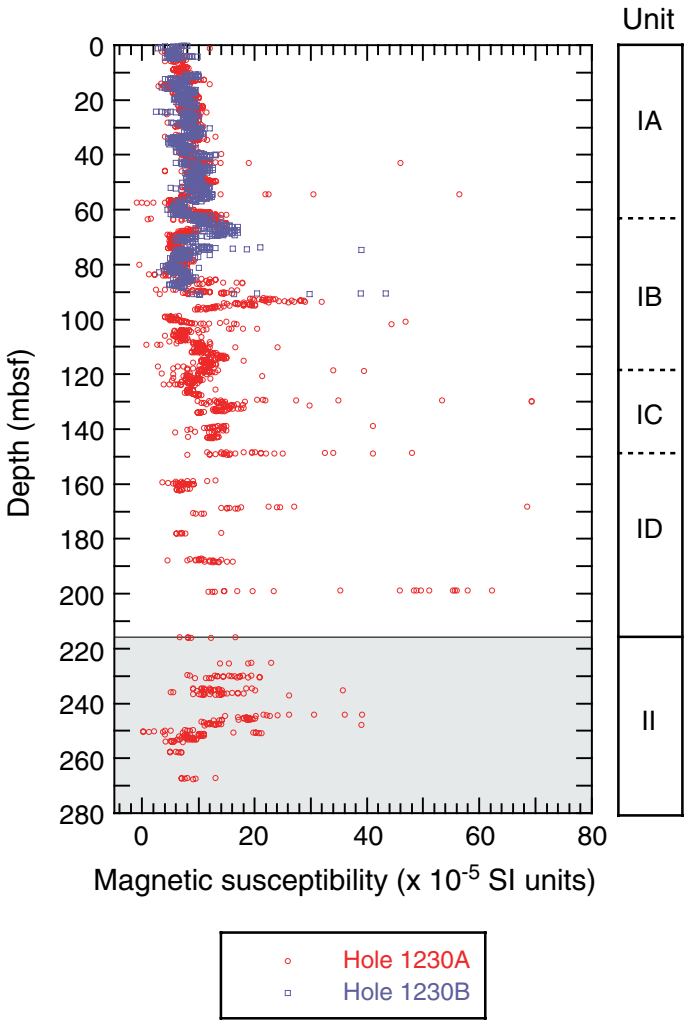

Figure F17. Magnetic intensity and susceptibility in Hole 1230A. Open squares = NRM intensity, solid squares = intensity after 20-mT AF demagnetization.

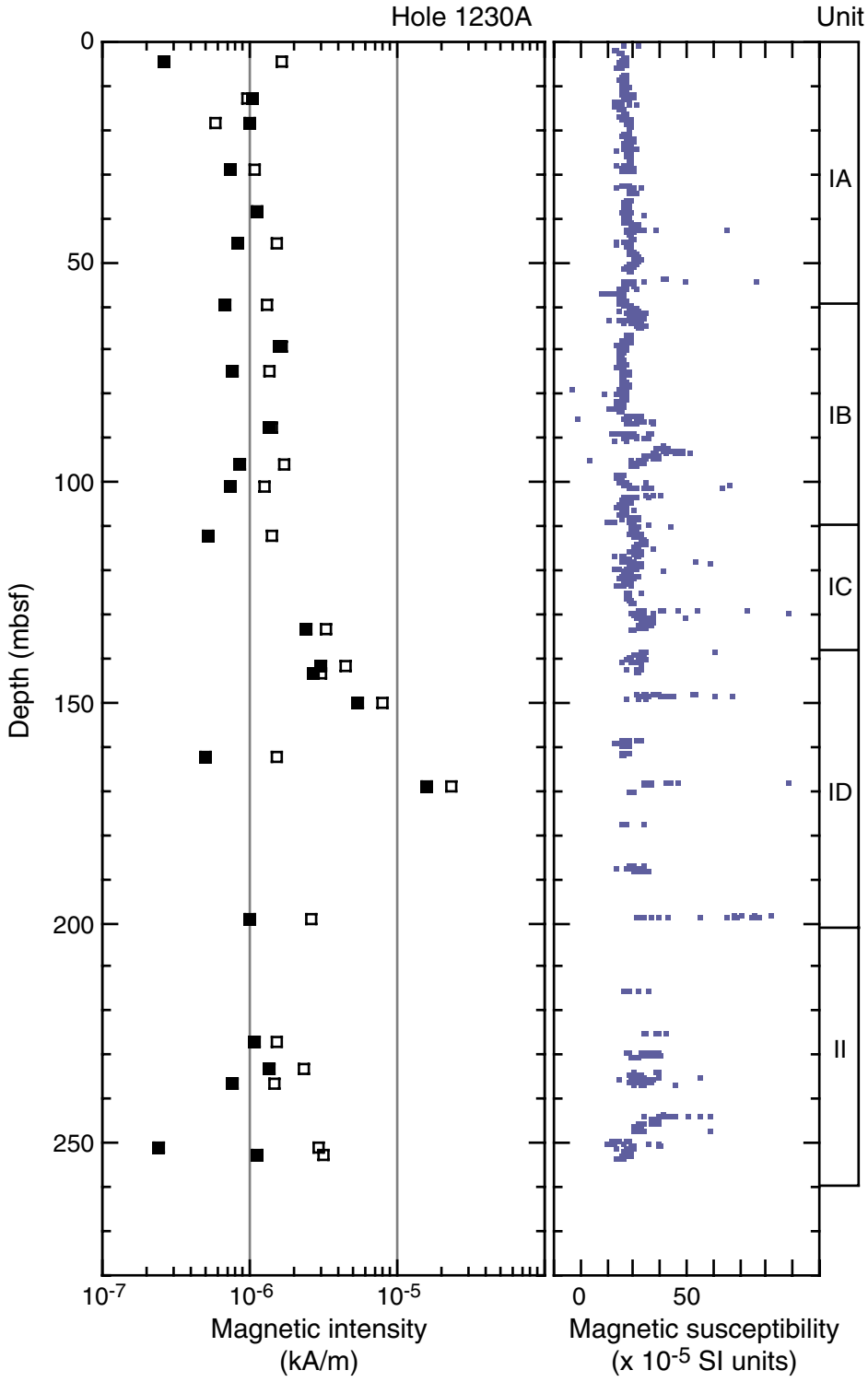

Figure F18. Principal component analysis of natural remanent magnetization (NRM) of Sample 201-1230A-17H-3, 89–91 cm, including equal area projection of directions of magnetization during demagnetization, intensity of magnetization plotted vs. demagnetization, and vector component diagrams showing projection of magnetic vector's endpoints on horizontal and vertical planes.

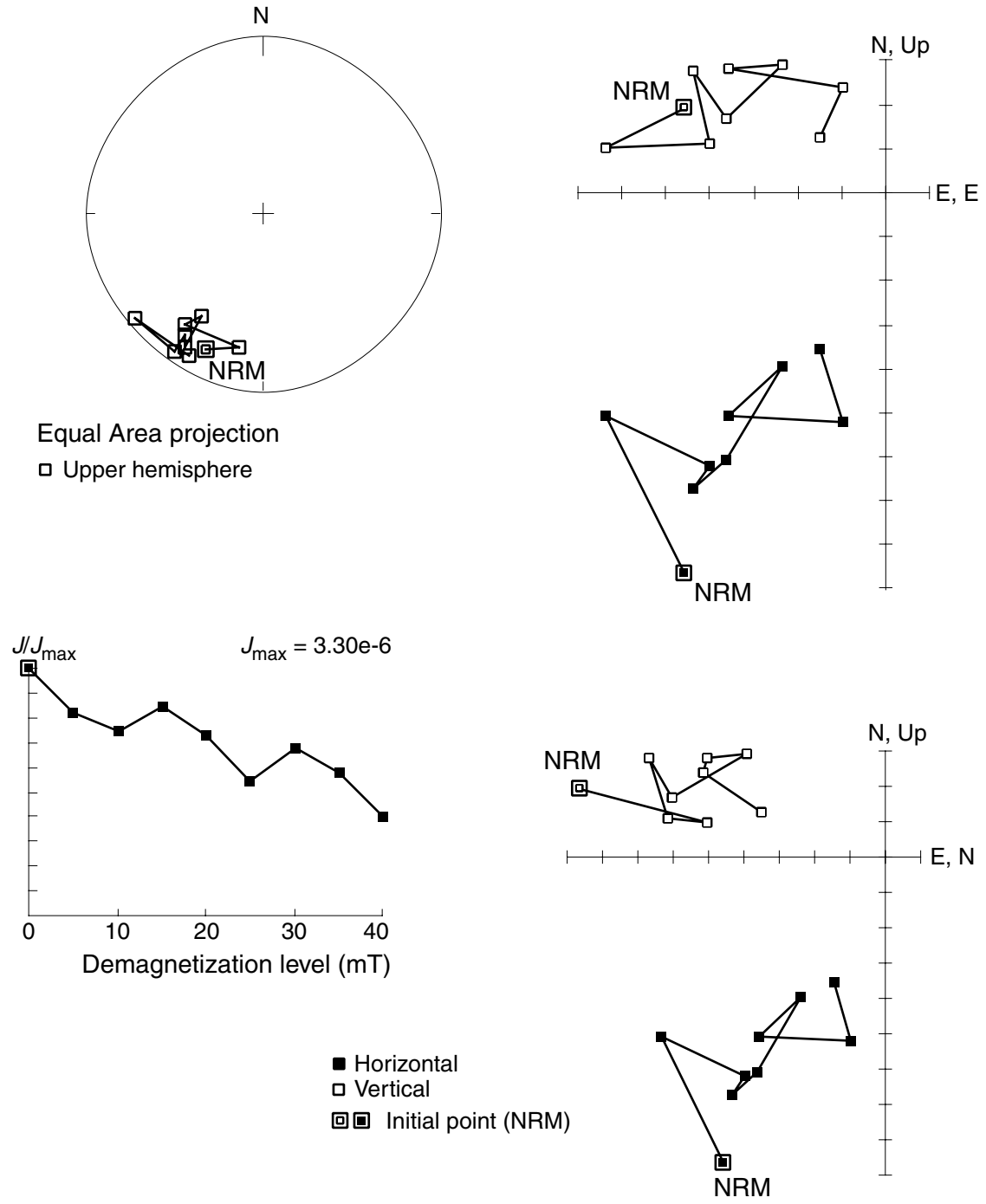

Figure F19. Principal component analysis of natural remanent magnetization (NRM) of Sample 201-1230A-19H-2, 10–12 cm, including equal area projection of directions of magnetization during demagnetization, intensity of magnetization plotted vs. demagnetization, and vector component diagrams showing projection of magnetic vector's endpoints on horizontal and vertical planes.

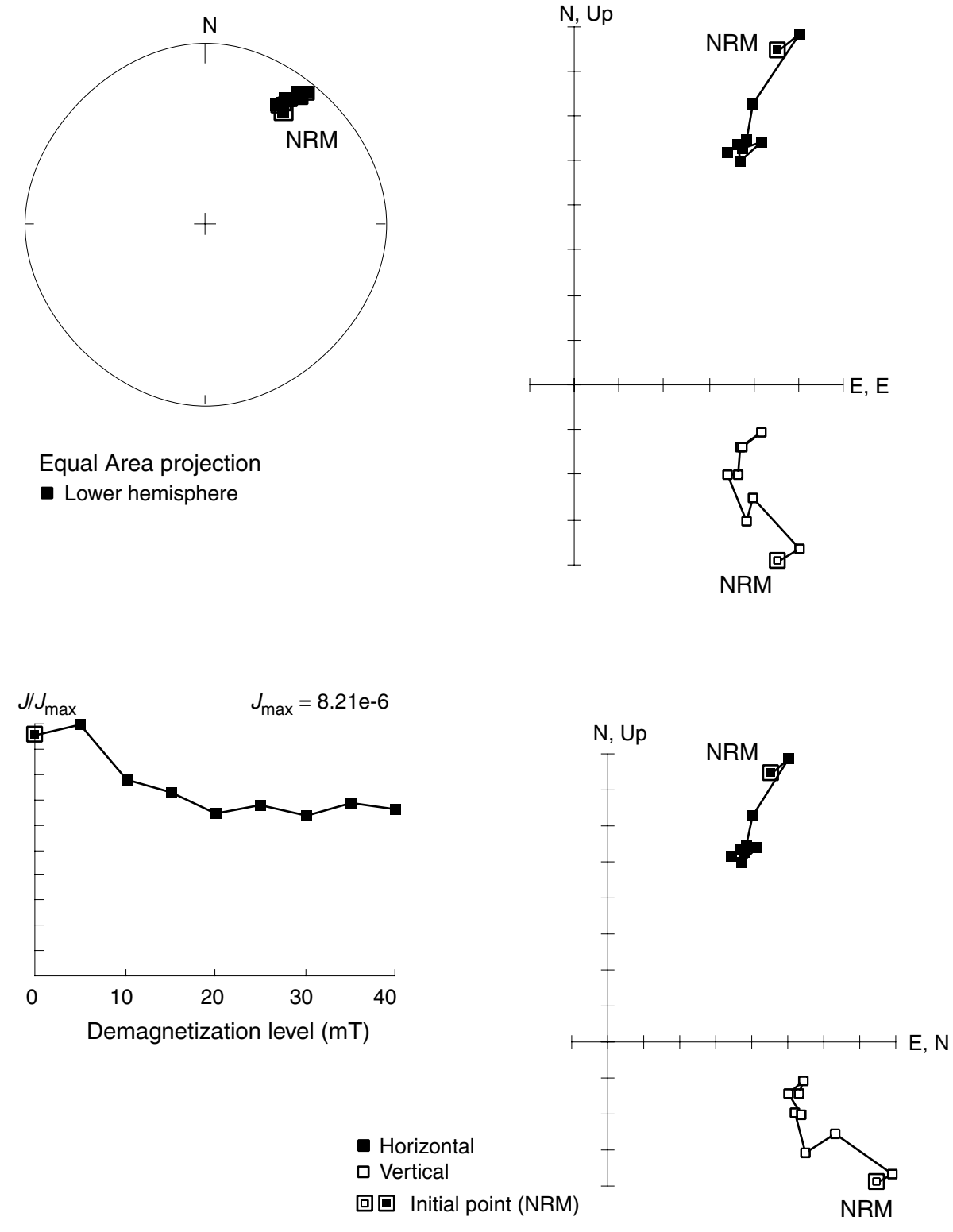

Figure F20. Principal component analysis of natural remanent magnetization (NRM) of Sample 201-1230A-22H-1, 60–62 cm including equal area projection of directions of magnetization during demagnetization, intensity of magnetization plotted vs. demagnetization, and vector component diagrams showing projection of magnetic vector's endpoints on horizontal and vertical planes.

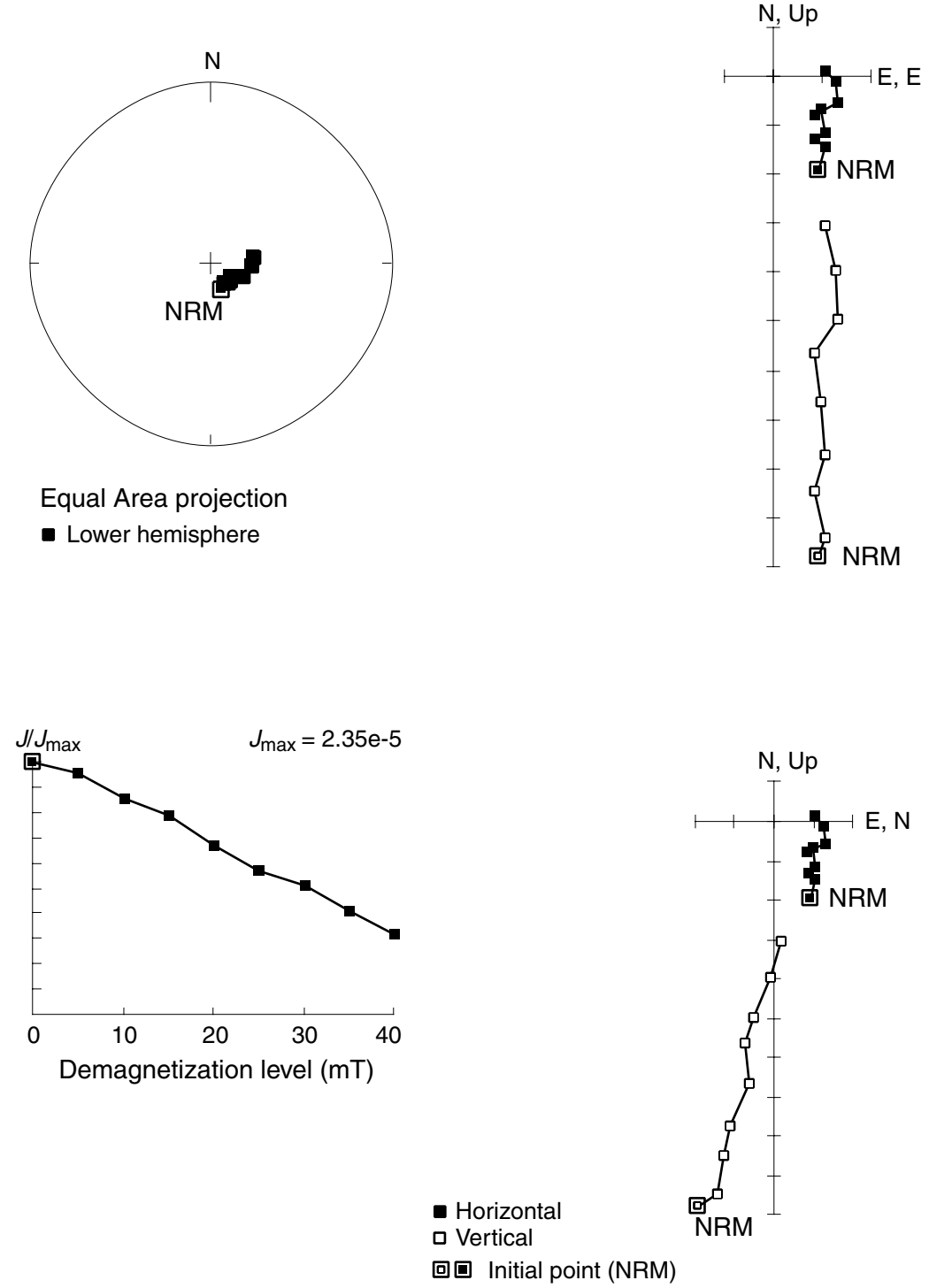

Figure F21. A. Bulk density from multisensor track gamma ray attenuation (GRA)-based measurements. The variability and occurrence of very low values (<1.2 g/cm^3) reflect severe degassing artifacts and recovery disturbance. **B.** Downhole comparison of GRA, moisture and density (MAD), and wireline bulk density measurements.

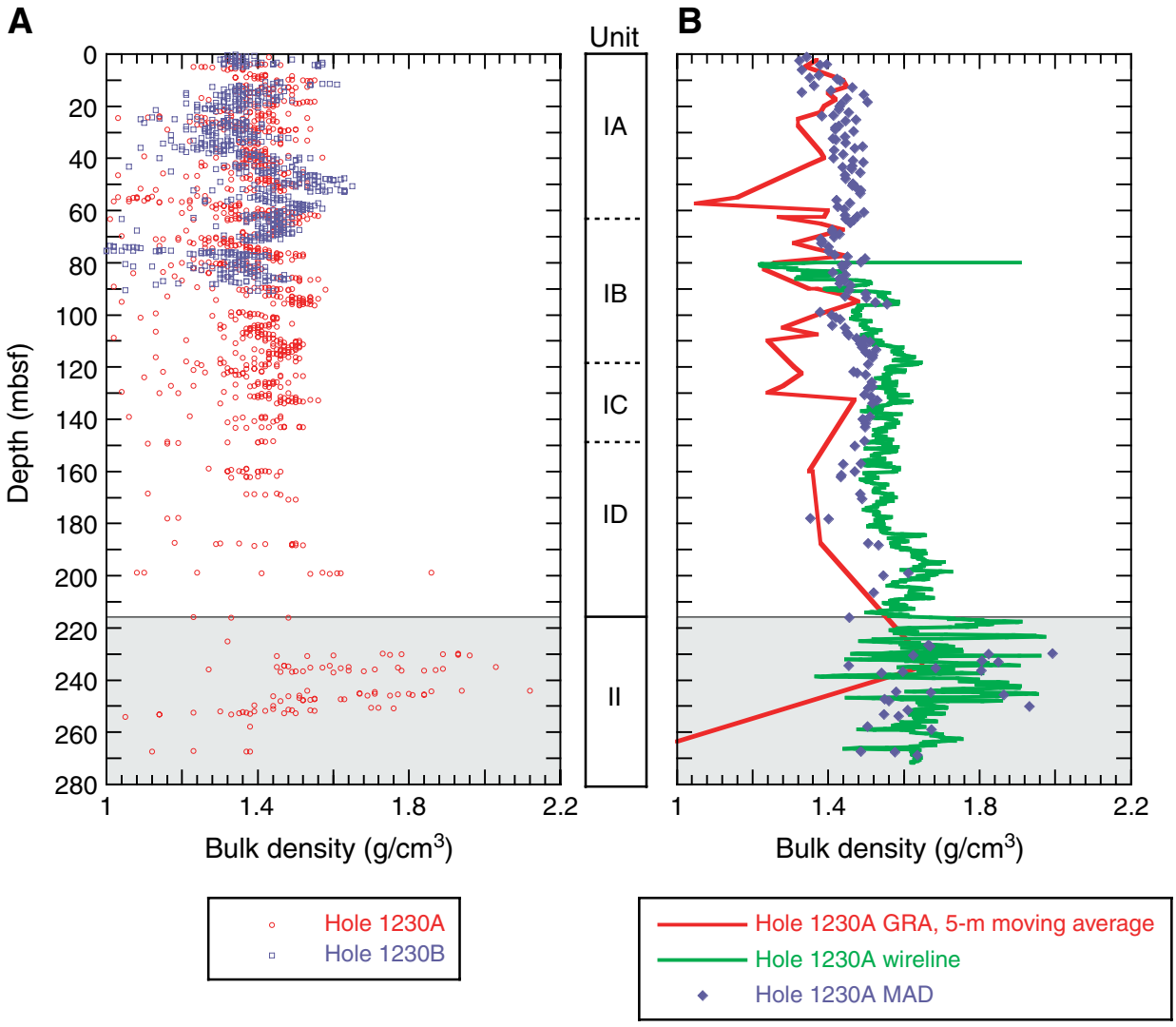

Figure F22. Mass/volume-based moisture and density (MAD) measurements. **A.** Bulk density. **B.** Grain density. **C.** Porosity.

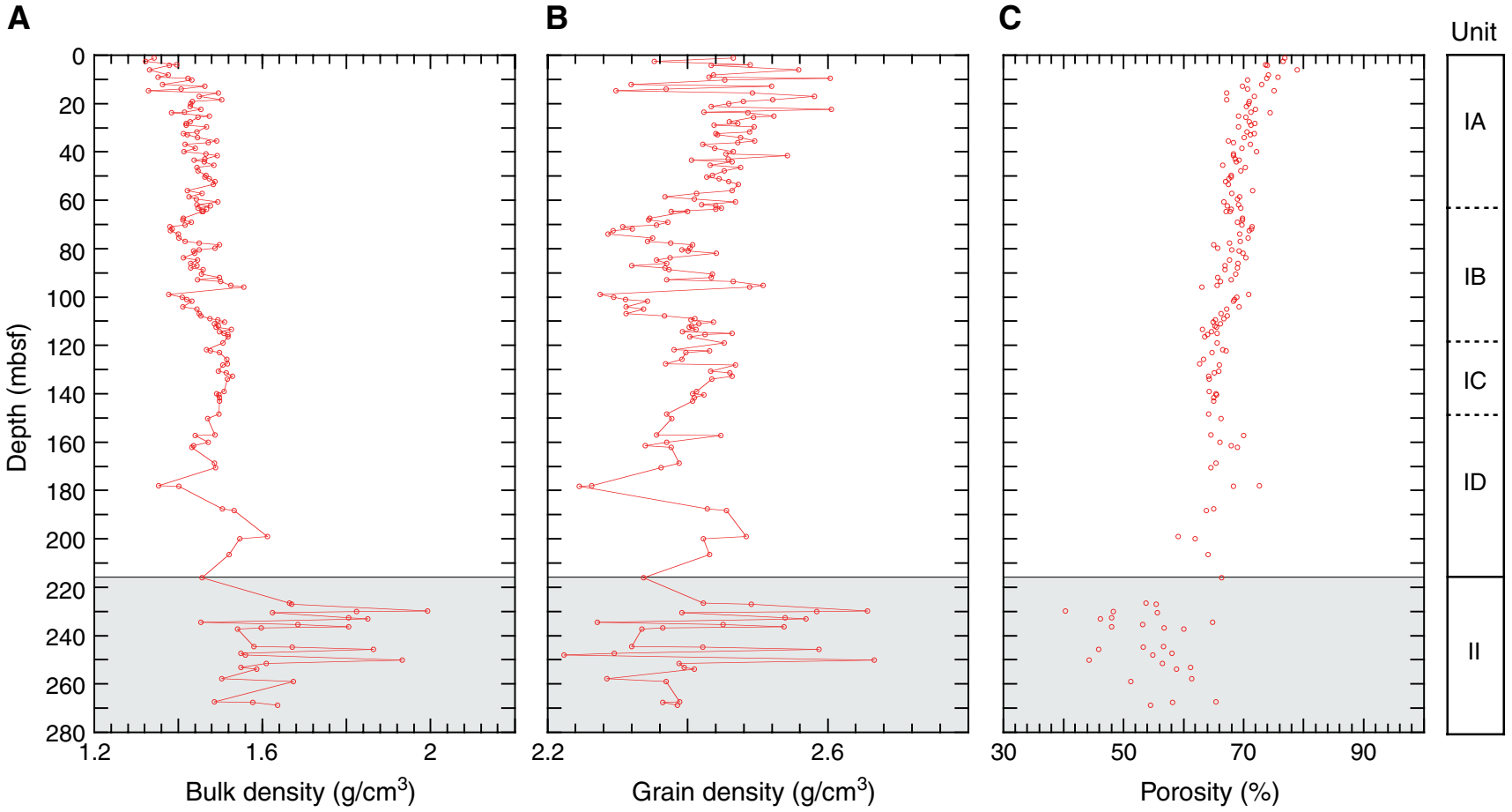

Figure F23. *P*-wave velocity profiles obtained by the MST *P*-wave logger (PWL) (0–11 mbsf only), PWS3, and wireline sonic measurements. At 222–225 mbsf, the sonic velocity increase corresponds to an interval of intense carbonate cementation.

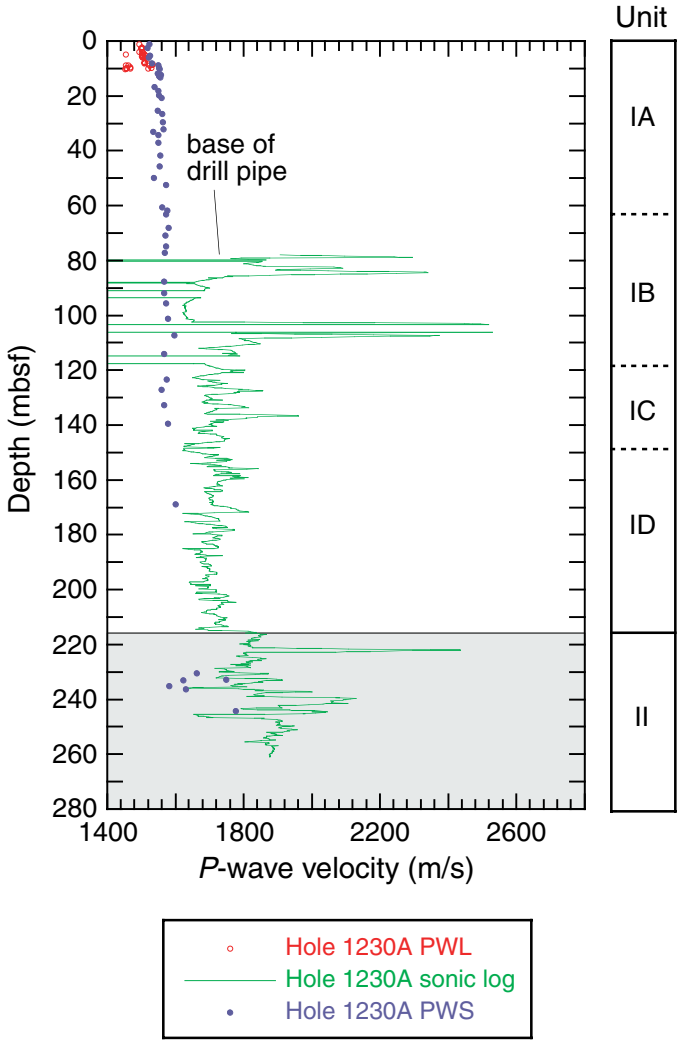

Figure F24. Natural gamma radiation (NGR) measured on the multisensor track (Holes 1230A and 1230B) and with the triple combination wireline tool (Hole 1230A).

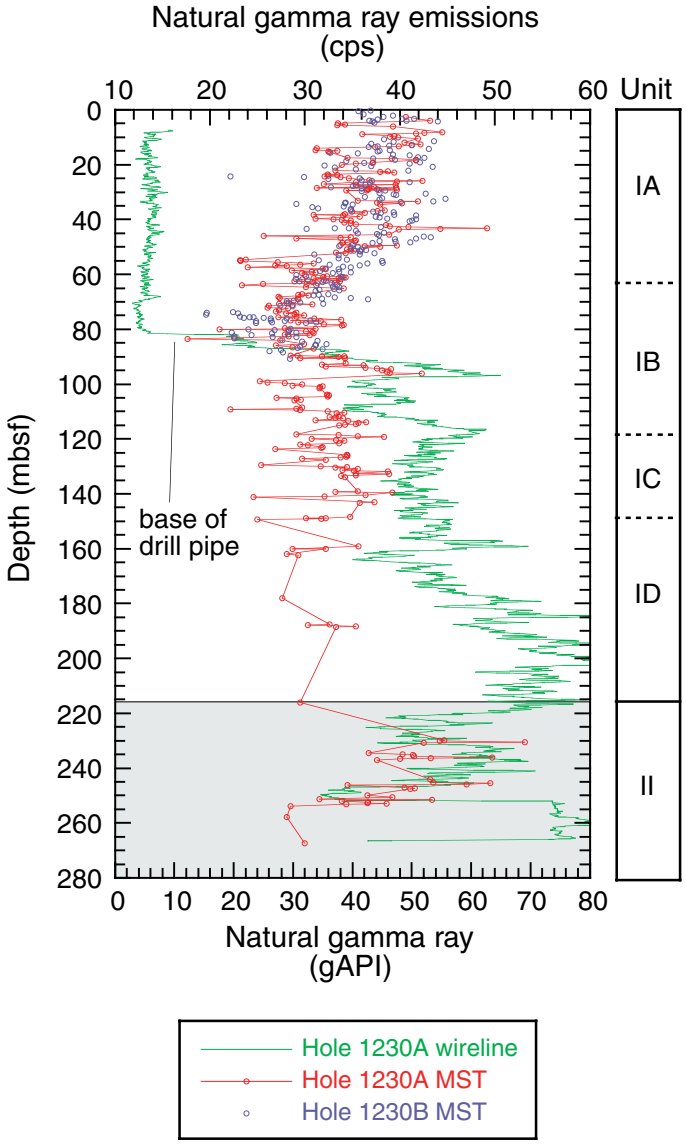

Figure F25. A. Thermal conductivity measurements (needle-probe method) show near-constant values through Unit I, with a sharp increase across the slope apron-wedge sediment interface at 216 mbsf. The value at 206 mbsf (0.68 W/m/°C) is an outlier. It probably represents measurement in an unfilled core liner. **B.** Overlapping mean-normalized thermal conductivity and bulk density profiles illustrate that water content is the primary determinant of downhole thermal conductivity variation.

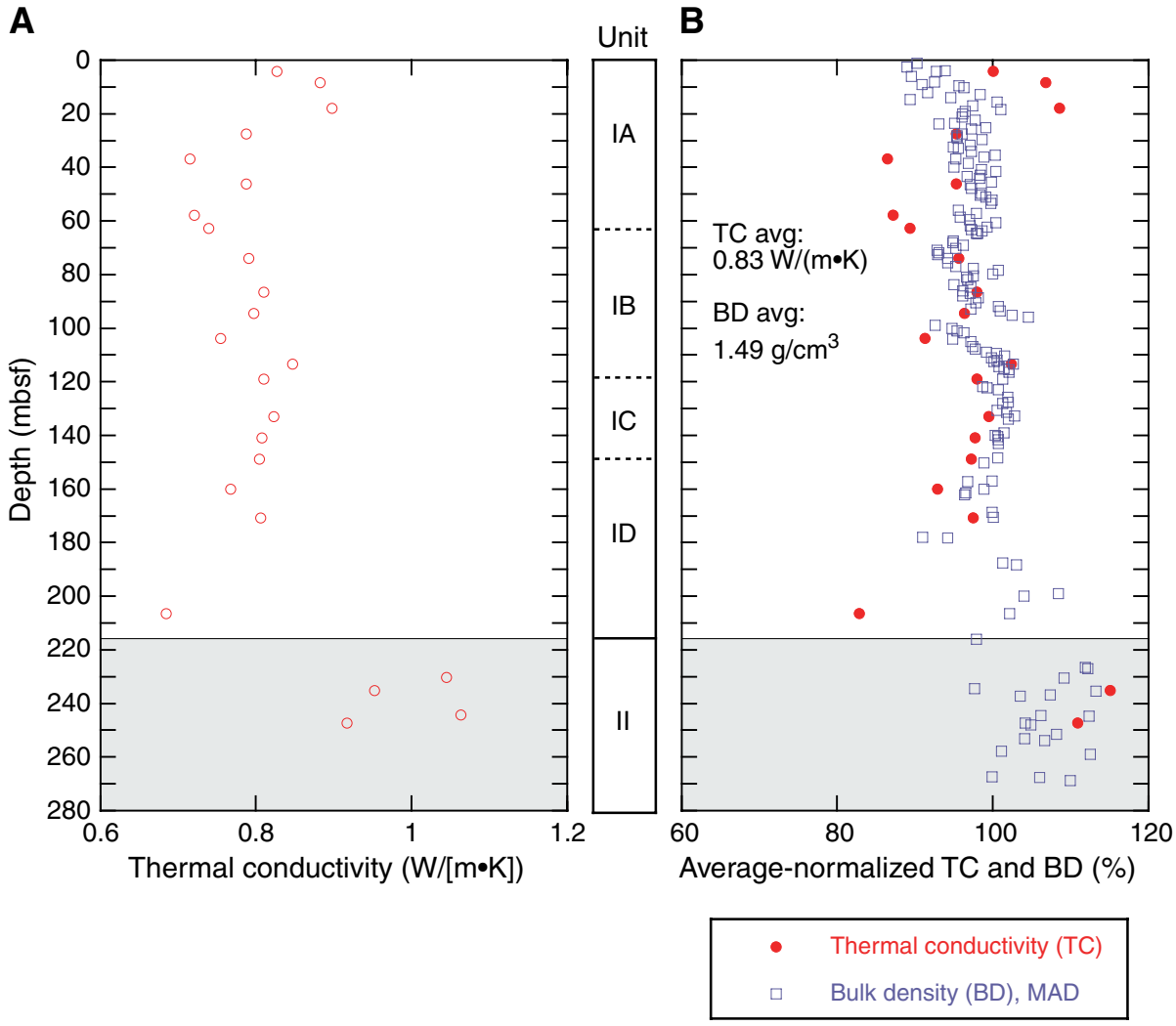

Figure F26. Temperature records for the three successful DVTP deployments at Site 1230 at (**A**) 33.3 mbsf, (**B**) 100 mbsf, and (**C**) 254.6 mbsf.

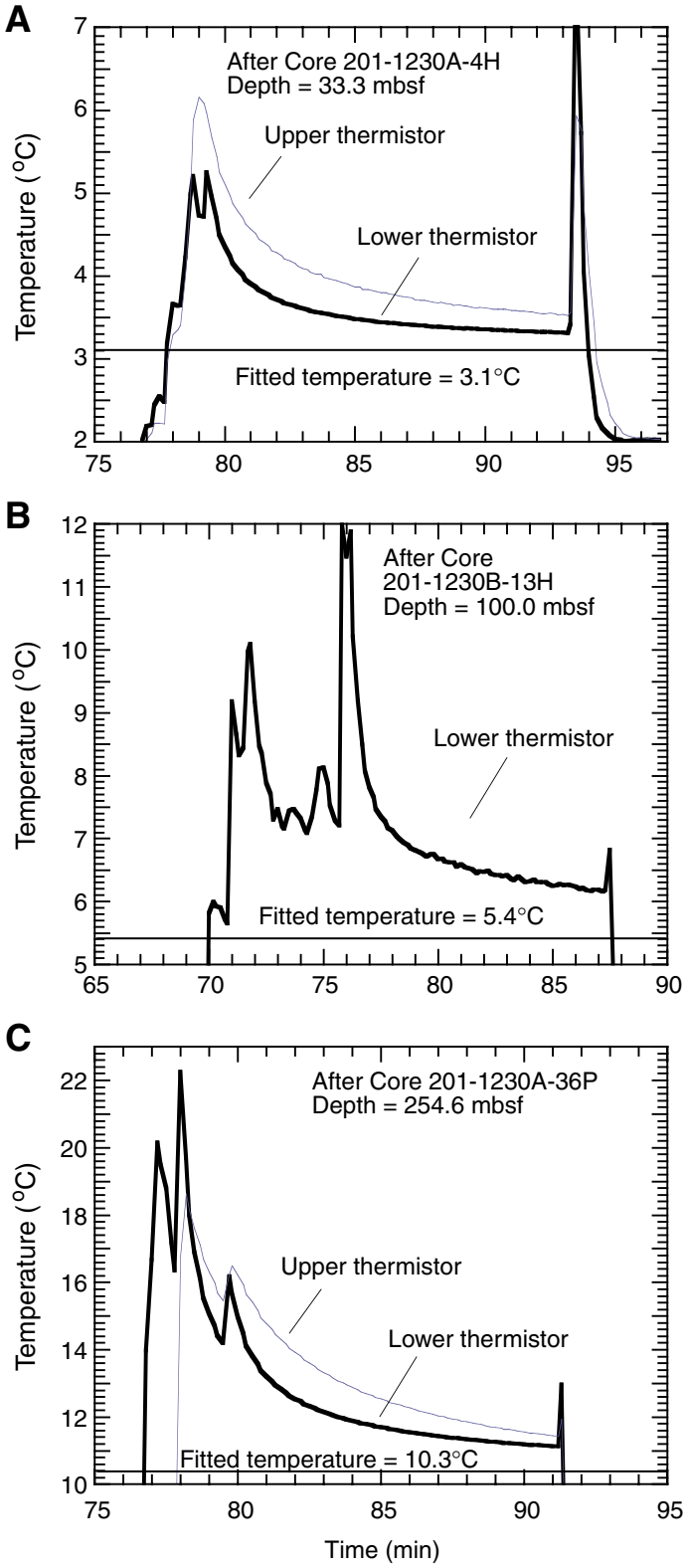

Figure F27. Temperatures measured in Holes 1230A and 1230B plotted vs. depth together with several model profiles. **A.** Best-fit linear profile. **B.** Steady-state conductive profile calculated using measured thermal conductivities from Hole 1230A and uniform heat flow. A parabolic least-squares fit is shown for comparison. **C.** Steady-state fluid flow with fixed temperature at depth and the flow velocities shown.

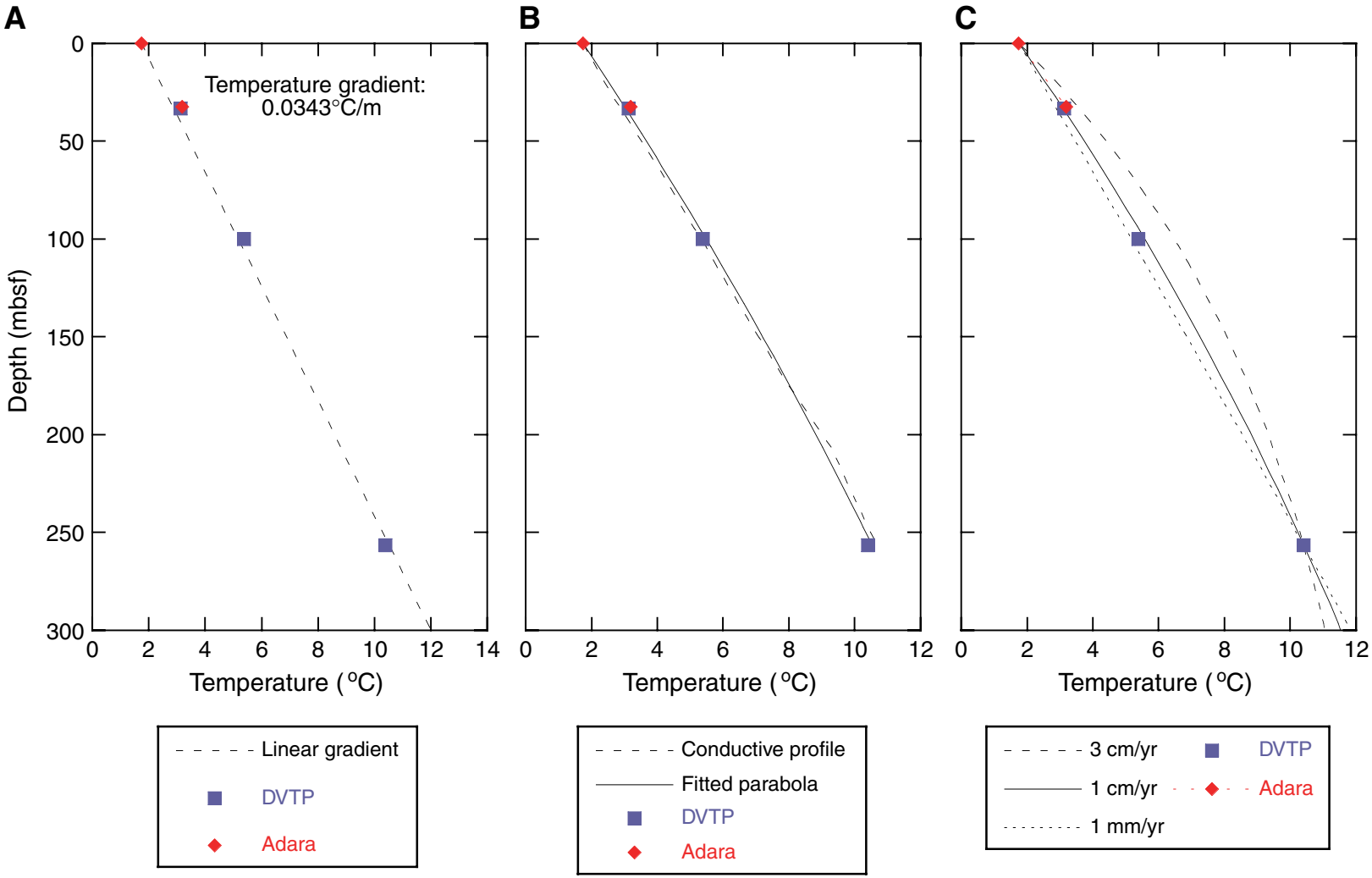

Figure F28. Pressure measured in Hole 1230B during the DVTP-P deployment after Core 201-1230B-14H. BOH = bottom of hole.

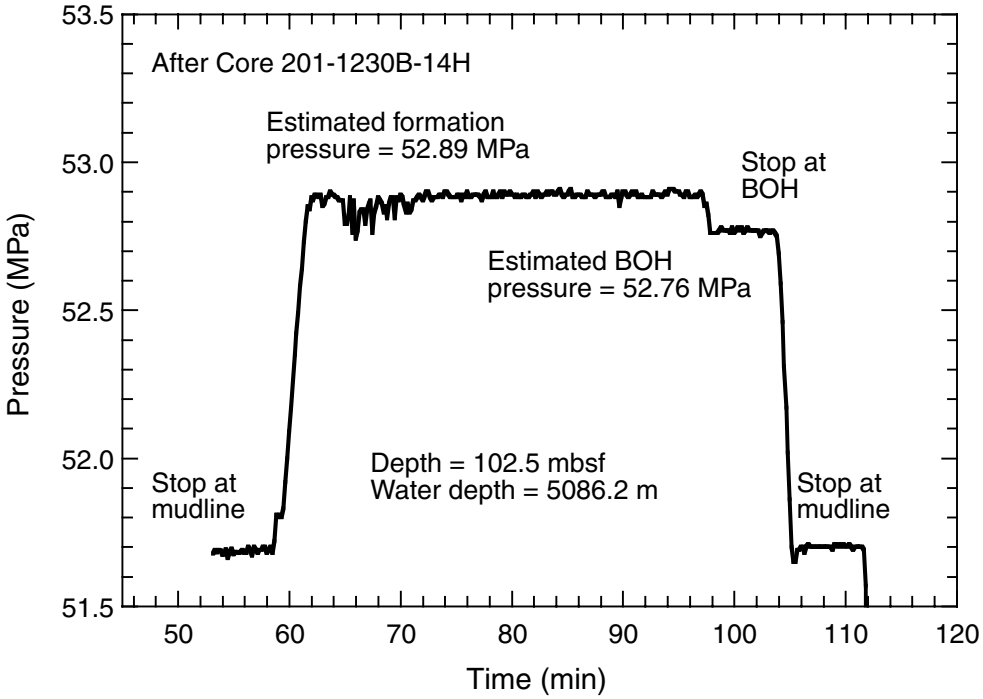

Figure F29. Main logs recorded in Hole 1230A. **A.** The hole diameter is measured by the caliper arm of the density sonde. **B.** The gamma ray log is a measure of the natural radioactivity of the formation. **C.** Concentrations of potassium, thorium, and uranium derived from the gamma ray counts. **D.** Resistivity measured by the Phasor Dual Induction Tool with three depths of investigation. **E.** Preliminary compressional (V_P) and shear (V_S) sonic velocity. These data will be reprocessed postcruise. **F.** Density log (red line) compared with density measurements made on core samples (shaded circles) (see **"Density and Porosity,"** p. 26, in "Physical Properties"). **G.** Porosity log for the two receivers of the APS sonde compared with porosity measurements made on core samples (shaded circles) (see **"Density and Porosity,"** p. 26, in "Physical Properties"). HNGS = Hostile Environment Natural Gamma Ray Sonde. SGT = Scintillation Gamma Ray Tool.

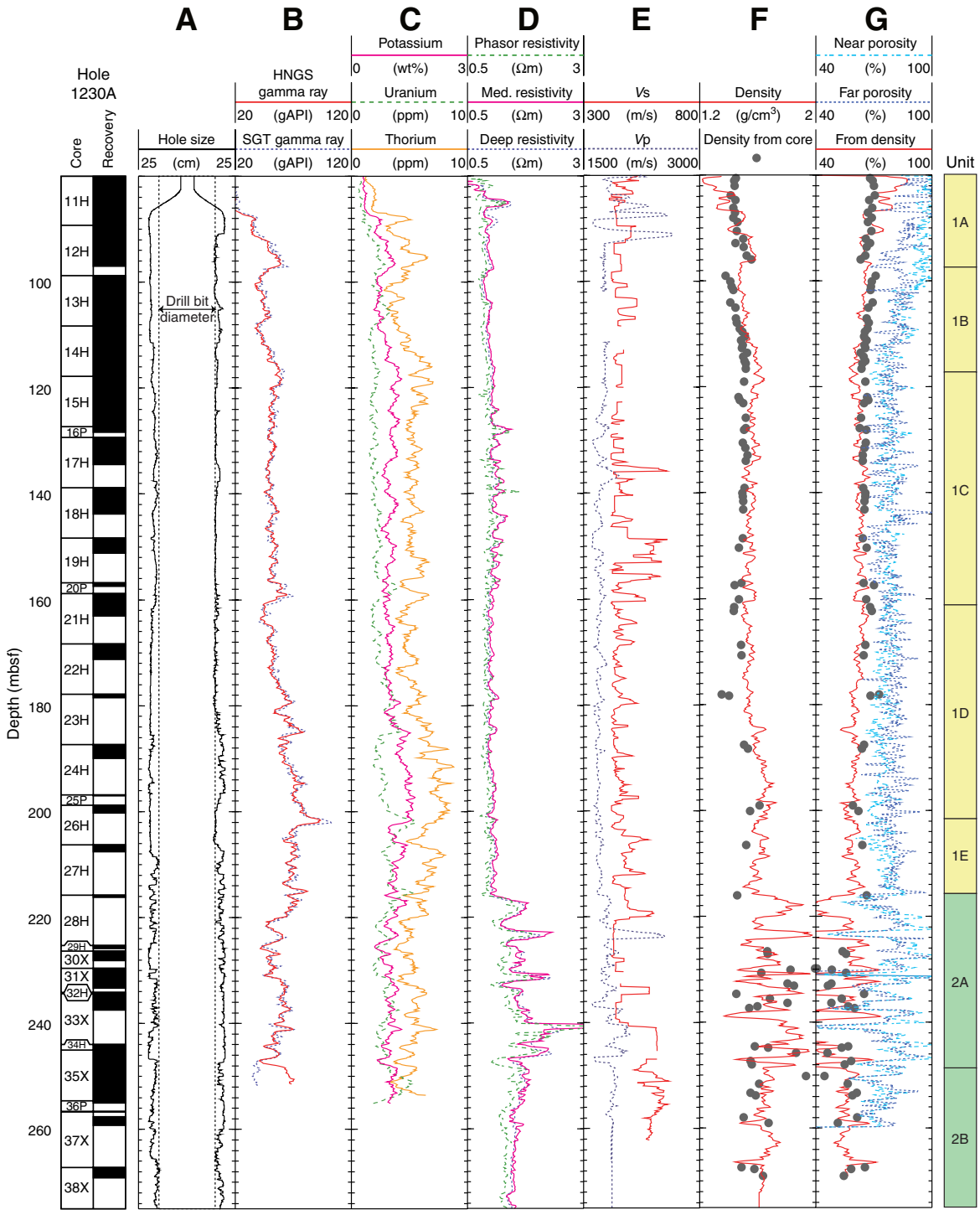

Figure F30. A–E. Formation MicroScanner images recorded in Hole 1230B at different intervals. Bright features indicate resistive layers, such as cemented intervals, or possibly hydrate-rich formations. The orientation of the tool and of the images is derived from a three-axis magnetometer (see **"Downhole Logging,"** p. 53, in the "Explanatory Notes" chapter).

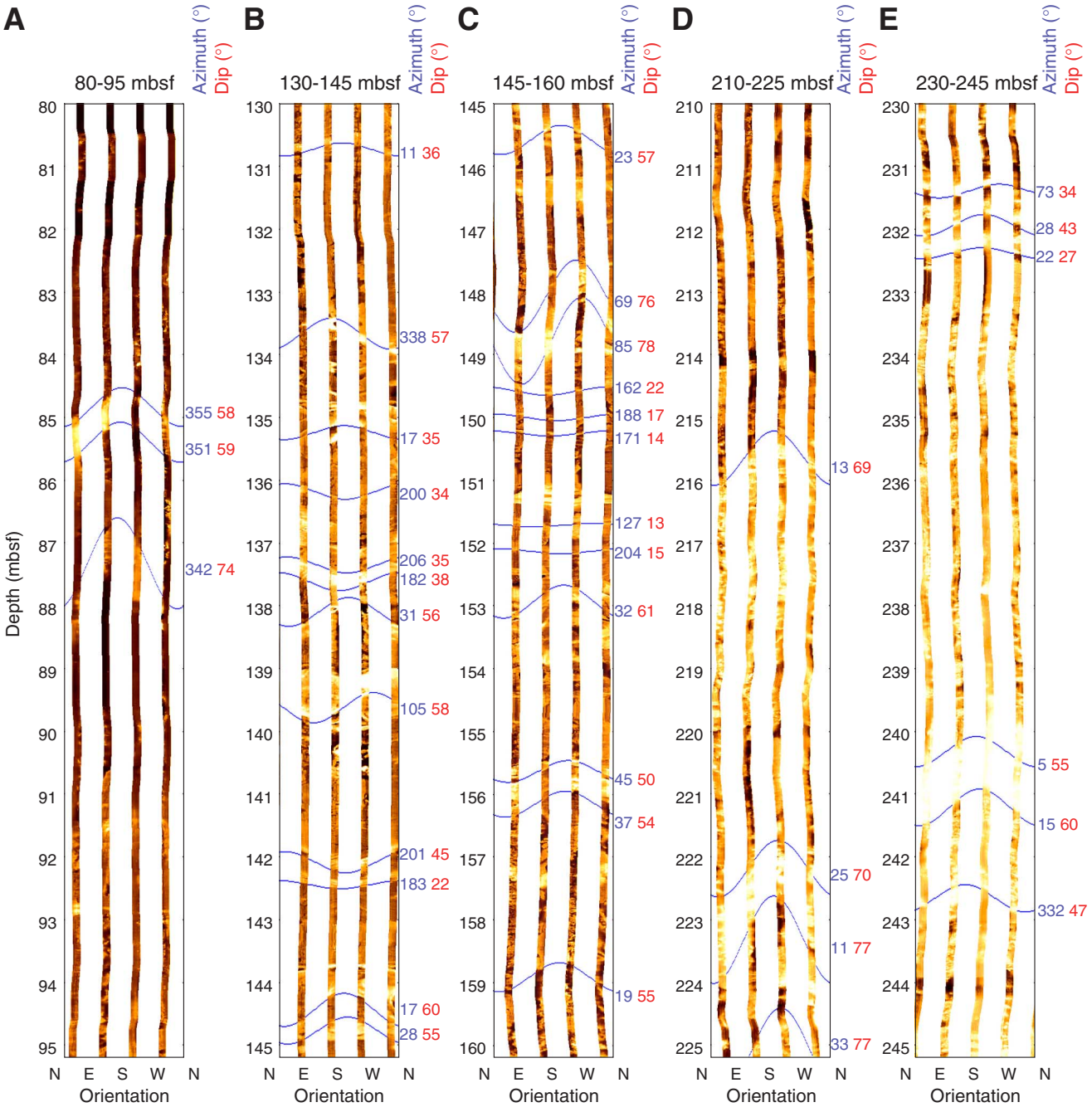

Figure F31. Temperature log recorded in Hole 1230A. Temperature data were recorded continuously during the two passes of the triple combo tool string.

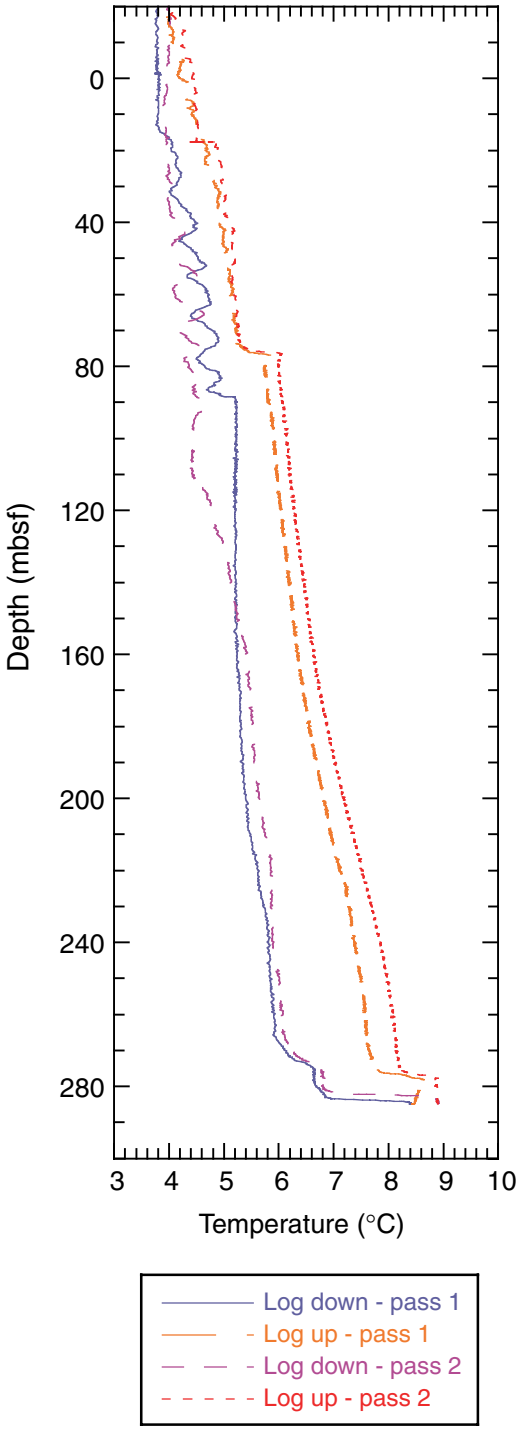

Figure F32. Comparison of temperatures recorded by the IR camera in (**A**) Core 201-1230A-6H without indications for gas hydrate and (**B**) Core 201-1230A-19H with intervals of gas hydrate (Table T14, p. 106). Black solid line = measured temperature, red dotted line = average temperature. Note that the average temperature of Core 201-1230A-6H is lower than that of Core 201-1230A-19H. This is because the latter core comes from greater sediment depth and contains gas voids, which result in positive temperature excursions. V = void, H = interval inferred to contain hydrate.

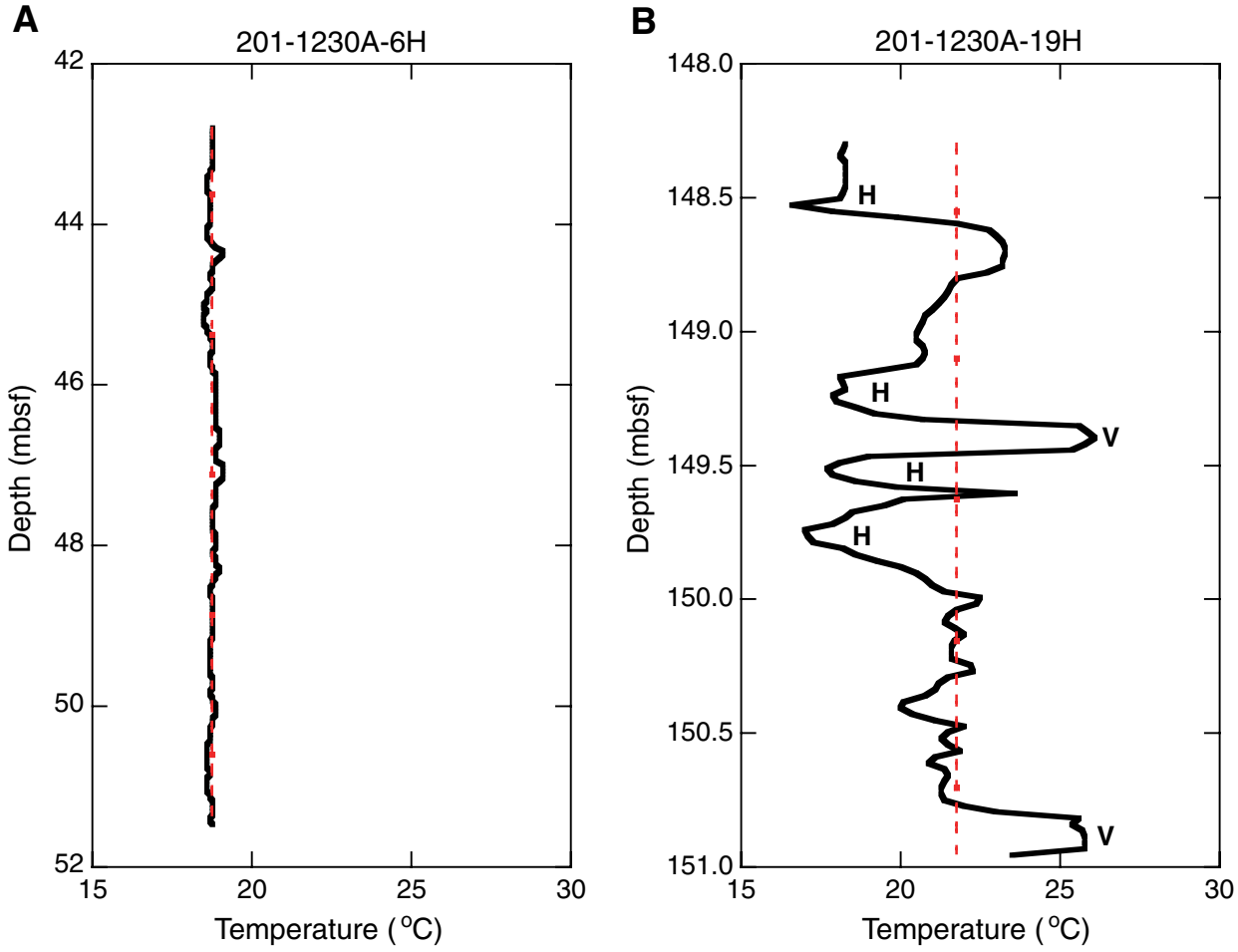

Figure F33. Photographs of vein-type gas hydrate that fills vertically running fractures (Section 201-1230B-12H-2). **A.** Core section immediately after splitting demonstrating the vertical to subvertical orientation of a ~3-mm-thick gas hydrate vein. **B.** White gas hydrate veins separated by dark gray sediment after splitting of the core. Sample was rotated out of its original orientation to show texture. Height of image is 7 cm.

A

B

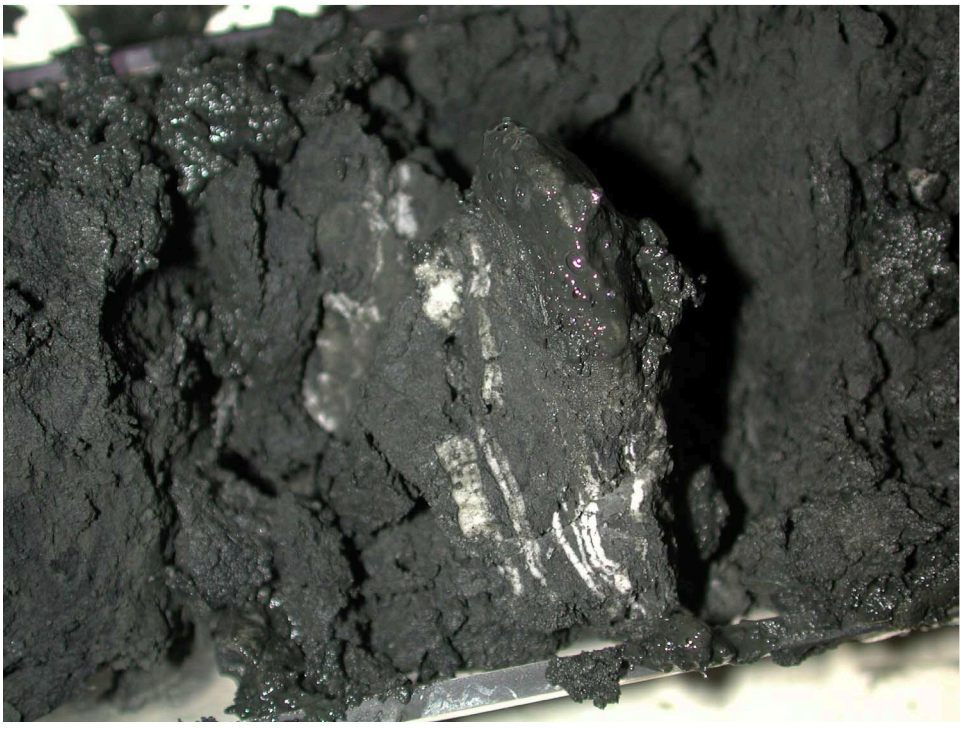

Figure F34. Images illustrating core disturbances believed to be associated with methane escape, possibly related to gas hydrate dissociation during core recovery. **A.** Sediment showing splitting parallel to bedding over a zone of 23 cm (37–60 cm). Note that intensity inferred by spacing decreases away from the center of this zone. **B.** Splitting and crumbling of sediment adjacent to a void. **C.** Void with crumbling and splitting of sediment confined to a 15-cm sediment interval. **D.** Multiple occurrences of disrupted fabrics (as in A–C) over a 52-cm interval.

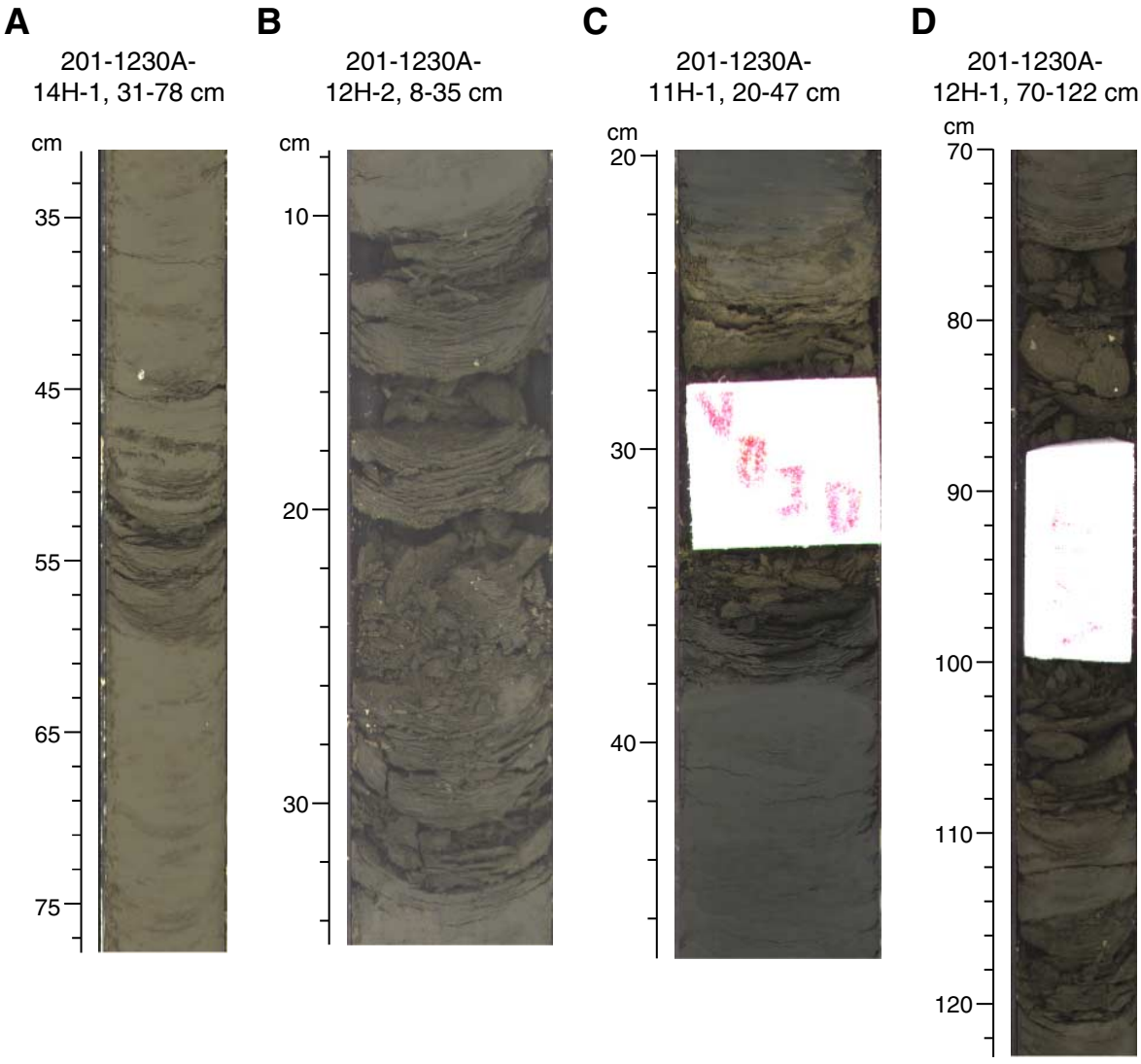

Figure F35. Interstitial water chloride concentrations for Site 1230. Low chloride concentrations at ~80 and 150 mbsf coincide with the two intervals from which solid hydrate samples were recovered. Arrows = location of hydrate samples.

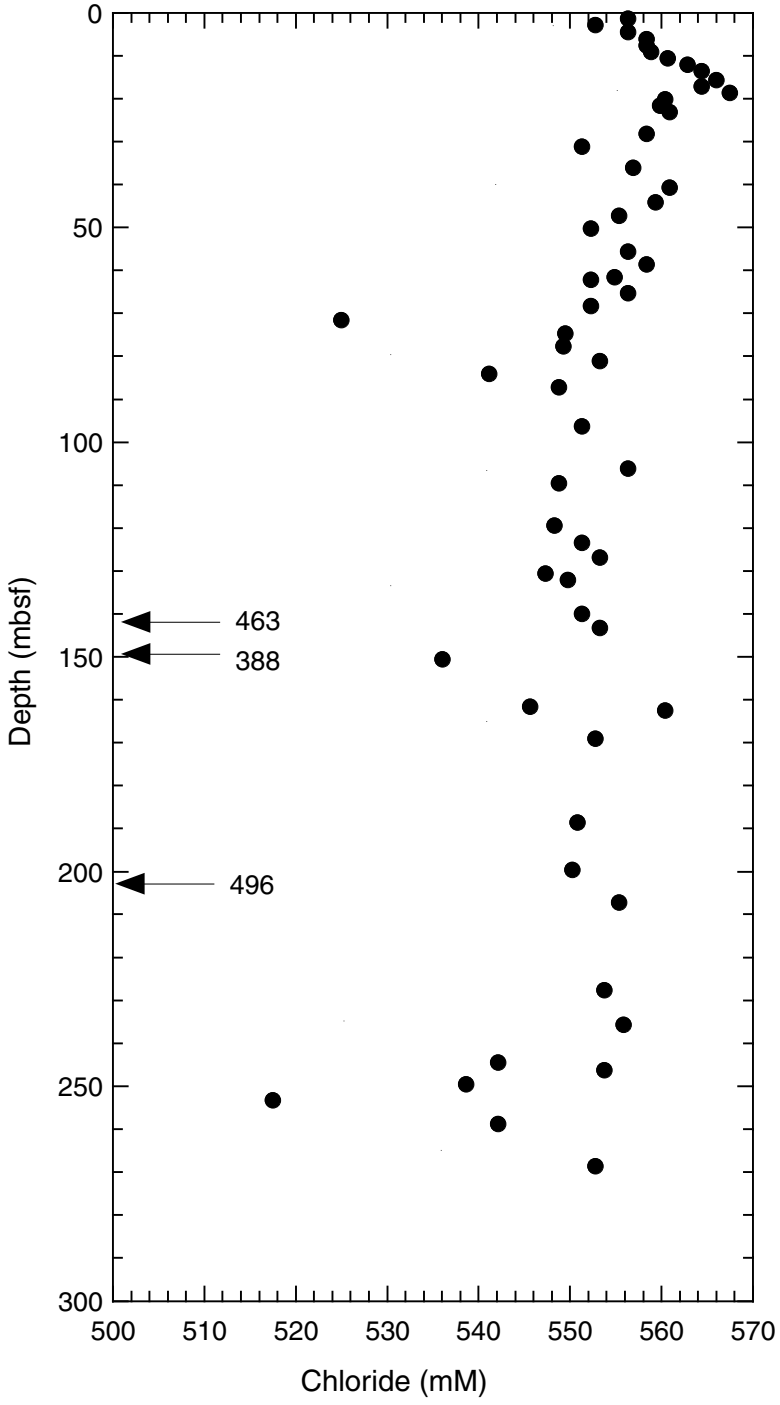

Figure F36. Identification of intervals where logging data show that gas hydrate may be present. Resistivity and velocity increase with increasing hydrate concentration, whereas waveform amplitude decreases. The density log helps to identify resistivity spikes that could be created by factors other than gas hydrate within the hydrate zone.

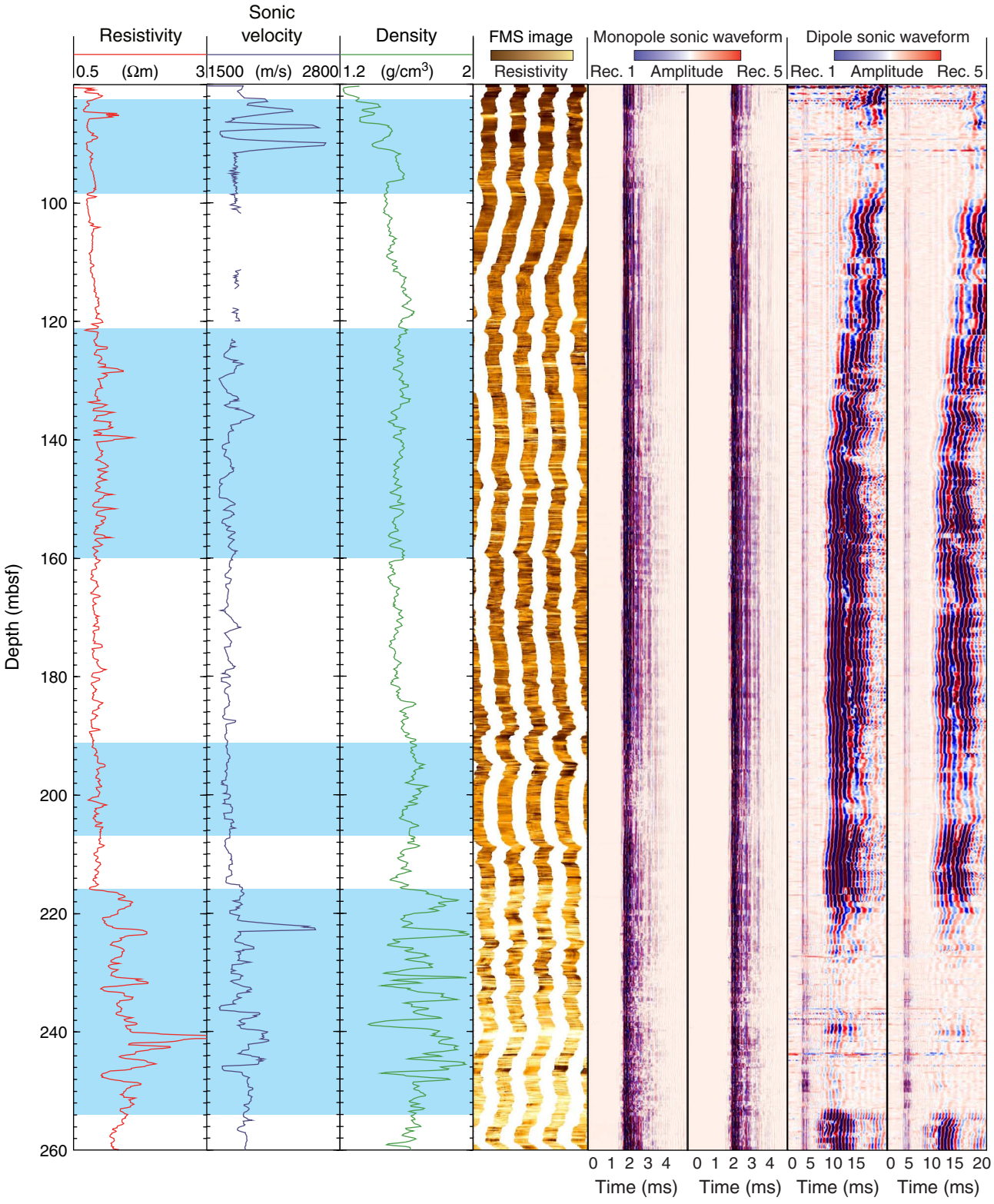

Figure F37. Stratigraphic comparison of depths with evidence for gas hydrate (marked with the arrows), core disruption, core liner temperature, and wireline logs for Hole 1230A. **A.** Core disturbance areas. From left to right, the black squares indicate a relative increase in core disturbance. **B.** Core temperature profile measured on the catwalk, based on IR thermal imaging of the core liners. **C.** Wireline resistivity. **D.** Wireline sonic velocity.

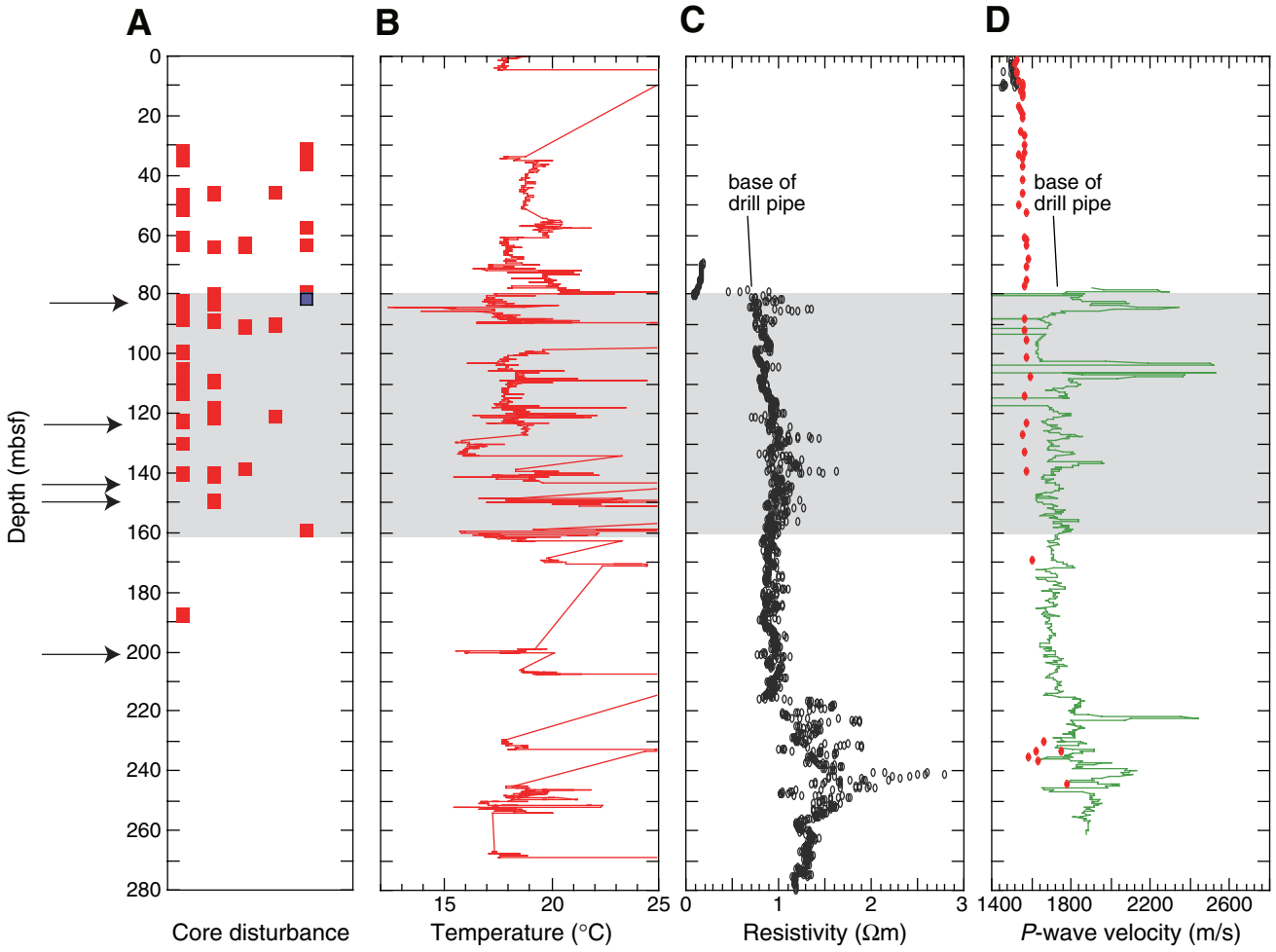

Table T1. Coring summary, Site 1230. (Continued on next two pages.)

Hole 1230A
Latitude: 9°6.7525′S
Longitude: 80°35.0100′W
Time on site (hr): 200.75 (0030 hr, 11 Mar–0845 hr, 19 Mar 2002)
Time on hole (hr): 142.08 (0030 hr, 11 Mar–2235 hr, 16 Mar 2002)
Distance between rig floor and sea level (m): 11.5
Water depth (drill pipe measurement from sea level, m): 5086.2
Total depth (drill pipe measurement from rig floor, mbrf): 5376.0
Total penetration (meters below seafloor, mbsf): 278.3
Total length of cored section (m): 277.3
Total length of drilled intervals (m): 1.0
Total core recovered (m): 187.33 m
Core recovery (%): 67.6
Total number of cores: 39
Total number of drilled intervals: 1

Hole 1230B
Latitude: 9°6.7415′S
Longitude: 80°35.0112′W
Time on hole (hr): 34.00 (2235 hr, 16 Mar–0835 hr, 18 Mar 2002)
Seafloor (drill pipe measurement from rig floor, mbrf): 5097.1
Distance between rig floor and sea level (m): 11.6
Water depth (drill pipe measurement from sea level, m): 5085.5
Total depth (drill pipe measurement from rig floor, mbrf): 5202.1
Total penetration (meters below seafloor, mbsf): 105.0
Total length of cored section (m): 102.0
Total length of drilled intervals (m): 3.0
Total core recovered (m): 98.33
Core recovery (%): 96.4
Total number of cores: 14
Total number of drilled intervals: 2

Hole 1230C
Latitude: 9°6.7369′S
Longitude: 80°35.0111′W
Time on hole (hr): 1.92 (0835 hr, 18 Mar–1030 hr, 18 Mar 2002)
Seafloor (drill pipe measurement from rig floor, mbrf): 5098.0
Distance between rig floor and sea level (m): 11.6
Water depth (drill pipe measurement from sea level, m): 5086.4
Total depth (drill pipe measurement from rig floor, mbrf): 5112.0
Total penetration (meters below seafloor, mbsf): 14.0
Total length of cored section (m): 14.0
Total core recovered (m): 14.42 m
Core recovery (%): 103.0
Total number of cores: 2

Hole 1230D
Latitude: 9°6.7338′S
Longitude: 80°35.0125′W
Time on hole (hr): 3.00 (1030 hr, 18 Mar–1300 hr, 18 Mar 2002)
Seafloor (drill pipe measurement from rig floor, mbrf): 5098.5
Distance between rig floor and sea level (m): 11.6
Water depth (drill pipe measurement from sea level, m): 5086.9
Total depth (drill pipe measurement from rig floor, mbrf): 5112.0
Total penetration (meters below seafloor, mbsf): 13.5
Total length of cored section (m): 13.5
Total core recovered (m): 14.22
Core recovery (%): 105.3
Total number of cores: 2

Hole 1230E
Latitude: 9°6.7265′S
Longitude: 80°35.0095′W
Time on hole (hr): 19.75 (1300 hr, 18 Mar–0845 hr, 19 Mar 2002)
Seafloor (drill pipe measurement from rig floor, mbrf): 5098.5
Distance between rig floor and sea level (m): 11.6
Water depth (drill pipe measurement from sea level, m): 5086.9
Total depth (drill pipe measurement from rig floor, mbrf): 5134.5
Total penetration (meters below seafloor, mbsf): 36.0
Total length of cored section (m): 34.5
Total length of drilled intervals (m): 1.5
Total core recovered (m): 34.47
Core recovery (%): 102.9
Total number of cores: 5
Total number of drilled intervals: 1

Table T1 (continued).

Core	Date (Mar 2002)	Local time (hr)	Depth (mbsf) Top	Depth (mbsf) Bottom	Length (m) Cored	Length (m) Recovered	Recovery (%)
201-1230A-							
1H	11	1625	0.0	4.8	4.8	4.86	101.3
2H	11	1740	4.8	14.3	9.5	9.60	101.1
3H	11	1910	14.3	23.8	9.5	9.90	104.2
4H	11	2025	23.8	33.3	9.5	9.79	103.1
5H	11	2345	33.3	42.8	9.5	10.17	107.1
6H	12	0135	42.8	52.3	9.5	10.01	105.4
7P	12	0330	52.3	54.3	2.0	1.50	75.0
8H	12	0520	54.3	60.8	6.5	9.97	153.4
9H	12	0740	60.8	70.3	9.5	10.59	111.5
10H	12	1000	70.3	79.8	9.5	10.18	107.2
11H	12	1420	79.8	89.3	9.5	10.25	107.9
12H	12	1655	89.3	98.8	9.5	7.69	81.0
13H	12	1920	98.8	108.3	9.5	10.11	106.4
14H	12	2145	108.3	117.8	9.5	9.51	100.1
15H	13	0030	117.8	127.3	9.5	10.26	108.0
16P	13	0300	127.3	129.3	2.0	1.05	52.5
17H	13	0510	129.3	138.8	9.5	5.14	54.1
18H	13	0710	138.8	148.3	9.5	5.00	52.6
19H	13	1115	148.3	156.8	8.5	2.91	34.2
20P	13	1510	156.8	158.8	2.0	0.65	32.5
21H	13	1715	158.8	168.3	9.5	4.20	44.2
22H	13	1920	168.3	177.8	9.5	2.95	31.1
23H	13	2250	177.8	187.3	9.5	0.67	7.1
24H	14	0045	187.3	196.8	9.5	2.63	27.7
25P	14	0405	196.8	198.8	2.0	0.18	9.0
26H	14	0545	198.8	206.3	7.5	1.49	19.9
27H	14	0750	206.3	215.8	9.5	1.25	13.2
28H	14	1010	215.8	225.3	9.5	0.36	3.8
29H	14	1355	225.3	226.3	1.0	0.54	54.0
30X	14	1640	226.3	229.6	3.3	1.78	53.9
31X	14	1845	229.6	234.1	4.5	3.69	82.0
32H	14	1945	234.1	234.4	0.3	0.30	100.0
33X	15	0005	234.4	244.0	9.6	3.06	31.9
34H	15	0120	244.0	245.0	1.0	0.93	93.0
35X	15	0545	245.0	254.6	9.6	9.47	98.7
36P	15	0730	254.6	256.6	2.0	0.41	20.5
			*****Drilled from 256.6 to 257.6 mbsf*****				
37X	15	1715	257.6	267.2	9.6	1.64	17.1
38X	15	2100	267.2	276.8	9.6	1.93	20.1
39P	15	2250	276.8	278.3	1.5	0.71	47.3
				Cored totals:	277.3	187.33	67.6
				Drilled total:	1.0		
				Total	278.3		
201-1230B-							
1H	17	0030	0.0	3.0	3.0	5.39	179.7
2H	17	0155	3.0	12.5	9.5	9.95	104.7
3H	17	0340	12.5	22.0	9.5	9.98	105.1
4P	17	0520	22.0	24.0	2.0	0.99	49.5
5H	17	0705	24.0	33.5	9.5	10.29	108.3
6H	17	0835	33.5	43.0	9.5	10.02	105.5
7H	17	1005	43.0	52.5	9.5	10.22	107.6
8H	17	1145	52.5	62.0	9.5	10.18	107.2
9H	17	1340	62.0	71.5	9.5	10.19	107.3
10P	17	1530	71.5	73.5	2.0	0.99	49.5
11H	17	1925	73.5	81.0	7.5	9.87	131.6
12H	17	2200	81.0	90.5	9.5	7.86	82.7
13H	17	2330	90.5	100.0	9.5	0.78	8.2
			*****Drilled from 100.0 to 101.5 mbsf*****				
			*****Drilled from 101.5 to 103.0 mbsf*****				
14P	18	0740	103.0	105.0	2.0	1.62	81.0
				Cored totals:	102.0	98.33	96.4
				Drilled total:	3.0		
				Total	105.0		
201-1230C-							
1H	18	1000	0.0	4.5	4.5	4.60	102.2
2H	18	1100	4.5	14.0	9.5	9.82	103.4
				Cored totals:	14.0	14.42	103.0

Table T1 (continued).

Core	Date (Mar 2002)	Local time (hr)	Depth (mbsf) Top	Depth (mbsf) Bottom	Length (m) Cored	Length (m) Recovered	Recovery (%)
201-1230D-							
1H	18	1215	0.0	4.0	4.0	4.23	105.8
2H	18	1330	4.0	13.5	9.5	9.99	105.2
				Cored totals:	13.5	14.22	105.3
201-1230E-							
1H	18	1500	0.0	4.0	4.0	3.99	99.8
2H	18	1610	4.0	13.5	9.5	10.07	106.0
3H	18	1720	13.5	23.0	9.5	9.87	103.9
4H	18	1910	23.0	32.5	9.5	10.54	111.0
			*****Drilled from 32.5 to 34.0 mbsf*****				
5P	18	2300	34.0	36.0	2.0	1.02	51.0
				Cored totals:	34.5	35.49	102.9
				Drilled total:	1.5		
				Total	36.0		

Table T2. Concentrations of dissolved species in interstitial water, Holes 1230A, 1230B, and 1230C. (See table notes. Continued on next two pages.)

Core, section, interval (cm)	Depth (mbsf)	Yellowness (JWBL)	pH	Alk (mM)	Cl^- (mM)	SO_4^{2-} (mM)	H_4SiO_4 (µM)	PO_4^{3-} (µM)	NH_4^+ (µM)	Fe (µM)	Mn (µM)	Sr (µM)	Li (µM)	Ba (µM)	ΣH_2S (mM)	DIC (mM)	Acetate (µM)	Formate (µM)
201-1230A-																		
WSTP						28.89				1.6	0.2	82	28	0.1				
1H-1, 135–150	1.35		8.02	8.25	556.4	24.24	819	19	1,920	2.8	2.6	83	29	0.4	0.84	7.30	6.1	5.9
1H-2, 135–150	2.85		8.09	17.19	552.8	19.21		38	1,570	0.8	0.8	83	27	0.4	2.81	15.51	3.3	6.7
1H-3, 144–160	4.44		8.10	27.38	556.4	13.35	877		2,600	3.7	0.2	84	26	0.8	4.72	24.43		
2H-1, 135–150	6.15		8.18	43.71	558.4	5.20	955	175	3,970	0.9	0.2	86	25	2.7	9.41	39.58		
2H-2, 135–150	7.65		8.21	52.54	558.4	0.84	810	138	5,310	0.7	0.1	85	25	21.6	10.9	47.48	11.4	9.5
2H-3, 135–150	9.15		8.14	56.92	558.9	0.27	866	176	6,290	1.8	0.1	89	25	60.3	10.5	51.81	9.1	3.9
2H-4, 135–150	10.65		8.06	60.51	560.7	<0.20	873	200	6,750	1.7	0.1	91	25	95.8	8.48	56.53	8.3	4.7
2H-5, 135–150	12.15		8.10	63.24	562.9	<0.20	979	205	7,710	0.6	0.1	92	26	129.3	6.53	59.71		
2H-6, 135–150	13.65		8.05	67.01	564.4	<0.20	942	245	10,480	0.6	0.1	94	26	163.7	5.24	65.00	13.7	4.0
3H-1, 135–150	15.65		8.01	73.10	566.0		925	277		1.2	0.1	95	26	219.6	3.53	72.53	30.9	4.3
3H-2, 135–150	17.15		8.03	75.27	564.4		929	351	10,530	1.4	0.1	98	26	234.6	1.57	75.48		
3H-3, 135–150	18.65		8.05	77.54	567.5		932	359	10,910	0.7	0.1	101	26	245.3	1.52	78.31		
3H-4, 135–150	20.15	0.53	7.96	83.49	560.4		1093	404	12,020	3.9	0.2	103	27	271.5	1.27	83.26	11.2	6.9
3H-5, 135–150	21.65	0.47	8.05	87.30	559.9		810	403	12,690	1.4	0.3	102	28	279.1	0.712	85.79	9.1	2.9
3H-6, 135–150	23.15		7.97	90.03	560.9		1003	381	14,810	1.7	0.6	105	30	290.1	0.351	90.37	12.4	5.2
4H-2, 135–150	26.65														0.002			
4H-3, 135–150	28.15		8.05	97.43	558.4		1044	423	15,640	28.4	1.1	108	34	318.7	<0.0004	95.53	45.4	5.1
4H-5, 135–150	31.15		8.03	102.32	551.3		958	367		28.3	1.3	107	39	326.2	<0.0004	102.51	22.2	3.3
5H-2, 135–150	36.15		7.98	110.65	556.9		889	337		57.3	0.6	104	46	349.0	0.00046		31.2	6.2
5H-5, 135–150	40.65	0.52	7.92	113.54	560.9		940			41.4	0.4	108	52	384.0	0.00061	111.68	34.0	7.1
6H-1, 135–150	44.15		7.91	118.20	559.4			389		11.7	0.3	106	57	385.5	<0.0004	120.08	20.7	6.5
6H-3, 143–158	47.23		7.93	119.89	555.4		817	276	23,790	5.5	0.2	103	60	374.3	0.00044	118.08		
6H-5, 135–150	50.23	0.53	7.81	123.81	552.3		1028		21,740	20.3	0.7	110	64	385.3	0.00043	126.81	75.1	6.3
8H-1, 135–150	55.65				556.4		776		18,920	23.8	1.0	80	47	23.2			52.3	7.0
8H-3, 135–150	58.65		8.03	130.94	558.4		897	524	23,940	24.4	1.0	111	71	395.4	0.00042	132.17		
8H-5, 135–150	61.65		8.13	131.66	554.9		869	125	25,160	7.9	1.0	113	72	407.0	<0.0002	130.14		
9H-1, 135–150	62.15		7.89	135.81	552.3		884	652	28,670	11.2	1.0	116	77	399.8	0.00042	138.38	33.1	5.0
9H-4, 125–140	65.35		7.96	136.94	556.4		833	478	30,160	17.7	0.7	113	79	360.1	0.00058	140.73		
9H-6, 135–150	68.25	0.57	8.05	137.65	552.3		719			32.6	0.6	100	82	261.5	0.00051	136.49	28.2	9.2
10H-1, 135–150	71.65	0.65	7.93	138.38	525.0			207		9.2	0.8	115	87	382.9	0.00048	144.47	36.5	5.8
10H-3, 135–150	74.65	0.64	7.92	141.90	549.5		884			16.6	0.6	116	94	403.9	0.00206	146.87	22.7	3.5
10H-5, 135–150	77.65	0.65	7.98	140.14	549.3		932			31.0	0.7	107	97	312.6	0.00166	144.05	24.5	8.0
11H-1, 135–150	81.15		8.27	139.87	553.3		1036			23.5	0.7	118	107	395.9	0.00051	148.36	41.8	5.0
11H-3, 135–150	84.15		8.15	148.05	541.2		927			16.0	0.7	115	106	356.1		154.77	35.2	4.1
11H-5, 135–150	87.15		8.02	148.93	548.8		947	453		19.0	0.8	122	114	389.5	0.00059	155.00		
12H-2, 135–150	92.15	0.67	8.12	143.78			868		33,920	21.1	0.7	122	118	412.6	0.00077	145.08	38.8	5.1
12H-3, 135–150	93.65		8.28	146.42			907		35,350	26.0	0.7	121	120	374.1			32.5	7.5
12H-5, 115–130	96.45	0.58	7.97	148.88	551.3										0.00104	154.94		
13H-1, 135–150	100.15		8.08	149.30			939			7.6	1.1	121	131	391.9	0.00051	151.21	36.6	8.3
13H-3, 135–150	103.15																	
13H-5, 135–150	106.15	0.54	8.02	153.32	556.4		955			11.7	1.4	120	134	393.0	0.00044	151.83	29.7	4.4
14H-1, 135–150	109.65	0.60	7.88	159.76	548.8			308	38,790	22.0	1.6	129	138	414.9	0.00062	159.89	28.5	2.7
14H-3, 135–150	112.72																	
14H-5, 135–150	115.72	0.55	8.02	153.82			944		35,520	7.2	1.1	123	145	391.1	<0.0004	155.21		
15H-2, 135–150	119.47		7.88	153.85	548.3		743		40,170	6.7	0.5	119	145	309.0	0.00093	158.39	31.7	6.3
15H-5, 85–98	123.47	0.50	7.93	154.76	551.3				36,300	10.8	0.7	123	154	335.8	0.00265	159.13		

Table T2 (continued).

Core, section, interval (cm)	Depth (mbsf)	Yellowness (JWBL)	pH	Alk (mM)	Cl^- (mM)	SO_4^{2-} (mM)	H_4SiO_4 (µM)	PO_4^{3-} (µM)	NH_4^+ (µM)	Fe (µM)	Mn (µM)	Sr (µM)	Li (µM)	Ba (µM)	ΣH_2S (mM)	DIC (mM)	Acetate (µM)	Formate (µM)
15H-7, 135–150	126.89	0.48	8.24	139.79	553.3		464		36,770	13.7	0.3	75	150	124.3	0.00111	136.41	50.3	41.0
17H-1, 135–150	130.65	0.55	7.79	156.11	547.3		840	466	38,100	16.0	0.5	122	159	347.1	0.00083	161.94	34.8	3.8
17H-2, 135–150	132.15		7.92	157.17	549.8				37,380	11.0	0.5	127	162	399.9	0.00153	162.95	60.8	8.7
17H-3, 135–150	133.65																	
18H-1, 130–150	140.10		7.81	154.04	551.3		775		36,840	31.4	0.5	121	174	341.1	0.00195	160.12	219.8	14.8
18H-2, 135–150	141.65	0.42	7.99	133.16	463.3				34,590	15.2	1.8	101	144	288.5	0.00336	136.41		
18H-4, 0–20	143.30	0.56	7.94	151.69	553.3			177	36,560	8.4	0.4	109	174	281.2	0.00288	155.64	172.5	8.2
19H-1, 135–150	149.65		7.86	112.47	388.2		761	375		22.3	0.3	90	135	318.7	0.00153	114.99	188.7	6.8
19H-3, 0–34	150.62	0.49	7.82	151.59	536.1		905		37,710	14.8	0.4	130	184	460.8	0.00134	155.40	151.7	5.0
21H-3, 135–150	161.63	0.56	8.01	148.30	545.7				39,160	15.2	0.9	138	201	561.7	0.00047	149.36	108.7	4.8
21H-4, 69–84	162.47	0.54	8.08	148.86	560.4		923		37,090	6.2	0.7	143	206	574.2	0.00040	150.48		
22H-1, 75–90	169.05		8.04	148.81	552.8		754		35,800	16.1	0.7	140	217	537.3	0.00046	151.88		
24H-1, 135–150	188.65	0.40	7.7	140.61			998	458	36,970	19.8	0.7	147	257	664.2	<0.0004	147.73	71.0	5.0
24H-2, 0–98	188.80	0.36	7.82	138.40	550.8		885	340		4.7	0.6	148	269	665.7	<0.0004	142.21	175.1	7.6
26H-1, 82–97	199.62	0.29	7.54	129.25	550.3		910		34,290	10.7	0.8	146	285	710.7	<0.0004	137.25	169.4	10.8
26H-2, 14–28	199.91	0.26			495.7		947		33,040								126.4	5.9
27H-1, 95–111	207.25	0.23	7.57	120.35	555.4		887		26,790	3.2	1.2	150	306	644.4	<0.0004	129.98	146.7	8.1
30X-1, 130–150	227.60		8.33	61.01	553.8					2.0	0.6	164	388	858.5				
31X-1, 135–150	230.95															94.33		
33X-1, 130–150	235.70	0.11	7.72	92.87	555.9		924			8.4	1.2	167	413	152.3	<0.0004	96.52	114.3	14.2
34H-CC, 0–12	244.59				542.2		1023			1.5	0.6	178	484	956.1			100.5	8.2
35X-1, 136–156	246.36	0.12	7.74	82.43	553.8		974	33		5.5	0.9	182	502	846.2	<0.0004	75.56	105.1	13.4
35X-4, 0–20	249.56	0.11			538.7		1118			1.9	0.6	185	493	997.5			71.9	9.1
35X-6, 132–150	253.39	0.12			517.5		789			1.3	0.2	97	441	45.8		50.56	65.0	20.9
36P-1, 33–40	254.93																	
37X-1, 115–134	258.75	0.11	8.06	39.20	542.2		1067			1.2	0.5	209	565	1166.6	<0.0004	81.53		
38X-2, 0–19	268.70	0.11	7.91	38.97	552.8		1172	29		9.0	0.9	236	675	1187.3	<0.0004	81.45	56.4	7.8
201-1230B-																		
1H-1, 0–15	0.00	0.02	7.44	2.68		28.84	494			19.4	5.6	84	29	4.0	<0.0004	2.63		
1H-1, 40–55	0.40	0.01	7.59	3.59		28.27	587			2.8	6.2	84	29	3.6	0.0053	3.48	11.0	5.3
1H-1, 80–95	0.80	0.02	7.68	4.88		27.40	701			5.5	5.3	82	29	3.6	0.231	4.66		
1H-1, 120–135	1.20	0.04	7.82	7.31		26.09	787			3.8	3.2	82	28	3.7	0.183	6.90	7.1	5.7
1H-2, 0–15	1.50	0.01	7.82	9.38		25.12	894			7.2	3.2	83	28	7.3	0.824	8.68	13.7	6.2
1H-2, 80–95	2.30	0.09	7.99	14.52		21.46	800			2.6	1.2	83	26	7.1	2.16	13.68		
2H-1, 0–15	3.00	0.08	8.04	16.78		19.60	795			2.9	0.8	83	27	2.8	0.577	15.50	8.8	7.0
2H-1, 60–75	3.60	0.10	8.08	21.09		17.61	899			1.2	0.4	83	26	2.1	3.99	19.33	13.4	7.3
2H-2, 0–15	4.50	0.13	8.13	25.83		14.79	889			1.7	0.2	84	27	9.3	4.37		7.5	6.7
2H-2, 40–55	4.90	0.13	8.12	27.93		13.25	955			3.6	0.3	84	25	9.3	4.71	26.08		
2H-2, 80–95	5.30		8.14	30.62		12.10	919			1.1	0.1	82	26	3.5	6.07		15.3	5.5
2H-3, 0–15	6.00	0.17	8.21	34.40		9.36	965			1.7	0.1	82	26	4.3	7.23			
2H-3, 40–55	6.40		8.21	37.20		7.75	1073			2.3	0.1	85	25	4.4	7.29	34.78	7.5	6.9
2H-3, 80–95	6.80		8.14	40.31		6.66	895			2.0	0.0	83	25	2.9	8.44		10.3	6.0
2H-4, 0–15	7.50		8.15	43.78		4.30	960			1.0	0.0	83	25	3.4	8.79		17.9	7.0
2H-4, 40–55	7.90	0.22	8.18	45.61		3.39	897			0.8	0.0	83	25	5.5	9.16	41.91	7.4	5.6
2H-4, 80–95	8.30		8.21	46.77		1.89	910			0.9	0.0	82	25	11.0	10.1		12.5	8.3
2H-5, 0–15	9.00		8.19	49.17		0.64	942			1.5	0.0	81	26	27.6	10.2		23.4	9.1
2H-5, 40–55	9.40		8.34	50.79		0.64	941			0.9	0.0	84	25	38.4	9.03	44.95	6.2	4.6
2H-5, 80–95	9.80	0.27	8.16	53.26		0.55	952			1.0	0.0	86	25	48.0	9.34		13.8	5.9
2H-6, 0–15	10.50		8.17	54.94		0.47				1.2	0.0	85	25	65.4	8.38		17.0	11.1

Table T2 (continued).

Core, section, interval (cm)	Depth (mbsf)	Yellowness (JWBL)	pH	Alk (mM)	Cl^- (mM)	SO_4^{2-} (mM)	H_4SiO_4 (µM)	PO_4^{3-} (µM)	NH_4^+ (µM)	Fe (µM)	Mn (µM)	Sr (µM)	Li (µM)	Ba (µM)	ΣH_2S (mM)	DIC (mM)	Acetate (µM)	Formate (µM)
2H-6, 60–75	11.10	0.31	8.13	57.29		0.29				2.1	0.1	86	27	75.5	8.76	54.38	10.7	4.6
2H-7, 0–15	12.00		8.2	56.00		0.22				1.1	0.0	89	25	100.1	6.33	57.20	19.1	5.2
3H-3, 135–150	16.85	0.43	8.05	71.92		0.18				1.6	0.0	96	25	212.8	2.88	72.28		
5H-3, 135–150	28.35	0.44	7.99	95.42		0.05				10.9	1.0	105	31	323.8	0.0005	97.20		
6H-3, 135–150	37.85	0.50	8.13	107.56		0.00				39.0	0.5	104	43	346.6	<0.0004	102.38		
7H-3, 135–150	47.35	0.62	8.03	119.21						65.6	0.4	106	55	386.6	0.00047	121.23		
8H-3, 135–150	56.85	0.58	8.13	127.21						41.9	0.9	110	66	380.2	0.00048	128.26		
9H-3, 125–150	66.25	0.65	8.06	136.95						34.4	0.5	113	78	384.8	0.00064	137.74		
11H-3, 135–150	77.85	0.63	8.05	144.95						21.5	0.8	116	90	386.7	0.00049	146.85		
12H-4, 130–150	84.94	0.64	8.16	139.97						13.0	0.4	98	101	295.3	<0.0004	136.64		
12H-6, 105–118	87.69	0.51	8.12	123.40						10.8	0.5	93	91	297.5	<0.0004	124.69		
201-1230C-																		
1H-1, 62–67	0.62					24.94				3.9	7.3	82	29	6.2				
1H-1, 78–83	0.78									3.8	7.1	83	29	4.4				
1H-1, 92–97	0.92									2.3	5.6	83	29	4.0				
2H-2, 0–5	6.00					6.65				2.7	0.1	82	26	2.3				
2H-2, 115–120	7.15					3.31				2.3	0.1	83	26	6.0				
2H-3, 0–5	7.50					2.58				2.0	0.1	84	25	14.9				
2H-3, 115–120	8.65					0.84				1.9	0.0	84	25	32.6				
2H-4, 0–5	9.00					0.63				1.6	0.1	83	25	42.1				
2H-4, 65–70	9.65					0.48				2.4	0.1	86	26	56.9				
2H-5, 0–5	10.50					0.26				2.4	0.1	89	25	82.5				
2H-5, 90–95	11.40					0.15				3.7	0.1	85	24	91.7				

Notes: Alk = alkalinity, SAL = salinity, DIC = dissolved inorganic carbon. WSTP = Well Seismic Temperature Pressure tool. This table is also available in **ASCII.**

Table T3. Dissolved sulfate, Hole 1230A.

Core, section	Before (mM)	After (mM)
201-1230A-		
2H-4	0.00	0.16
2H-4	0.00	0.18
2H-6	0.00	0.13

Notes: Dissolved sulfate was reanalyzed on selected samples at higher sensitivity after waiting 4 days. This table is also available in **ASCII.**

Table T4. Hydrogen concentrations, Holes 1230A and 1230C.

Core, section, interval (cm)	Depth (mbsf)	H_2 (nM)	Incubation temperature (°C)
201-1230A-			
1H-1, 87–93	0.87	0.25	4
1H-2, 65–71	2.15	1.20	4
1H-3, 60–66	3.60	0.99	4
2H-2, 65–71	7.38	0.48	4
2H-5, 70–76	11.50	0.69	4
3H-2, 80–86	16.60	0.65	4
3H-5, 50–56	20.80	1.40	4
4H-5, 95–101	30.75	0.75	4
6H-2, 56–62	44.86	0.99	4
9H-5, 108–114	66.58	0.11	4
11H-4, 70–76	85.00	1.64	4
13H-3, 100–106	102.80	0.78	4
15H-6, 75–81	124.79	0.97	4
18H-3, 65–71	142.45	0.81	4
21H-3, 90–96	161.18	0.14	4
22H-2, 95–101	170.15	0.07	4
24H-2, 53–59	189.33	0.09	4
26H-1, 47–53	199.27	0.13	4
31X-2, 29–35	231.39	0.42	4
201-1230C-			
2H-2, 55–60	6.55	0.42	4
2H-3, 45–50	7.95	0.76	4
2H-3, 85–90	8.40	1.04	4
2H-4, 30–35	9.30	1.19	4
2H-5, 35–40	10.90	0.54	4

Note: This table is also available in **ASCII.**

Table T5. Hydrocarbon gas concentrations in headspace, Hole 1230A. (See table notes. Continued on next page.)

Core, section, interval (cm)	Depth (mbsf)	Methane (ppm in headspace) 20 min @ 60°C	Methane (ppm in headspace) 7 days @ 22°C	Methane (µM)	Ethane (ppm in headspace) 20 min @ 60°C	Ethane (ppm in headspace) 7 days @ 22°C	Ethane (µM)	Propane (ppm in headspace) 20 min @ 60°C	Propane (ppm in headspace) 7 days @ 22°C	Propane (µM)
201-1230A-										
1H-1, 130–135	1.30		96	18		0.3	0.1		0.0	0.0
1H-2, 130–135	2.80	12		*	0.0		*	0.0		*
1H-3, 139–144	4.39		107	21		0.6	0.1		0.0	0.0
2H-1, 130–135	6.10		308	56		0.9	0.2		0.0	0.0
2H-2, 130–135	7.60	297		*	0.0		*	0.0		*
2H-3, 130–135	9.10		9,787	1,852		1.5	0.3		0.0	0.0
2H-4, 130–135	10.60		18,635	3,778		1.2	0.2		0.0	0.0
2H-5, 130–135	12.10		24,398	4,788		1.4	0.3		0.0	0.0
2H-6, 130–135	13.60	11,686		*	0.6		*	0.0		*
3H-1, 130–135	15.60		23,801	5,076		1.4	0.3		0.0	0.0
3H-2, 130–135	17.10	19,625		*	0.8		*	0.0		*
3H-3, 130–135	18.60		33,782	7,196		1.9	0.4		0.0	0.0
3H-4, 130–135	20.10		22,728	4,593		1.9	0.4		0.9	0.2
3H-5, 130–135	21.60		21,777	4,427		1.8	0.4		1.6	0.3
3H-6, 130–135	23.10	15,390		*	0.6		*	0.0		*
4H-1, 145–150	25.25		29,279	6,062		1.8	0.4		1.1	0.2
4H-2, 130–135	26.60	13,767		*	171.7		*	287.1		*
4H-4, 0–5	28.30		27,178	5,486		2.2	0.4		1.7	0.3
4H-4, 145–150	29.75		25,054	5,193		2.0	0.4		1.4	0.3
4H-6, 0–5	31.30	8,798		*	1.8		*	2.3		*
5H-1, 145–150	34.75	7,282		*	0.7		*	0.0		*
5H-3, 0–5	36.30		30,033	6,379		2.1	0.5		0.5	0.1
5H-6, 0–5	40.80		27,186	5,398		2.0	0.4		1.0	0.2
6H-1, 130–135	44.10		18,322	3,815		1.9	0.4		1.2	0.2
6H-4, 0–5	47.38	9,910		*	0.7		*	0.0		*
6H-6, 0–5	50.38		22,898	4,827		1.8	0.4		1.0	0.2
8H-2, 145–150	57.25		15,295	3,219		1.5	0.3		1.0	0.2
8H-3, 130–135	58.60		21,668	4,477		1.8	0.4		0.9	0.2
8H-5, 0–5	60.30	4,390		*	0.0		*	0.0		*
9H-1, 130–135	62.10		25,098	5,201		1.7	0.4		0.8	0.2
9H-4, 135–140	65.45	8,627		*	0.6		*	0.0		*
9H-6, 130–135	68.20		28,139	5,769		2.0	0.4		0.8	0.2
10H-2, 0–5	71.80		29,440	5,907		1.3	0.3		0.5	0.1
10H-4, 0–5	74.80	4,991		*	0.0		*	0.0		*
10H-6, 0–5	77.80		32,417	6,689		2.0	0.4		1.6	0.3
11H-1, 130–135	81.10		21,315	4,410		1.2	0.3		0.8	0.2
11H-5, 130–135	87.10		20,388	4,367		0.8	0.2		1.0	0.0
12H-2, 130–135	92.10	3,849		*	0.0		*	0.0		*
12H-4, 0–5	93.80		14,985	3,246		1.1	0.2		0.5	0.1
12H-5, 0–5	95.30		13,489	2,947		1.0	0.2		0.3	0.1
13H-1, 130–135	100.10	2,699		*	0.0		*	0.0		*
13H-2, 145–150	101.75		20,214	4,240		1.9	0.4		1.2	0.3
13H-5, 0–5	104.80		18,184	3,762		1.8	0.4		1.5	0.3
14H-1, 130–135	109.60	4,799		*	0.0		*	0.0		*
14H-4, 0–5	112.87		32,414	7,091		2.4	0.5		1.7	0.4
14H-5, 130–135	115.67		15,753	3,525		1.2	0.3		0.7	0.2
15H-3, 0–5	119.62	2,832		*	0.4		*	0.0		*
15H-5, 137–142	123.99		25,023	5,534		1.5	0.3		1.2	0.3
15H-7, 130–135	126.84		18,375	4,152		1.3	0.3		1.0	0.2
17H-1, 130–135	130.60		19,981	4,348		1.1	0.2		0.7	0.2
17H-3, 0–5	132.30	4,494		*	0.4		*	0.0		*
18H-2, 130–135	141.60	5,860	21,028	4,629	0.0	1.6	0.3	0.0	1.3	0.3
19H-3, 0–5	150.62	2,911		*	0.5		*	0.0		*
21H-2, 0–5	159.70	13,575		*	2.6		*	0.0		*
21H-4, 0–5	161.78		24,508	5,167		2.6	0.5		2.4	0.5
22H-1, 70–75	169.00		22,781	4,986		2.9	0.6		3.7	0.8
24H-1, 130–135	188.60	3,921	15,490	3,481	1.2	3.2	0.7	0.0	3.9	0.9
26H-1, 80–82	199.60		12,899	3,126		4.9	1.2		5.1	1.2
27H-1, 90–95	207.20		14,241	3,185		5.3	1.2		5.4	1.2
30X-1, 125–130	227.55		19,880	5,133		19.2	4.9		31.9	8.2
30X-1, 130–135	227.60	5,128		*	8.6		*	14.2		*
31X-1, 130–135	230.90	4,142	11,466	2,953	8.0	10.8	2.8	13.0	13.0	3.3
33X-1, 125–130	235.65		16,442	4,424		25.0	6.7		45.8	12.3
34H-1, 54–59	244.54	3,223	11,570	2,925	7.4	13.9	3.5	14.2	50.8	12.8
35X-2, 145–150	248.01		10,958	2,861		9.7	2.5		29.4	7.7

Table T5 (continued).

Core, section, interval (cm)	Depth (mbsf)	Methane (ppm in headspace) 20 min @ 60°C	Methane (ppm in headspace) 7 days @ 22°C	Methane (µM)	Ethane (ppm in headspace) 20 min @ 60°C	Ethane (ppm in headspace) 7 days @ 22°C	Ethane (µM)	Propane (ppm in headspace) 20 min @ 60°C	Propane (ppm in headspace) 7 days @ 22°C	Propane (µM)
35X-4, 0–5	249.56	5,532		*	48.5		*	24.6		*
35X-6, 130–132	253.37		14,185	3,325		52.8	12.4		20.6	4.8
37X-1, 115–120	258.75	8,291		*	64.0		*	59.1		*
38X-2, 0–5	268.70	5,146		*	18.5		*	34.0		*

Notes: * = not calculated due to systematically lower values compared to 8-day extraction. This table is also available in ASCII.

Table T6. Hydrocarbon gas analyses of vacutainer samples, Hole 1230A.

Core, section, interval (cm)	Depth (mbsf)	C_1 (ppm)	C_2 (ppm)	C_2= (ppm)	C_3 (ppm)	*I*-C_4 (ppm)	*N*-C_4 (ppm)	*N*-C_5 (ppm)	*I*-C_5 (ppm)	*N*-C_6 (ppm)	*I*-C_6 (ppm)
201-1230A-											
4H-6, 10–15	31.40	852,212	0.0	0	0.0	0.0	0.0	0	0.0	0	0
5H-1, 50–51	33.80	903,507	0.0	0	0.0	0.8	0.0	0	0.0	0	0
6H-3, 50–51	46.30	867,254	0.0	0	3.0	1.8	0.0	0	0.7	0	0
8H-3, 20–21	57.50	859,269	0.0	0	3.6	2.8	0.0	0	0.9	0	0
9H-4, 15–16	64.25	914,128	0.0	0	3.4	2.9	0.0	0	0.9	0	0
10H-3, 31–33	73.61	717,083	11.8	0	334.6	0.9	3.9	0	0.0	0	0
11H-6, 35–36	87.65	194,642	0.0	0	1.4	0.0	1.0	0	1.2	0	0
12H-1, 109–110	90.39	561,546	0.0	0	1.2	1.1	0.0	0	1.1	0	0
13H-5, 50–51	105.30	729,577	0.0	0	2.0	1.6	0.0	0	0.7	0	0
14H-6, 50–51	116.37	206,679	0.0	0	1.3	0.0	0.0	0	0.7	0	0
15H-5, 55–56	123.17	809,225	0.0	0	1.7	1.1	0.0	0	0.0	0	0
17H-1, 85–86	130.15	793,043	0.0	0	7.2	1.0	0.0	0	1.0	0	0
18H-1, 135–136	140.15	910,164	0.0	0	2.8	1.9	0.0	0	0.0	0	0
19H-2, 80–81	150.60	808,779	0.0	0	12.2	10.7	0.0	0	3.7	0	0
21H-4, 10–11	161.88	872,296	0.0	0	15.6	12.0	0.0	0	7.5	0	0
22H-2, 50–51	169.70	908,598	0.0	0	6.5	2.8	0.0	0	2.6	0	0
27H-1, 75–76	207.05	805,849	0.0	0	33.8	5.7	2.3	0	3.6	0	0

Notes: All samples were run on the natural gas analyzer. This table is also available in **ASCII.**

Table T7. Rock-Eval pyrolysis of sediments. (See table notes. Continued on next page.)

Core, section, interval (cm)	Depth (mbsf)	TOC (wt%)	S_1 (mg HC/g)	S_2 (mg HC/g)	HI (mg HC/g TOC)	T_{max} (°C)
201-1227A-						
2H-2, 55–61	7.65	1.05	0.70	3.13	298	420
2H-5, 93–99	12.53	5.11	1.99	24.30	475	408
3H-2, 65–71	17.25	5.42	3.96	24.10	444	396
5H-5, 86–92	40.96	5.80	1.60	23.42	403	414
6H-2, 60–66	45.70	1.51	0.60	3.97	262	416
6H-3, 124–126	47.84	10.84	8.58	54.59	503	392
6H-4, 59–61	48.69	4.24	1.22	16.56	390	407
6H-4, 122–124	49.32	2.95	1.03	5.58	199	411
7H-2, 74–80	55.34	5.54	4.23	25.53	460	404
9H-3, 65–71	75.75	6.75	5.16	32.05	474	404
10H-2, 50–56	83.60	4.42	2.76	18.73	423	406
11H-2, 88–94	93.48	9.33	3.65	30.52	327	401
12H-2, 83–89	102.93	5.50	3.07	25.61	465	407
201-1227D-						
2H-1, 100–102	8.50	3.26	2.48	10.73	329	407
2H-3, 100–102	11.50	5.35	3.07	19.67	367	400
201-1228A-						
1H-1, 126–141	1.26	9.61	14.03	47.54	494	402
1H-3, 135–150	4.26	4.57	4.72	20.87	456	397
2H-1, 135–150	6.25	6.82	7.34	27.74	406	393
2H-3, 0–15	7.90		6.84	34.86		401
3H-1, 135–150	15.75	8.29	5.40	32.39	390	396
3H-3, 135–150	18.75	6.41	4.90	27.84	434	404
3H-5, 135–150	21.75	4.95				
4H-1, 135–150	25.25	0.98				
4H-3, 135–150	28.25	4.21				
4H-5, 50–52	30.40	10.76	9.47	50.56	469	382
4H-5, 120–122	31.10	0.82	0.34	2.11	257	409
5H-1, 135–150	34.75	3.35				
5H-3, 135–150	37.75	4.56				
6H-1, 135–150	44.25	5.56				
6H-3, 135–150	47.25	0.96				
7H-3, 135–150	56.75	0.21				
7H-5, 135–150	59.75	0.41				
8H-1, 135–150	63.25	0.39				
8H-3, 135–150	66.25	0.77				
9H-3, 135–150	75.75	0.48				
10H-1, 135–150	82.25	2.21				
10H-4, 135–150	86.75	1.67				
11H-1, 85–100	91.25	2.04	1.77	6.58	322	386
12H-1, 88–110	100.78	*0.05*	*0.16*	*0.48*	*960*	*389*
14H-1, 135–150	111.75	*0.45*	*0.32*	*1.26*	*280*	*395*
14H-5, 135–150	117.75	*0.48*	*0.37*	*1.44*	*300*	*396*
16H-1, 135–150	129.75	*0.23*	*0.14*	*0.70*	*304*	*399*
16H-3, 135–150	132.75	*0.49*	*0.23*	*1.29*	*263*	*402*
18H-3, 135–150	151.75	*0.52*	*0.24*	*1.11*	*213*	*399*
19H-2, 135–150	159.19	*0.22*	*0.13*	*0.36*	*163*	*499*
20H-3, 135–150	170.60	*0.27*	*0.13*	*0.69*	*255*	*403*
21H-1, 135–150	177.25	0.67	0.26	1.14	170	393
22H-1, 120–135	186.60	0.50	0.24	0.98	196	392
22H-1, 135–150	186.75	0.45	0.25	0.83	184	390
201-1229A-						
11H-6, 25–27	96.65	0.97	0.33	0.85	87	377
11H-7, 26–27	98.15	3.05	2.21	11.05	362	388
201-1229D-						
7H-2, 30–32	51.10	0.65	0.34	1.00	153	392
8H-2, 30–32	60.60	2.84	1.91	9.76	343	391
201-1230A-						
9H-2, 60–62	62.90	3.48	1.53	10.69	307	416
9H-4, 60–62	64.70	2.64	1.12	6.85	259	410
9H-6, 60–62	67.50	3.25	1.28	7.29	224	377
11H-4, 70–76	85.00	2.48	1.03	5.86	236	415
13H-3, 100–106	102.80	3.30	1.71	11.10	336	410
15H-6, 75–81	124.79	2.50	0.92	6.99	279	422
18H-3, 65–71	142.45	3.15	1.17	9.29	294	411

Table T7 (continued).

Core, section, interval (cm)	Depth (mbsf)	TOC (wt%)	S_1 (mg HC/g)	S_2 (mg HC/g)	HI (mg HC/g TOC)	T_{max} (°C)
21H-3, 90–96	161.18	3.12	1.06	11.53	369	407
22H-2, 95–101	170.15	2.59	1.09	10.29	397	406
22H-3, 0–2	170.63	1.95	1.10	7.28	373	408
22H-3, 27–28	170.90	2.61	1.17	8.31	318	418
26H-1, 38–40	199.18	2.03	0.87	7.80	384	415
26H-2, 33–35	200.10	1.93	1.05	7.18	372	407
30X-1, 48–50	226.78	4.40	1.52	18.02	409	408
31X-1, 22–24	229.82	0.83	0.18	1.90	228	419
31X-1, 88–90	230.48	0.71	0.06	1.35	190	413
35X-1, 90–92	245.90	2.29	0.60	7.66	334	420
35X-2, 90–92	247.46	3.48	1.00	13.58	390	419
35X-4, 36–38	249.92	4.13	3.02	24.86	601	406
35X-4, 78–80	250.34	1.71	0.25	3.79	221	429
35X-5, 68–70	251.74	3.72	1.18	15.11	406	416
201-1230C-						
1H-1, 83–92	0.83	2.49	1.08	7.87	316	413
2H-3, 90–95	8.40	5.21	2.58	13.78	264	414
2H-4, 40–45	9.40	2.54	1.44	7.37	290	411
201-1231D-						
4H-1, 30–32	27.10	*0.47*	*0.95*	*4.74*	*1008*	*536*
4H-4, 30–32	31.60	*0.34*	*0.78*	*3.43*	*1008*	*537*
4H-7, 30–32	36.10	*0.70*	*1.20*	*7.31*	*1044*	*529*
6H-1, 140–142	47.20	*0.43*	*0.43*	*4.80*	*1116*	*537*
6H-3, 140–142	50.20	*0.29*	*0.28*	*3.29*	*1134*	*531*
6H-5, 140–142	53.20	*0.11*	*0.13*	*1.29*	*1172*	*564*
6H-6, 140–142	54.70	*0.12*	*0.02*	*1.47*		*575*
7H-1, 90–92	56.20	*0.06*	*0.01*	*0.75*		*586*
8H-1, 18–20	64.98	*0.07*	*0.00*	*0.79*	*1128*	*525*
8H-1, 28–30	65.08	*0.12*	*0.03*	*1.13*	*941*	*576*

Notes: TOC = total organic carbon, HI = hydrogen index. Data in italics are reported but not discussed in detail because the TOC concentrations were too low to provide meaningful Rock-Eval pyrolysis parameter (S_1, S_2, HI, T_{max}). This table is also available in **ASCII.**

Table T8. Level of seawater contamination expected in cores based on the concentration of PFT observed in sediment, and parallel bead counts, Holes 1230A, 1230B, and 1230C.

Core, section	Sample details	ng PFT/ g sediment	Potential µL seawater/ g sediment	Beads counted	Beads/g
201-1230A-					
1H-1	Center (slurry sect)	0.01	0.01	0 in 50 fields	0
1H-1	Outside (slurry sect)	0.48	0.48		
1H-1	Center	0.03	0.03		
1H-1	Outside	0.03	0.03		
2H-2	Center (slurry sect)	BD	BD	0 in 50 fields	0
2H-2	Outside (slurry sect)	0.12	0.12		
9H-6	Center	0.01	0.01		
9H-6	Outside	BD	BD		
13H-3	Center	0.22	0.22	6 in 50 fields	76
13H-3	Outside	1.42	1.42	73 in 50 fields	1813
15H-6	Center (slurry sect)	0.02	0.02	0 in 50 fields	0
15H-7	Center	0.01	0.01	0 in 50 fields	0
15H-7	Outside	0.34	0.34		
21H-3	Center	0.03	0.03		
21H-3	Outside	0.84	0.84		
22H-2	Center	0.13	0.13		
22H-2	Outside	2.55	2.55		
30X-1	Center	0.35	0.35		
30X-1	Outside	1.68	1.68		
37X-1	Center	0.21	0.21		
37X-1	Outside	5.91	5.91		
38X-1	Center (dry portion)	0.03	0.03	0 in 50 fields	0
38X-1	Outside (dry portion)	1.33	1.33		
38X-1	Center (HTEW, wet)	0.38	0.38	0 in 50 fields	0
38X-1	Outside (HTEW, wet)	2.04	2.04	1 in 100 fields	(88)
201-1230B-					
12H-2	Center, near hydrate	BD	BD		
12H-2	Outside, near hydrate	0.28	0.28		
201-1230C-					
1H-1	Center	0.72	0.72		
1H-1	Outside	2.31	2.31		
2H-1	Center	BD	BD		
2H-1	Outside	0.65	0.65		
2H-3	Center	BD	BD		
2H-3	Outside	0.12	0.12		
2H-4	Center	BD	BD		
2H-4	Outside	0.34	0.34		
2H-5	Center	0.01	0.01		
2H-5	Outside	0.22	0.22		

Notes: Detection limit = 0.01 µL seawater/g sediment, BD = below detection. The potential for microbial contamination is based on 5×10^8 cells/L surface seawater. This may be viewed as an upper limit for microbial contamination because it requires that the sediment be porous enough to allow all of the contaminating cells to travel with the PFT. In many cases, the level of contamination has been determined for both the outside of the core, where drill fluid is expected, and the middle of the core, where it may be clean. HTEW = thermophile enrichment whole-round core. Numbers in parentheses = not considered a significant indication of contamination (see text).

Table T9. Potential seawater contamination for slurries based on PFT results, Holes 1230A and 1230C.

Core, section	Sample details	ng PFT/ mL slurry	Potential µL seawater/ mL slurry
201-1230A-			
1H-2	ENI section	BD	BD
1H-1		0.56	0.56
2H-2		BD	BD
9H-6		BD	BD
13H-3		BD	BD
15H-6		BD	BD
15H-6	ENI section	BD	BD
21H-2	ENI section	BD	BD
31X-2	ENI section	1.30	1.30
38X		0.32	0.32
201-1230C-			
2H-3	ENI section	BD	BD

Notes: Detection limit = 0.025 µL seawater/mL slurry, BD = below detection. ENI = enrichment for thermophiles (see Table **T11,** p. 102).

Table T10. Potential contamination of slurries obtained using fluorescent beads (0.5 µm diameter) as prokaryotic cell mimics, Holes 1230A and 1230C.

Core, section, interval (cm)	Sample type	Beads/fov	Beads/mL sediment	Delivery confirmed
201-1230A-				
1H-1, 45–52	Slurry	0/50	0	Yes
2H-2, 65–79	Slurry	0/50	0	Yes
9H-5, 48–60	Slurry	*		No
13H-3, 50–64	Slurry	0/50	0	Yes
15H-6, 114–128	Slurry	*		No
38X-1 65–71	Slurry	2/100	71	Yes
201-1230C-				
2H-2, 40–45	Slurry	†		Yes
2H-3, 25–30	Slurry	†		Yes
2H-4, 20–25	Slurry	†		Yes
2H-5, 20–25	Slurry	†		Yes

Notes: fov = a field of view under the microscope approximating an area of 22,800 µm^2. * = beads not deployed, † = insufficient slurry sample to process for beads.

Table T11. Media inoculated with sample material from different depths, Holes 1230A, 1230B, and 1230C. (Continued on next page.)

Core: Depth (mbsf):	1230A-1H 1	1230A-1H 2	1230A-2H 7	1230A-9H 66	1230A-13H 102	1230A-15H 124†	1230A-21H 161	1230A-38X 268	1230B-12H-2 (Gas hydrate)
Medium:									
Sed	15°C: MPN		15°C: MPN	15°C: MPN	15°C: MPN			Core 38X	15°C: EN
Sed-Ox	15°C: MPN		15°C: MPN	15°C: MPN		15°C: MPN			
Mono	15°C: MPN		15°C: MPN	15°C: MPN	15°C: MPN			15°C: EN	15°C: EN
Mono-Ox	15°C: MPN		15°C: MPN	15°C: MPN		15°C: MPN			
Poly	15°C: MPN		15°C: MPN	15°C: MPN	15°C: MPN			15°C: EN	15°C: EN
Poly-ox	15°C: MPN		15°C: MPN	15°C: MPN		15°C: MPN			
Aro	15°C: MPN		15°C: MPN	15°C: MPN	15°C: MPN			15°C: EN	15°C: EN
Rad	4°C: MPN		4°C: MPN	4°C: MPN		4°C: MPN			
Rad-Lac	4°C: MPN		4°C: MPN	4°C: MPN		4°C: MPN			
Grad	15°C: EN		15°C: EN	15°C: EN	15°C: EN	15°C: EN			
201-1		RT, 50°C, 80°C: EN		RT, 50°C, 80°C: EN		RT, 50°C, 80°C: EN	RT, 50°C, 80°C: EN		
201-2		RT, 80°C: EN, 50°C: MPN		RT, 80°C: EN, 50°C: MPN		RT, 80°C: EN, 50°C: MPN	RT, 80°C: EN, 50°C: MPN		
201-3		RT, 50°C, 80°C: EN		RT, 50°C, 80°C: EN		RT, 50°C, 80°C: EN	RT, 50°C, 80°C: EN		
201-4		RT, 50°C, 80°C: EN		RT, 50°C, 80°C: EN		RT, 50°C, 80°C: EN	RT, 50°C, 80°C: EN		
201-5		RT, 50°C, 80°C: EN		RT, 50°C, 80°C: EN		RT, 50°C, 80°C: EN	RT, 50°C, 80°C: EN		
201-6		RT, 50°C, 80°C: EN		RT, 50°C, 80°C: EN		RT, 50°C, 80°C: EN	RT, 50°C, 80°C: EN		
201-7		RT, 50°C, 80°C: EN		RT, 50°C, 80°C: EN		RT, 50°C, 80°C: EN	RT, 50°C, 80°C: EN		
201-8		RT, 50°C, 80°C: EN		11°C, RT, 50°C, 80°C: EN		RT, 50°C, 80°C: EN	RT, 50°C, 80°C: EN		
201-8A (H_2)		RT, 50°C: EN		RT, 50°C: EN		RT, 50°C: EN	RT, 50°C: EN		
201-8B (HCOONa)		RT, 50°C: EN		RT, 50°C: EN		RT, 50°C: EN	RT, 50°C: EN		
201-8C (CH_3COONa)		RT, 50°C: EN		RT, 50°C: EN		RT, 50°C: EN	RT, 50°C: EN		
201-9		RT, 50°C: EN		RT, 50°C: EN		RT, 50°C: EN	RT, 50°C: EN		
201-10		RT, 50°C: EN		RT, 50°C: EN		RT, 50°C: EN	RT, 50°C: EN		
201-11		RT: EN		RT: EN		RT: EN	RT: EN		
Fe(III)red	10°C: EN		10°C: EN	10°C: EN		10°C: EN			
Mn(IV)red	10°C: EN		10°C: EN	10°C: EN		10°C: EN			
Methylamine	20°C: DS*								
H_2/HCO_3^-	20°C: DS								
CH_4-ace	20°C: DS								

Notes: Enrichment assays were quantitative (MPN) or qualitative (EN), and incubated at the temperature given or at room temperature (RT = 21°–25°C). † = black layer. * = dilution series in 1:10 steps, starting with 0.25 mL sediment in 10 mL media. Media are defined in Table **T9,** p. 90, in the "Explanatory Notes" chapter (see also **"Microbiology,"** p. 14, Table **T4,** p. 84, **T5,** p. 85, and **T7,** p. 97, all in the "Explanatory Notes" chapter).

Table T11 (continued).

Core: Depth (mbsf):	1230C-2H-2 6.5	1230C-2H-3 8.2	1230C-CC, 2–4 9.2	1230C-CC, 2–5 10.7
Medium:				
Sed				
Sed-Ox				
Mono	4°C: MPN	4°C: MPN	4°C: MPN	4°C: MPN
Mono-Ox				
Poly	4°C: MPN	4°C: MPN	4°C: MPN	4°C: MPN
Poly-ox				
Aro	4°C: MPN	4°C: MPN	4°C: MPN	4°C: MPN
Rad	4°C: MPN	4°C: MPN	4°C: MPN	4°C: MPN
Rad-Lac	4°C: MPN	4°C: MPN	4°C: MPN	4°C: MPN
Grad				
201-1		RT, 50°C, 80°C: EN		
201-2		RT, 80°C: EN, 50°C: MPN		
201-3		RT, 50°C, 80°C: EN		
201-4		RT, 50°C, 80°C: EN		
201-5		RT, 50°C, 80°C: EN		
201-6		RT, 50°C, 80°C: EN		
201-7		RT, 50°C, 80°C: EN		
201-8		RT, 50°C, 80°C: EN		
201-8A (H_2)		RT, 50°C: EN		
201-8B (HCOONa)		RT, 50°C: EN		
201-8C (CH_3COONa)	RT: EN	RT, 50°C: EN		
201-9		RT, 50°C: EN		
201-10		RT, 50°C: EN		
201-11		RT: EN		
Fe(III)red				
Mn(IV)red				
Methylamine	20°C: DS*			20°C: DS
H_2/HCO_3^-	20°C: DS			20°C: DS
CH_4-ace	20°C: DS			20°C: DS

Table T12. Downhole temperature measurement summary, Site 1230.

Depth (mbsf)	Tool	Measurement location	Thermal conductivity (W/[m·K])	Temperature (°C)	Assessment	Recovery next core (%)	Lithology of next core	Disturbance in next core
–20 to –10	WSTP	Seafloor, T Core 1230A-1H	—	1.9				
–10 to 0	Adara	Seafloor, T Core 1230A-1H	—	1.75	Good			
0	Adara	Seafloor, T Core 1230E-1H	—	1.74	Good			
32.5	Adara	Core 1230E-4H	0.75	3.19	OK but large confidence interval; ends far from equilibrium			
33.3	DVTP	B Core 1230A-4H	0.75	3.13	Good	107	Clay and quartz-bearing diatom ooze	No cracks or voids in Section 201-1230-5H-1
73.5	DVTP	B Core 1230B-10H	—	—	Starts rising again after 2 min	130	Clay bearing diatom silt	Highly disrupted 0–150 cm
79.9	DVTP	B Core 1230A-10H	—	—	Three large oscillations ratchet temperature upward	107	Clay-rich diatom ooze	Void with cracks at 30 cm
100	DVTP	B Core 1230B-13H	0.77	5.38	Good; adjusted down by 0.38 for DVTP 2	81	Nannofossil-bearing clay-rich diatom ooze	Very few cracks in Hole 1230A at this depth
148.3	DVTP	B Core 1230A-18H	—	—	Value too low—comparable to bottom-water temperature	34	Clay-rich diatom ooze	Void with cracks at 105 cm
225.3	Adara	Core 1230A-29H	—	—	Slow oscillation, rises in second half			
254.6	DVTP	B Core 1230A-36P	0.91	10.34	Good	17	Quartz and feldspar-rich diatom ooze	Not possible to assess due to low recovery
277.3	—	—	0.83*	11.16†				

Notes: WSTP = Water Sampling Temperature Probe, DVTP = Davis-Villinger Temperature Probe. T = top of core, B = bottom of core. — = not applicable. * = average thermal conductivity. † = projected temperature at base of hole using parabolic projection. The last line shows the temperature extrapolated to the base of the hole using linear fit in Figure **F27,** p. 75, and the mean thermal conductivity computed from data plotted in Figure **F25,** p. 73.

Table T13. Detail of logging operations, Hole 1230A.

Date (Mar 2002)	UTC (GMT – 6 hr)	Tool depth (mbsf)	Remarks
15	2300		End of coring
15	2300–0300		Wiper trip; hole displaced with 150 bbl sepiolite; bottom of pipe set at 80 mbsf
16	0300–0500		Logging rig-up
16	0530		Start going downward with triple combination tool string: TAP/DIT-E/HLDT/APS/HNGS/SGT
16	0815	0	Stop 5 min at mudline for temperature calibration
16	0825	80	Bottom of tool string (TAP) in open hole
16	0845	282	Tool at TD; start logging upward at 900 ft/hr
16	0927	80	Tool back inside pipe; speed up to 1500 ft/hr to log mudline
16	0937	0	Mudline indicated by gamma ray at 164 m below rig floor
16	0945	–15	End of pass 1; standing 5 min and start going back downward
16	0950	80	TAP in open hole
16	1000	282	Tool at TD; start logging upward pass 2 at 900 ft/hr
16	1040	103	End of pass 2
16	1045	80	Tool back inside pipe
16	1305		Tool string on deck
16	1400		Finish triple combo rig-down; start FMS/sonic rig-up
16	1515		Start going downward with FMS/sonic tool string: MESTB/NGT/MCD/DSS
16	1710	0	Tool at mudline
16	1715	80	Bottom of tool string in open hole
16	1730	282	Tool at TD; start of pass 1
16	1815	75	Tool back in pipe; end of pass 1
16	1820	80	Bottom of tool in open hole
16	1830	282	Tool at TD; start of pass 2
16	1845		Pipe raised 10 m
16	1915	70	Tool back in pipe; end of pass 2
16	2110		Tool string on deck
16	2200		Rig-down completed

Notes: UTC = Universal Time Coordinated. TD = total depth. TAP = LDEO Temperature/Acceleration/Pressure tool, DIT-E = Dual Induction Tool, HLDT = Hostile Environment Litho-Density Tool, APS = Accelerator Porosity Sonde, HNGS = Hostile Environment Gamma Ray Sonde, SGT = Scintillation Gamma Ray Tool. MESTB = microelectrical scanner tool, NGT = Natural Gamma Ray Tool, MCD = caliper tool, DSS = deep sound source.

Table T14. Catwalk observations of gas hydrate and evidence for hydrate, Holes 1230A and 1230B.

Core, section, interval (cm)	Top of sample (mbsf)	Observation	IR camera temperature (°C)	IR camera cold spot (mbsf)
201-				
1230B-12H-2, 0–60	81.54	Foliated nodule	13.2	81.9
1230A-15H-5, 85–98	123.47	Fizzing	17.0	123.3
1230A-18H-3, 0	141.80	Fizzing	15.4	141.4
1230A-19H-1, 0–22	148.30	Nodule	16.6	148.5
1230A-19H-1, 135–150	149.65	Fizzing	17.0	149.8
1230A-26H-2, 14–28	199.91	Fizzing	15.5	199.8

Notes: IR = infrared. Hydrates were identified visually and were implied from IR scans, based on low core liner temperatures. Curated depths (top of sample depth) and depths calculated from IR image processing (which represent the coldest spot in a cold part of the core) agree reasonably well. However, refined data acquisition and image processing should improve this correlation.

Table T15. Concentrations of chemical species in a gas hydrate nodule and in interstitial water remaining after the dissociation of gas hydrate containing sediment, Holes 1230A and 1230B.

Core, section:	1230B-12H-2	1230A-11H-3	1230A-19H-1
Matrix:	Hydrate nodule	Ambient interstitial water	20% hydrate
Dissolved species:			
Cl (mM)	33	541.2	388.2
Ba (μM)	7.6	356.1	318.7
Fe (μM)	3.3	16.0	22.3
Li (μM)	3.3	106	135
Mn (μM)	0.2	0.7	0.3
Sr (μM)	3.8	115	90.4
Acetate (μM)	4.3	35.2	161.7
Formate (μM)	4.8	4.1	5.9

Note: These data are compared to concentrations of the same species in interstitial water at the same sediment depth in a parallel hole.